High Performance FM Gyroscopes

by

Burak Eminoglu

A dissertation submitted in partial satisfaction of the

requirements for the degree of

Doctor of Philosophy

in

Engineering - Electrical Engineering and Computer Sciences

in the

Graduate Division

of the

University of California, Berkeley

Committee in charge:

Professor Bernhard E. Boser, Chair
Professor Ali M. Niknejad
Professor Roberto Horowitz

Fall 2017

High Performance FM Gyroscopes

Abstract

High Performance FM Gyroscopes

by

Burak Eminoglu
Doctor of Philosophy in Engineering - Electrical Engineering and Computer Sciences

University of California, Berkeley
Professor Bernhard E. Boser, Chair

MEMS gyroscopes are used in a wide range of applications such as gaming and image stabilization. However, the poor long-term stability of consumer MEMS gyroscopes precludes their use in demanding applications such as inertial navigation. Although devices with higher performance are available, they suffer from substantially higher power dissipation, size, and cost. For wider adoption it is imperative to find solutions that reduce drift without compromising the advantages of MEMS gyroscopes.

This thesis focuses on scale factor and bias stability. The scale factor of any sensor is set by a reference. Unfortunately, conventional amplitude modulated (AM) MEMS gyroscopes measure rate indirectly via the Coriolis force. In these solutions, the scale factor is set by many parameters including mass, spring constant, gaps, and, depending on the implementation, even absolute voltage. Achieving an accurate scale factor requires controlling all of these parameters, a most challenging task. The proposed solution measures rate—degrees per second, i.e. a frequency—directly. The scale factor is set explicitly by an external clock. Since very accurate clock sources are available, scale factor accuracy at the ppm level is readily achievable.

The second issue, bias stability, is addressed with a readout mechanism that implicitly modulates input rate, hence shifting its spectrum away from low-frequency drift sources such as temperature variations. The same approach is used in conventional precision gyroscopes under the name “may tagging”. Those solutions mount the gyroscope on a spinning platform that periodically rotates the transducer, thereby inverting its sensitivity. The proposed solution achieves the same without moving the transducer and hence is compatible with low cost planar MEMS implementations.

To my family.

Contents

List of Figures

List of Tables

Acknowledgments

First of all I would like to thank my thesis advisor Prof. Bernhard E. Boser for his help, guidance and support during my graduate studies. His unique way of looking at problems and passion to impact the industry with university research always inspired me in the academic environment.

I would like to thank Prof. Ali Niknejad for his support to my thesis. His classes are one of the most fruitful experiences which I have had as a student and a GSI. I also want to thank for Prof. Roberto Horowitz for his valuable feedback in my qualifying exam and thesis.

During my study, I had an opportunity to work with amazing people. I would like to thank my colleague Mitchell Kline who is one of the main brains behind this PhD thesis. The time when I was working with him was one of the most inspiring periods of my research career. I also would like to thank Igor Izyumin for his endless help. Igor has very strong intuition and deep knowledge about both technical and non-technical subjects: he is basically a walking library. I would like to thank Yu-Ching Yeh for her continuous support of my research. Without her contribution, this thesis would never have been finished. I would like to thank Luya Zhang and Sidney Buchbinder for their help during the tapeout period. I also want to thank Kaveh Gharehbaghi for his valuable partnership.

I would like to thank my colleagues Behnam Behroozpour, Eftyhmios Papageorgiou, Pramod Murali, Hao-Yen Tang, and Mahsa Sadeghi for their endless friendship. I always think that I am very lucky to be surrounded by not only super smart people but also super nice people. I really wish that our friendship will continue forever.

Special thanks to my friend Soner Sonmezoglu for his continuous support since METU years. I owe limitless thanks to Alper Ozgurluk for his invaluable friendship and roommateship for more than 5 years. I also would like to thank to my friends Gulustan Ozturk, Ziya Ercan, Mert Korkali, Levent Beker, Ufuk Senveli, Ilbey Karakurt, Sercan Baglama, Cem Yalcin, Sedat Pala, and Imre Ozbay for all of the wonderful memories we have had together.

I would like to thank Parsa Taheri-Tehrani and Prof. David Horsley at UC Davis for their helps in transducer design and Professor Thomas W. Kenny and his group at Stanford University for the MEMS fabrication. I acknowledge the support of this project by DARPA under the PASCAL program and thank the TSMC University Shuttle Program for CMOS fabrication.

Our life was much easier with the awesome people of EECS Student Affairs. Special thanks to Shirley Salanio for her endless helps. I also would like to thank Kim Ly, Richard Lossing, and Dalene Corey from BSAC; Mila MacBain, Shelly Kim, and Huo Chao Kuan from Swarm Lab.

Last but not least, I would like to thank my brother Selim Eminoglu for his endless guidance in my academic and non-academic life, my mother Ayla Eminoglu, my father Muhittin Eminoglu, and my grandmother Gullu Eminoglu for their support and encouragement through all my life.

Chapter 1

Introduction

MEMS gyroscopes have become very popular in different applications such as gaming, image stabilization, and navigation. The cost of gyroscopes have been decreased dramatically in the consumer grade products. These products also occupy very small volume, and consume low power, but their performance is not good enough for applications requiring long-term stability. On the other hand, high performance gyroscopes, which are suitable for these applications, are expensive, bulky, and power hungry. There is a demand to meet high performance requirements while keeping cost, size, and power low. Figure 1.1 shows commercial and tactical grade inertial measurement units (IMUs) which have 3-axis gyroscopes and 3-axis accelerometers.

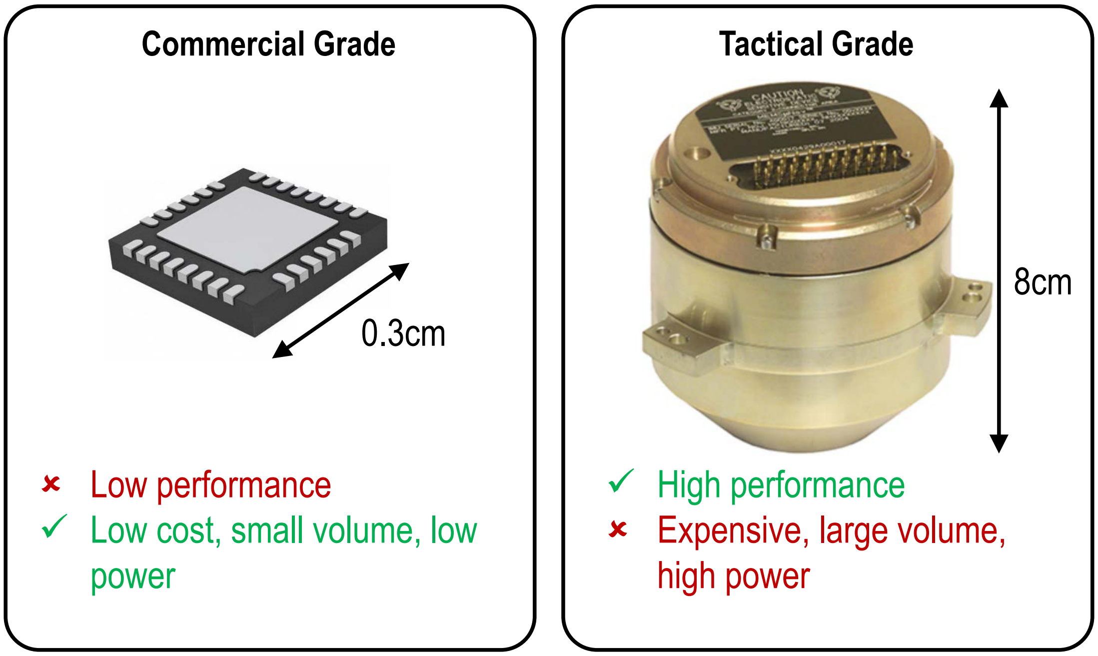

Figure 1.1. Typical IMUs in the market [1, 2].

Conventional high-performance MEMS gyroscopes have three main drawbacks. First, transducers require sophisticated calibration and trimming to improve the performance. Trimming and calibration of an individual device increase cost considerably. Similarly, designs for these applications are relatively large to reduce the effect of fabrication intolerance and packaging issues. Second, electronics consume significant power to reduce the noise. Third, the sensitivity of a conventional gyroscope to angular rate relies on several transducer and electrical parameters which are very challenging to monitor and control even with calibration.

There are two important performance parameters for gyroscopes: bias and scale factor. Figure 1.2 shows a input-output curve of a gyroscope. Ideally, this relationship should be a straight line passing through the origin with a well-defined slope called scale factor (SF). However, in practice this line has offset which is called bias. These parameters drift due to temperature, aging, and stress. In addition, they also vary significantly from sensor to sensor even in the same batch. As a result, maintaining the stability of bias and scale factor is a big challenge in order to meet navigation requirements.

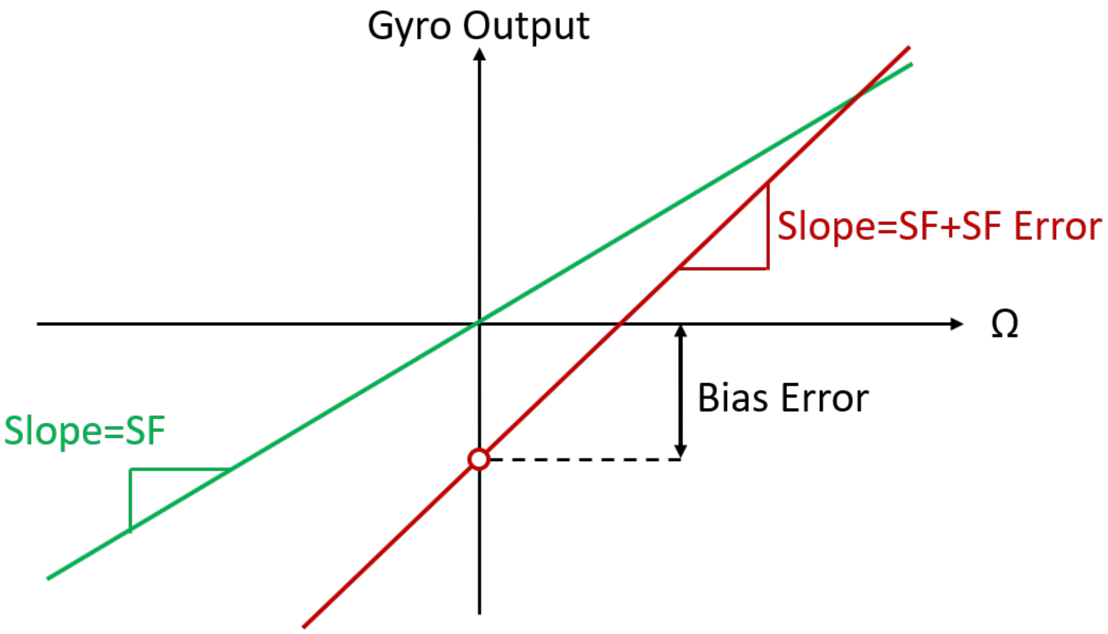

Figure 1.2. Important gyroscope parameters.

In the literature, there are several efforts to understand and minimize the sources of instabilities of bias and scale factor. Furthermore, new system and circuit techniques have been introduced to relax the noise and power trade-off. A brief summary of the error sources, challenges, and recent advances in the literature are given in the following sections.

1.1 Bias Stability

The gyroscope is a two degree-of-freedom (DOF) resonator as shown in Figure 1.3. This resonator is composed of one proof-mass having 2-DOF and shuttle frames with 1-DOF. Shuttle frames are coupled to the proof mass via coupling springs. The overall structure can also be considered as two individual coupled resonators which are moving in perpendicular axes (x- and y- axis).

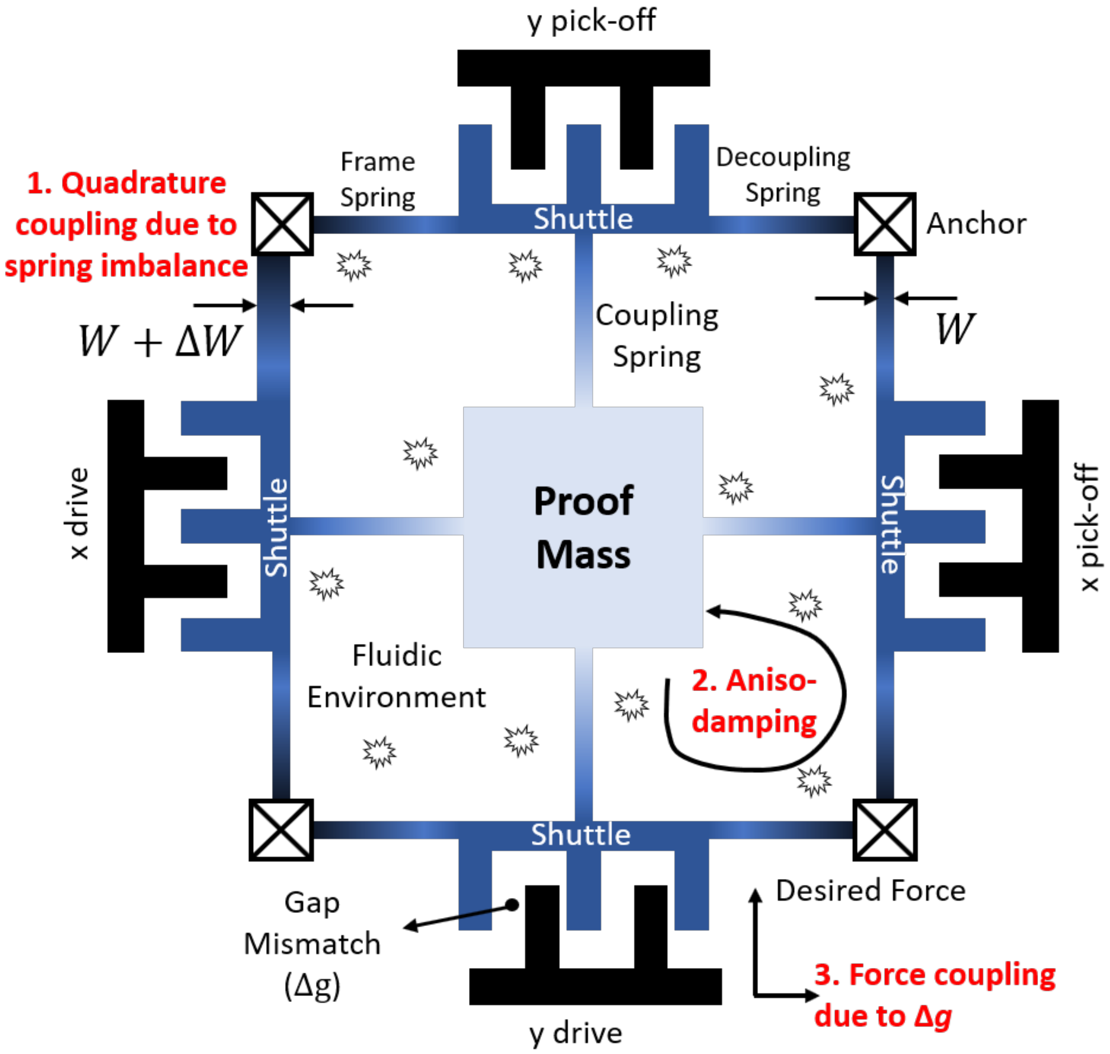

Figure 1.3. Simplified gyro structure with typical error sources.

These individual resonators are ideally only coupled to each other with the Coriolis effect which arises from a rate-induced fictitious force in a rotating frame with an angular rate of Ω. In order to generate this fictitious force, a 2-DOF mass (m) needs to have a certain velocity ($\dot{x}$). Then, the Coriolis force equals $F_{\text{Coriolis}} = 2m\dot{x} \times \Omega$ which is in-phase with the velocity of the moving body.

However, there are also other undesired coupling forces between the resonators. These coupling forces cause error at the output and degrade the bias stability which is one of the key performance parameters. There are three main undesired coupling mechanisms in MEMS gyroscopes.

(1) Quadrature coupling is a force between the two mechanically-coupled resonators which is mainly due to the spring and transduction imbalances resulting from fabrication imperfections. This error is quadrature with the Corilos force, and hence it only affects gyro output if there is a phase error in the electro-mechanical signal path. As Figure 1.3 shows that major source of a quadrature error is the size mismatch of spring beams [5].

Quadrature coupling is the dominant error source for commercial grade gyroscopes. To minimize the effect of quadrature error, it is a common practice to use high-bandwidth electronics to minimize the phase error of the loop by sacrificing the power consumption. Alternatively, the phase error can be characterized and corrected continuously in the background by monitoring temperature fluctuations during operation [6].

Quadrature error can be tuned by using an electromechanical suppression method that utilizes special electrodes placed within a gyroscope. A servo-loop can be used to estimate and then cancel the quadrature coupling to enhance the bias stability [5].

(2) Anisodamping error is an in-phase coupling force due to the anisotropic losses in the transducer. The major source of this error is the fluidic coupling between moving masses of each channels. As shown in Figure 1.3, fluidic environment, i.e. residual molecules in the vacuumed package, causes this coupling when the suspended mass moves. Since, this force is directly proportional to the velocity, it directly adds on Coriolis Force, as well [7].

This error has the same signal-path as Coriolis force. For symmetric designs, this error is same in both channels (x and y) of 2-DOF resonator where rate polarity is opposite[7]. This feature is exploited in the conventional gyroscopes by alternating x and y channels as drive and sense modes [8] and getting the difference of the rate outputs between consequent measurements. This method eliminates the anisodamping error and improves the bias stability. This approach is similar to correlated double sampling (CDS) in electronics. In practice, there is anisodamping mismatch between channels which limits the performance of this method.

(3) Force coupling error is due to the misalignment and imbalance of the forcer electrodes due to fabrication and packaging problems (Figure 1.3)[9]. Due to these problems, the sustaining force used to compensate the energy loss in the resonators also results in an orthogonal force which couples to the rate output. Since the sustaining force is in-phase with the velocity, the resultant parasitic force is also in-phase with the velocity and Coriolis force [10, 11]. Because of this in-phase nature, this coupling force directly degrades the bias stability. However, in contrast to anisodamping error, this error has a different signal-path than the Coriolis force. This feature makes it possible to differentiate the force coupling error from the rate output. Alternating the drive actuation force faster than the drive mode-bandwidth has recently been introduced to correct this error [11].

1.2 Scale Factor

Scale factor is the sensitivity of the gyroscope, and it is important especially for applications where the system is exposed to significant amount of rotation, such as indoor navigation. In this application not only is a person changing their heading direction continuously, but they are also continuously moving their hands and legs, presenting further challenges to navigation. However, conventional gyroscopes have poor scale factor accuracy which does not meet the indoor navigation requirements.

There is a fundamental problem in the conventional approach. When the sensor is exposed to a rotation, the rotation-induced energy couples to the secondary axis through a Coriolis force. The Coriolis force results in displacement and an electrical signal through the electro-mechanical interface and front-end electronics. The electrical signal is then amplified and converted to a digital signal by ADCs. In open-loop gyroscopes, this digital signal is directly measured. In closed-loop gyroscopes the feedback signal that re-balances the Coriolis force is used as a measure of the angular rate. These signal paths are very long and consist of several mechanical and electrical elements with various parameters. To improve the scale factor accuracy, all of these parameters needed to be controlled accurately which is a difficult task.

Gyroscopes measure angular rate which is a frequency of rotation. Frequency is a physical parameter that exits in both mechanical and electrical domains. However, this unique feature of angular rate measurement is not exploited in conventional gyroscopes. Instead, rate-information is extracted indirectly through a long path relying on an inaccurate amplitude measurement.

Whole angle gyroscopes do not have this problem due to their direct angle-readout [12, 13]. Unfortunately, the noise of these gyroscopes is higher compared to force feedback gyroscopes. For this reason, these gyroscopes only operate in whole-angle mode if the external angular rate is large, otherwise they operate in force-feedback mode due to its low noise [14].

1.3 Mode-matching

The noise of a typical MEMS gyroscope is due to two main sources: mechanical (Brownian) and electrical noise. The former noise source is the fundamental limit and is determined by the energy loss in the mechanical structure. This noise comes from the random fluctuations in the thermal energy of the mass and appears as a force noise applied to the suspended mass. Thus, it is not shaped by the resonator itself.

The electronic noise, on the other hand, adds on to the interface signal coming from the transducer and it is shaped by the resonator. Since the pick-off signal in resonator-x is generated by the energy coupling from resonator-y, the frequency of this pick-off signal is ω_y. However, the noise on this signal is shaped by resonator-x with a resonance frequency of ω_x. Hence, the electrical noise is proportional to the the mode-split $\Delta\omega = \omega_x - \omega_y$.

In order to reduce the effect of electrical noise, this mode-split should be minimized. Minimizing the electrical noise also implies minimizing the power for the same noise targets. To achieve this, the mode-split should be smaller than the mechanical bandwidth.

However, this is not a trivial task for conventional solutions since the resonance frequency of one of the modes (sense mode) is not observable. There have been efforts to observe the resonance frequency which increase system complexity and hence potential errors [15, 16, 17, 18]. In addition, decreasing the mode-split also decreases the bandwidth of the open-loop gyroscopes. Closed-loop systems can increase the bandwidth of open-loop with increased complexity.

1.4 3-Axis Gyroscopes

In addition to the aforementioned issues, the design and fabrication of high-performance 3-axis gyroscopes is very challenging. In commercial applications, having all three axis in the same proof mass is preferred to reduce the cost and size. However, current fabrication techniques do not allow symmetric structures for out-of plane devices. Therefore commercial products typically use asymmetric structures to measure all three axes [19]. These asymmetric structures have higher error sources compared to symmetric gyroscopes such as DRGs and QMGs [20, 21, 22].

1.5 Organization of the Thesis

There have been recent advances demonstrating significant performance improvements in the literature. However, there is still a large demand for improved performance without increasing the power, size, and cost.

This thesis first discusses the background calibration techniques for conventional amplitude modulated (AM) gyroscopes in Chapter 2. These techniques reduce bias and scale-factor errors and are applicable to both symmetric and asymmetric transducers, making them attractive for commercial-grade 3-axis gyroscopes.

Next, Frequency Modulated (FM) gyroscopes will be discussed in more details. FM gyroscopes have been recently introduced and they have inherently stable operation without any calibration [23, 24]. This operating mode is more suitable for high performance single-axis applications, because it requires symmetric structures for proper operation.

FM gyroscope solves most of the challenges facing today's gyroscopes. Rate is digitized with reference to an external precision clock, providing a very stable scale factor. The structural symmetry combined with inherent chopping minimizes the bias instability. Continuous monitoring of the mode split enables low power operation.

Chapter 3 gives a review of FM gyroscopes with detailed error analysis. Chapter 4 introduces an indexing technique for mode-matched FM gyroscopes. Chapter 5 discusses the ASIC implementation with additional techniques to improve the short-term noise and bandwidth for chopped FM gyroscopes. Chapter 6 contains a summary of this work.

Chapter 2

Background Calibration Techniques

Managing the trade-off between the performance and size, cost, and power is a big challenge for conventional MEMS gyroscopes. Background calibration techniques relieve this trade-off by estimating and correcting the errors in the bias and scale factor during operation. In this chapter, new background calibration techniques for conventional gyroscopes will be discussed.

2.1 Background Calibration for Scale Factor

Scale factor accuracy is critical for navigation grade gyroscopes. In traditional open-loop MEMS vibratory gyroscopes, the scale factor depends on the mechanical resonator characteristics which are functions of ambient conditions such as temperature and pressure. Force-feedback reduces this sensitivity but introduces new variations including proof mass bias voltage, drive mode velocity, interface capacitances, dimensions of the pick off and forcer electrodes, and mass. In gyroscopes with digital output, the scale factor also depends on the ADC reference voltage. Whole angle gyroscopes achieve a stable scale factor but require a complex controller [25], and compared to force-feedback rate gyroscopes, they suffer from poor resolution [26]. Although this drawback can be overcome by combining a whole angle and rate gyroscope to simultaneously achieve accurate scale factor stability and high resolution [27], this solution adds significant complexity. An alternative approach described in [28] injects a virtual rate signal to continuously monitor and cancel variations of the scale factor. This implementation only requires one gyroscope, but here it is difficult to isolate the sense mode and the calibration loop from each other. The presence of angular rate in the same band as the injected tone will degrade the scale factor accuracy. Choosing the frequency of the injected tone outside the signal band reduces the feed-through but limits the bandwidth of the gyroscope. This problem can be alleviated by injecting non-uniform rate signal instead of a fixed tone, but this makes the system more sensitive to the errors in the complicated demodulation algorithms [29].

Our proposed ratio-metric readout technique for force-feedback gyroscope results in a scale factor that depends only on the ratio of the sensitivities of the sense and drive forcer capacitances, thus eliminating the major sources of drift. It combines FM and force-feedback concepts, and it does not require a second gyroscope or direct signal injection to the sense mode.

2.1.1 Review of Force Feedback Gyroscopes

Force feedback gyroscopes have two control loops. First, the sense mode controller rebalances the quadrature and Coriolis forces such that the proof mass does not move in the sense (y) axis. Second, the drive mode controller regulates the velocity of the drive (x) axis. Both of these loops affect the scale factor accuracy.

2.1.1.1 Sense Mode Effects on the Scale Factor

Figure 2.1 shows the block diagram of a typical control loop for sense mode. Its closed-loop dynamics is modeled as

$$m_y\ddot{y} + b_y\dot{y} + k_y y + 2m\alpha_z\dot{x} + b_{xy}\dot{x} + k_{xy}x = \underbrace{F_{yd}\cos(\omega t)}_{\text{in phase with } x} + \underbrace{F_{yv}\sin(\omega t)}_{\text{in phase with } \dot{x}} \tag{2.1}$$

where m, b, and k are mass, damping, and stiffness terms, respectively. α_z is the angular gain of the transducer which only relies on the transducer geometry. F_{yd} and F_{yv} are the base-band components of the feedback forces which are in phase with the drive mode displacement and velocity, respectively. In order to have a zero motion in the sense axis, the controller enforces the following conditions:

$$\begin{aligned} y &= 0 \\ F_{yd} &= k_{xy}x_a \\ F_{yv} &= (2m\alpha_z\Omega + b_{xy})\dot{x}_a \end{aligned} \tag{2.2}$$

Here x_a and $\dot{x}_a$ are the base-band components of the drive mode displacement and velocities, respectively. Equation 2.2 shows that F_{yv} includes the angular rate information, and this force does not depend on the resonator characteristics. Consequently, the system bandwidth is not limited by either the mechanical bandwidth nor the frequency split. Furthermore, there is no non-linearity in the pick-off and forcer electrodes, since there is no motion in the sense axis. This avoids noise folding, which otherwise can significantly degrade the gyroscope resolution. F_{yv} also includes a bias error due to anisotropic damping (b_{xy}) which will be neglected in this section, because it does not affect scale factor accuracy.

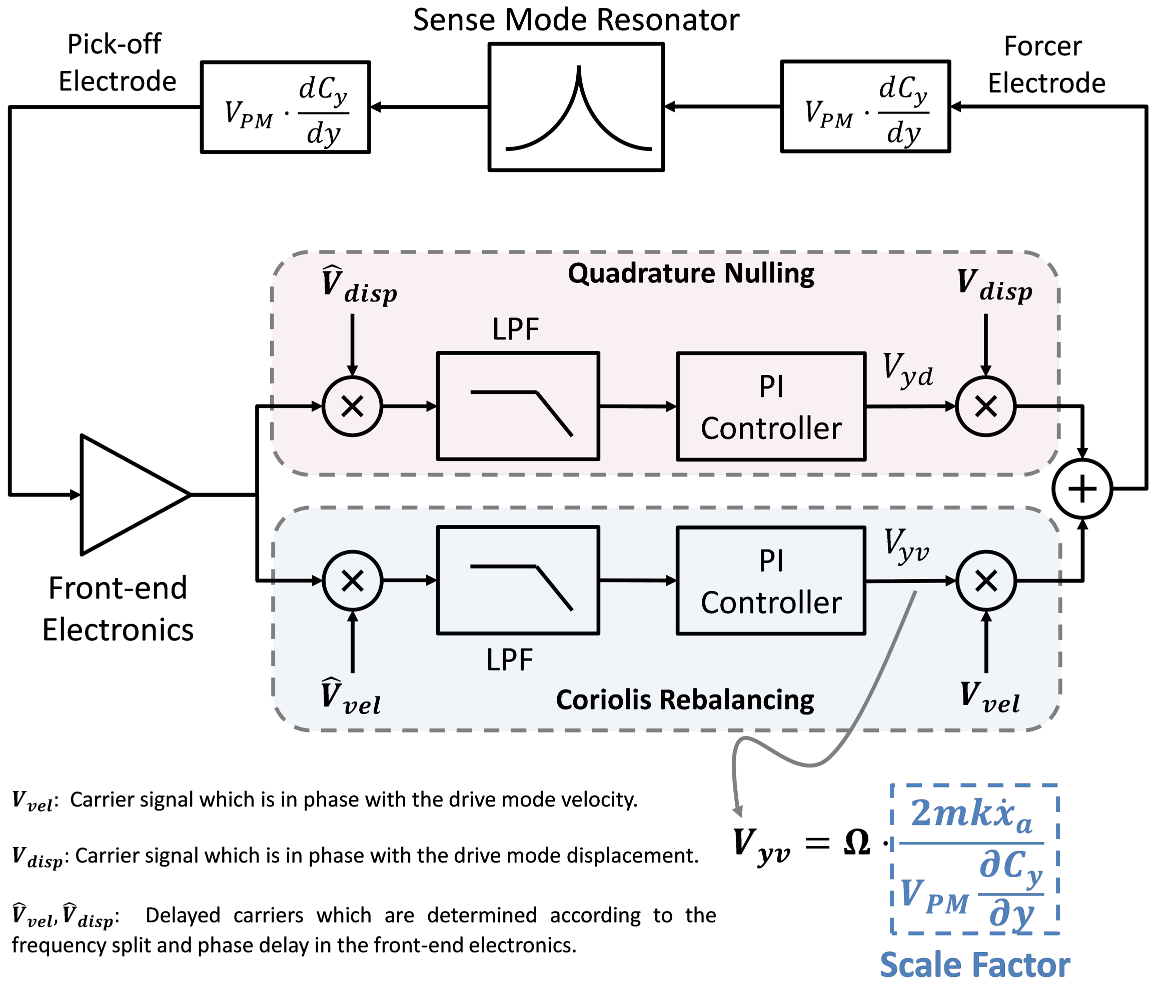

Figure 2.1. Block diagram of the sense mode control loop with scale factor expression.

The feedback forces are generated by applying a voltage to the forcer electrodes as shown in (2.3). The range is limited by the maximum amount of the voltage which can be applied by the feedback electronics.

$$F_{yd,yv} = V_{PM} \frac{dC_y}{dy} V_{yd,yv} \text{ for } y = 0 \tag{2.3}$$

where V_{yd} and V_{yv} are the feedback voltages to generate F_{yd} and F_{yv}, respectively. V_{PM} is the proof-mass bias and dC_y/dy is the spatial derivative of the capacitance of the pick-off electrode. Using (2.2) and (2.3), the angular rate can be written as

$$\Omega = V_{yv}/SF \tag{2.4}$$

where SF is the scale factor which can be expressed by

$$SF = \frac{2m\alpha_z \dot{x}_a}{V_{PM}\dfrac{dC_y}{dy}} \tag{2.5}$$

Equation 2.5 shows that the scale factor does not depend on the sense mode resonator characteristics, but it still depends on the mass, drive mode velocity, proof mass voltage, and spatial derivative of the forcer capacitance. These dependencies are the limiting factors for the scale factor accuracy in navigation grade applications. In addition, this analog feedback voltage also needs to be converted into a digital code by an ADC. In this case, rate and scale factor expression can be modified to (2.6) and (2.7), respectively.

$$\Omega = D_{yv}/SF \tag{2.6}$$

where D_{yv} is the digital code of V_{yv}.

$$SF = \frac{2m\alpha_z \dot{x}_a}{V_{PM}\dfrac{dC_y}{dy}} \cdot \frac{A_{conv}}{V_{ref,ADC}} \tag{2.7}$$

where A_{conv} is the conversion gain, and $V_{ref,ADC}$ is the reference voltage of the ADC. Equation 2.7 is also the same for digital implementations of the controller. In this case, A_{conv} is the inverse of the DAC gain.

The velocity, voltage dependencies, and dC_y/dy in (2.7) are more likely to change with temperature, stress, shock, etc. Other parameters, such as angular slip factor and mass, also cause uncertainties in the scale factor, but they can be considered as robust parameters which are insensitive to the environmental disturbances.

2.1.1.2 Drive Mode Effects on the Scale Factor

Typical self-oscillation loops implement velocity control as shown in Figure 2.2. The drive mode velocity is determined by the reference voltage $V_{amp,set}$ for amplitude set point, electronics gain A_{dr}, and electromechanical conversion gain $V_{PM} \cdot dC_x/dx$.

$$\dot{x}_a = \frac{V_{amp,set}}{A_{dr}V_{PM}\dfrac{dC_x}{dx}} \tag{2.8}$$

All the parameters that appear in the drive mode velocity are susceptible to drift. In order to have a stable operation, these parameters should be controlled accurately.

Voltage references are another important limitation for the scale factor accuracy. These voltage dependencies appear in several places in the scale factor expression such

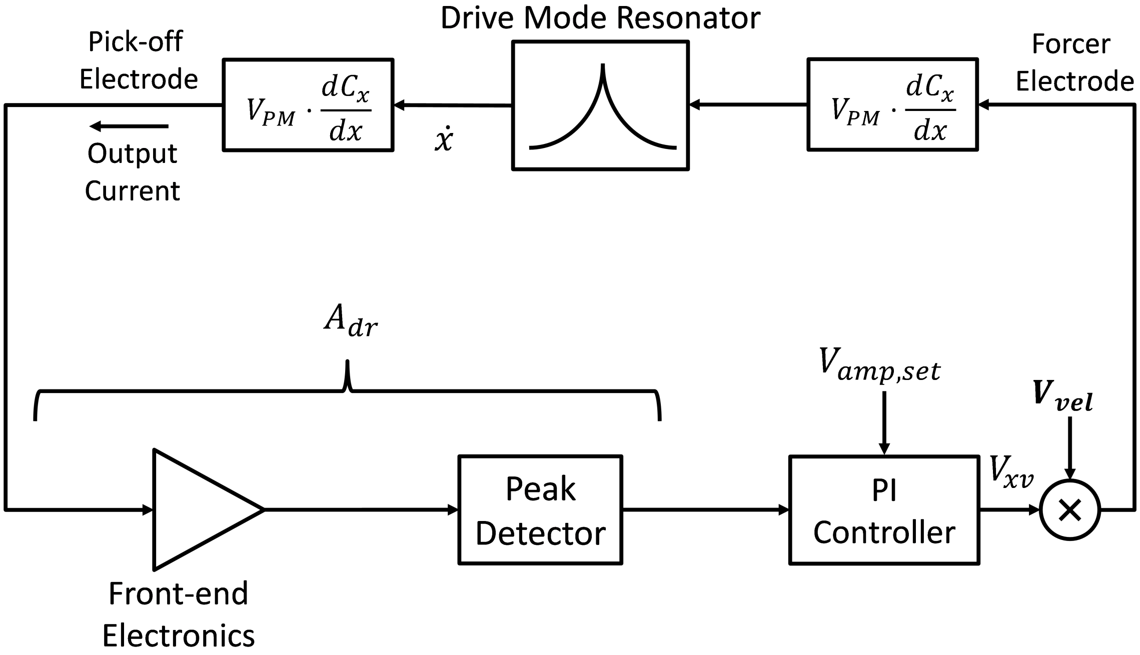

Figure 2.2. Block diagram of the drive mode control loop.

as proof mass, amplitude set, and ADC reference voltages. The effect of the voltage references can be reduced by sharing the same source (V_{ref}).

Referring all of the voltage references in the system to V_{ref} and inserting (2.8) into (2.7), the overall scale factor expression becomes

$$SF = 2m\alpha_z \frac{1}{A_{dr}} \frac{1}{\frac{dC_x}{dx}\frac{dC_y}{dy}} \frac{1}{V_{ref}^2} A_{ref} \tag{2.9}$$

where A_{ref} is a scalar determined by the ratios between V_{ref} and other voltage references in the system such as V_{PM}, $V_{ref,ADC}$, and $V_{amp,set}$.

However, the voltage reference dependency in (2.9) is still not low enough for navigation grade applications which require sub 1-ppm scale factor accuracy.

In brief, (2.9) shows the scale factor of the force feedback gyroscopes depend on the gain of the drive mode front-end amplifier, multiplication of the dC_x/dx and dC_y/dy terms, and V_{ref}. These parameters can be monitored and calibrated to get an accurate scale factor, but this approach is expensive and ineffective because of the limited resolution of the monitor.

2.1.2 Ratio-Metric Readout Technique for Force Feedback Gyroscopes

It was shown that the scale factor of force feedback gyroscopes depends on several parameters, degrading scale factor accuracy. There is a very significant fundamental limitation behind this poor scale factor: The input is an angular rate which is a frequency of rotation; however, the output of the system is a voltage/digital code. Therefore, all the parameters in the signal path between the frequency and voltage/digital code appear in the scale factor expression.

On the other hand, it is possible to get the unknown relation between the frequency and voltage in the drive mode. It is known that the drive mode oscillation frequency is set by the springs and mass in the drive mode resonator. The springs can be considered as a mechanical element which generates force which is in proportional to the displacement. The same effect can be carried out in electrical domain by generating a force which is in-phase with the drive mode displacement. This phenomenon enables us to modulate the frequency by applying a voltage through the forcer electrode in the drive mode. The relation between the modulated frequency and the applied modulated voltage gives the unknown relation between the angular rate and feedback voltage. This unknown relation can be continuously monitored, and the force feedback output can be normalized with this relation. This new normalized output provides a ratio-metric output with dimensionless scale factor. Figure 2.3 shows the proposed ratio-metric readout technique for force feedback gyroscopes.

2.1.3 Theory

The drive mode dynamics can be written as

$$m\ddot{x} + b_x\dot{x} + k_x x = F_{xd}\cos(\omega t) + F_{xv}\sin(\omega t) \tag{2.10}$$

where F_{xd} and F_{xv} are the base-band components of the feedback forces which are in phase with the drive mode displacement and velocity, respectively. In conventional drive mode loops, F_{xd} is set to 0, and F_{xv} is generated by the controller to achieve the required oscillation amplitude. In our approach, there is no need to have an extra control loop to regulate the velocity, since the scale factor is inherently free from the velocity. Moreover, velocity settling takes a considerable amount of time for open-loop self-oscillation loops if the Q-factor is high. Therefore, it is better to have an amplitude control as shown in Figure 2.3. In this case, F_{xv} regulates the oscillation amplitude with the help of the controller, and F_{xd} sets the oscillation frequency with the mechanical spring as shown in (2.11) and (2.12), respectively.

$$b_x\dot{x}_a = F_{xv} \rightarrow \dot{x}_a = \frac{F_{xv}}{b_x} \tag{2.11}$$

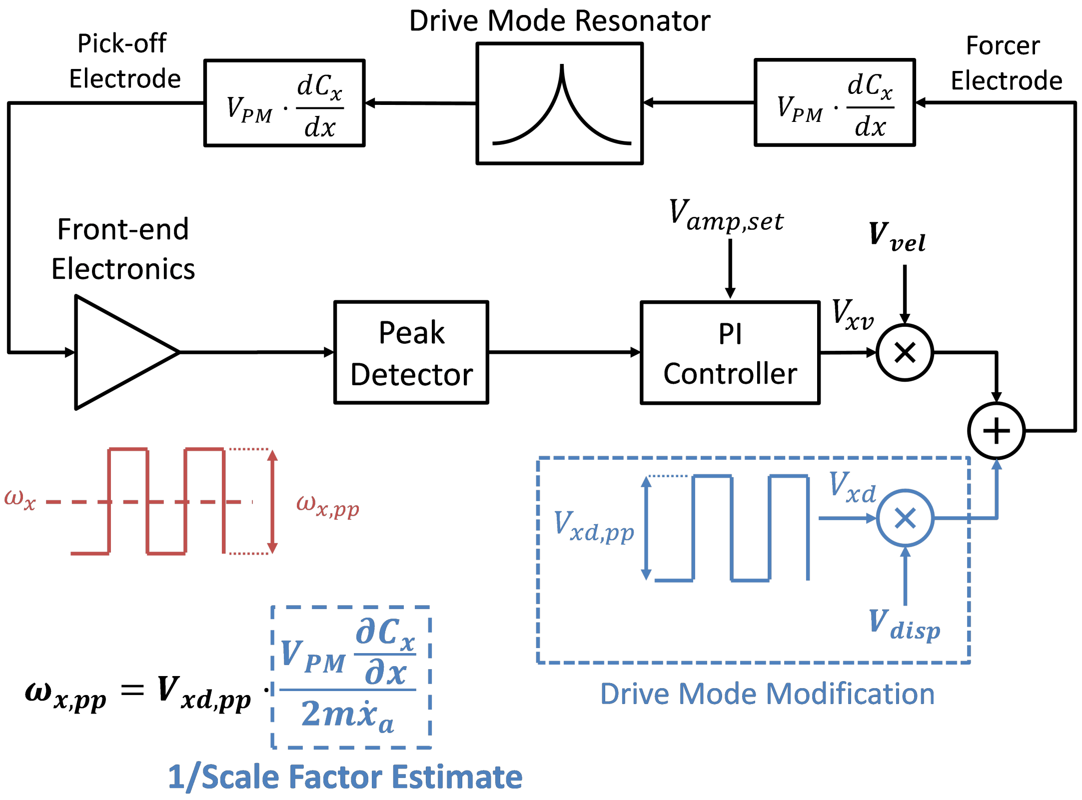

Figure 2.3. The proposed ratio-metric readout technique for force feedback gyroscopes.

$$m\ddot{x} + k_x x = F_{xd} \rightarrow -m\omega^2 x_a + k_x x_a = F_{xd}$$
$$\rightarrow \omega = \sqrt{\frac{k_x - \frac{F_{xd}}{x_a}}{m}} \tag{2.12}$$

The mechanical spring constant is much higher than the electrostatic spring constant in (2.12). Therefore, (2.12) can be simplified using Taylors series expansion as

$$k_x \gg \frac{F_{xd}}{x_a} \rightarrow \omega = \omega_x - \frac{F_{xd}}{2m\omega_x x_a} \tag{2.13}$$

where $\omega_x = \sqrt{k_x/m}$ (mechanical resonance frequency).

F_{xd} is the force due to V_{xd} and $\omega_x x_a = \dot{x}_a$.

$$\omega = \omega_x - V_{xd}\frac{V_{PM}\dfrac{dC_x}{dx}}{2m\dot{x}_a} \tag{2.14}$$

The second term in (2.14) gives a very similar expression as the scale factor expression in (2.5) which can be expressed by

$$SF = \frac{\alpha_z}{\dfrac{\partial\omega}{\partial V_{xd}}}\frac{\dfrac{dC_x}{dx}}{\dfrac{dC_y}{dy}} \tag{2.15}$$

Using (2.15), the angular rate can be written as

$$\Omega = V_{yv}\cdot\frac{\partial\omega}{\partial V_{xd}}\cdot\frac{1}{\alpha_z}\cdot\frac{\dfrac{dC_y}{dy}}{\dfrac{dC_x}{dx}} \tag{2.16}$$

$\partial\omega/\partial V_{xd}$ can be dynamically measured by applying a modulated (AC) V_{xd}. Therefore, (2.16) can be rewritten as

$$\Omega = \underbrace{V_{yv}\cdot\frac{\omega_{AC}}{V_{xd,AC}}}_{\text{Ratio-metric readout}}\underbrace{\cdot\frac{1}{\alpha_z}\cdot\frac{\dfrac{dC_y}{dy}}{\dfrac{dC_x}{dx}}}_{1/SF_{RM}} \tag{2.17}$$

As it is shown in (2.17), the first part of the angular rate expression is continuously measured. It can be considered as a new output, and the second part can be considered as the inverse of the scale factor of the ratio-metric force feedback sensing.

SF_{RM} is equal to angular gain (α_z) for ideal symmetric structures. This expression is same as whole angle and FM gyroscopes [25, 30]. In addition to this, the ratio-metric readout technique still works for asymmetric structures, since the scale factor now depends only on a ratio of the spatial derivatives of the forcer electrodes in addition to α_z.

Equation 2.17 can also be generalized for gyroscopes with different transduction gains (η_x and η_y).

$$\Omega = \underbrace{S_{yv}\cdot\frac{\omega_{AC}}{S_{xd,AC}}}_{\text{Ratio-metric readout}}\underbrace{\cdot\frac{1}{\alpha_z}\cdot\frac{\eta_y}{\eta_x}}_{1/SF_{RM}} \tag{2.18}$$

where S_{**} refers to signal which can be voltage (V) for capacitive and piezoelectric transducers and current (I) for magnetic transducers.

The effect of the ADC is also eliminated in the ratio-metric force feedback if the same type of ADC and same V_{ref} are used for the voltage which modulates the drive mode resonance frequency. In this case, the scale factor expression will be independent of the ADC reference voltage, and only the matching of the ADCs appears in the scale factor expression. Equation 2.19 shows the overall scale factor expression between the angular rate and digital code.

$$\Omega = \underbrace{D_{yv} \cdot \frac{\omega_{AC}}{D_{xd,AC}}}_{\text{Ratio-metric readout}} \underbrace{\cdot \frac{1}{\alpha_z} \cdot \frac{\frac{dC_y}{dy}}{\frac{dC_x}{dx}}}_{1/SF_{RM}} \cdot \frac{A_{conv1}}{A_{conv1}} \tag{2.19}$$

where A_{conv1} and A_{conv2} are the ADC gains for V_{xd} and V_{yv}, respectively. If the controller is implemented digitally, A_{conv1} and A_{conv2} are now the DAC gains for V_{yv} and V_{xd}, respectively.

2.1.4 Practical Issues

The assumptions, which were made above, cause some errors in the practical implementations. These errors and solutions to them will be discussed below.

Nonlinearity in SF Estimate: In (2.12) it was assumed that mechanical spring constant is much higher than the electrostatic spring constant. However, ω_{AC} should be high enough to have a better estimation for the scale factor. In this case, higher order terms in Taylor series should be taken into account. Fortunately, peak-to-peak measurement for ω_{AC} eliminates the even order terms. As a result, in order to have a sub-1 ppm non-linearity error, peak-to-peak frequency deviation can be set to 500ppm of the natural frequency of the drive mode.

Frequency Measurement: There are several approaches for frequency measurement. One of the easiest method is to use a high-resolution counter whose clock can be generated by typical quartz or MEMS oscillators. This kind of frequency readout can be considered as a first order $\Sigma\Delta$ modulator [31] whose frequency noise due to the quantization error can be very low with reasonable clock frequencies.

The ultimate accuracy of the scale factor of the ratio-metric force feedback is determined by the reference clock. Precision oscillators, which have sub-ppm level accuracy, can be used for this clock [32]. This amount of accuracy is good enough for navigation grade applications. Furthermore, if the same clock is used for rate integration, the obtained result will be free from the stability of the reference clock.

Drift of ω_x: ω_x is not a constant parameter, and it drifts with temperature and stress. The rate of the oscillation frequency change should be high enough to eliminate the effect of this drift on the scale factor estimation.

Drive mode without amplitude control: If the settling time is not a concern, the amplitude control can be removed from Figure 2.3. This does not change the result, since the proposed ratio-metric readout is inherently free from the velocity. As a result, the proposed approach even simplifies the drive mode implementation by removing several blocks such as demodulator, low pass filter, and controller. The overall structure can be implemented by using only a preamp, phase shifter, and limiter.

Change in the base-band dynamics of the sense mode: The sense mode is not affected by the change of the drive mode frequency with an ideal controller. Nevertheless, the low frequency errors are shaped by the frequency split and damping of the sense mode. If there is a systematic error in the controller, it will cause a significant tone at the output. It is important to null these offsets in the control loop.

Mode-matching: If the gyroscope is required to operate in mode-matched condition, the drive mode oscillation frequency should always be close enough to the sense mode resonance frequency. Therefore, it is needed to keep peak-to-peak frequency deviation below the mechanical bandwidth to take advantage of mode matching

Nonlinearities in dC_x/dx: The scale factor of the ratio-metric force feedback depends on the ratio between the spatial derivative of the capacitances of the forcer electrodes in the drive and sense channels. There is no motion in the sense channel, so that there is no non-linearity. On the other hand, dC_x/dx term may suffer from non-linearity. Comb-drive electrodes are usually used to operate the gyroscopes with a larger displacement. They are also inherently linear actuators, but if the displacement is too large then dC_x/dx might change due to the displacement dependent parasitic capacitances. Therefore, the displacement amount in the drive mode should be optimized to get accurate scale factor.

2.1.5 Test Results

Scale factor calibration was tested with two different type of sensor. First, it was demonstrated by a capacitive MEMS transducer. Although this sensor has a comb-drive transduction, the tip capacitances cause non-linearity. This causes mismatch in the drive and sense transduction gains which limits the performance of scale factor calibration method.

Second, this method is also demonstrated by a magnetic sensor (CRS07) which has inherently linear transduction. This avoid the aforementioned problem.

2.1.5.1 Capacitive Transducer

The ratio-metric readout technique is first verified using a pendulum MEMS gyroscope whose photograph is shown in Figure 2.4. The sensor is fabricated in the Invensense Nasiri fabrication process [33]. The resonance frequency of this gyroscope is 3 kHz, and the quality factor is 1000. The controllers and signal processing algorithms are implemented using Labview and PXI 7854R.

To verify the effectiveness of the calibration method, turn-on scale factor repeatability tests were carried out. The scale factor was measured twice per minute

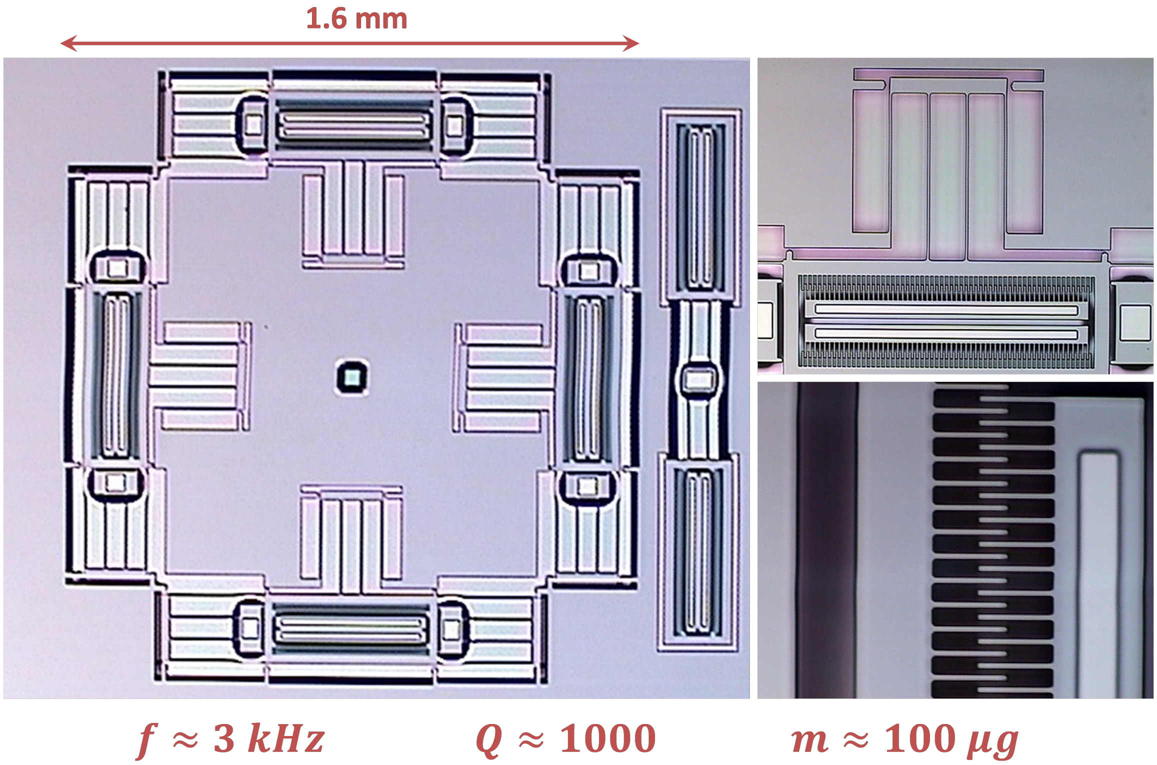

Figure 2.4. Photograph of the pendulum gyroscope used in the tests [3].

by applying angular rates of 0 dps, 100 dps, and -100 dps. This test was repeated for 28 minutes. The data in the first two minutes was removed to eliminate the settling errors coming from the signal processing algorithms. After that, measured scale factors were averaged to reduce the noise in the measurement. The supply was tuned off for 2 minutes. This 30 minutes procedure was repeated for a one-day period. Both the traditional and ratio-metric force feedback data were collected from the same gyroscope output simultaneously. The systematic offsets in the sense mode controllers were nulled to avoid the tones which have been mentioned before. As a final note, the test environment did not have a temperature control.

After the supply was turned on, the scale factor of the traditional force feedback gyroscope changes considerably. This turn-on transient was suppressed substantially using the ratio-metric force feedback technique as shown in Figure 2.5.

Figure 2.6 shows the turn-on scale factor repeatability test. A peak-to-peak drift of 2660 ppm was obtained over one day with the traditional force feedback. This value was reduced to 130 ppm using ratio-metric force feedback. These tests demonstrate 20-folds improvement in the scale factor accuracy.

The measured nominal scale factor is 0.924, and the expected angular slip factor of the sensor under test is 0.95. This gain is a robust parameter which does not

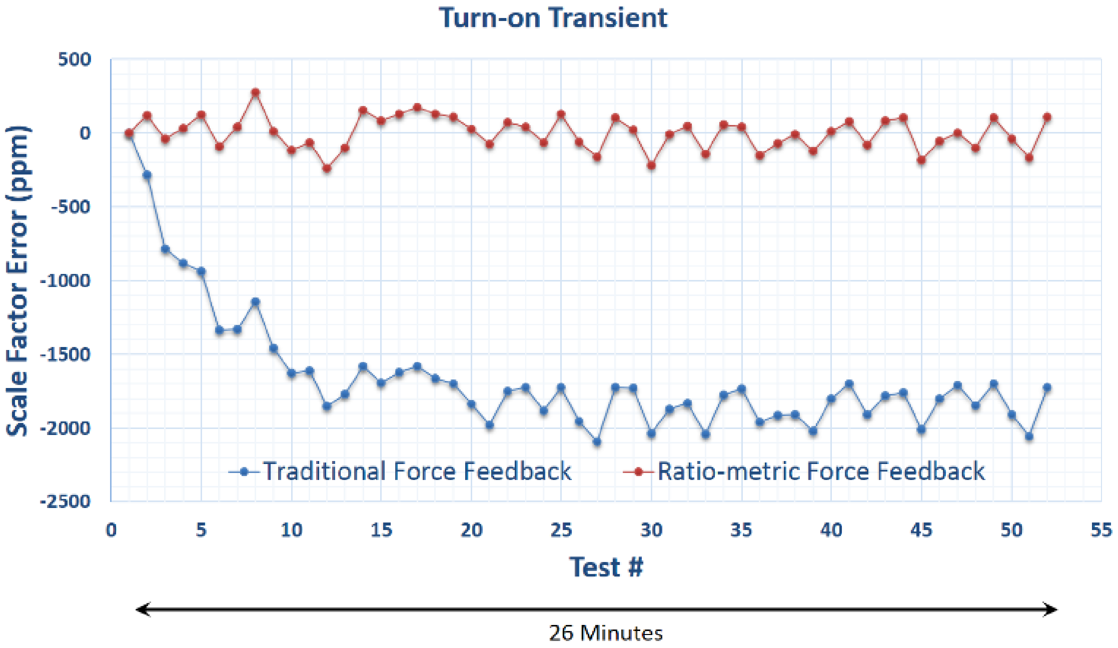

Figure 2.5. Turn-on transient test with traditional and ratio-metric force feedback operations.

vary too much with temperature and process variations. The difference between the measured scale factor and angular slip factor is coming from the mismatch between the dC_x/dx and dC_y/dy terms which can be measured on-chip. This result implies that ratio-metric force feedback gyroscopes can be used without any scale factor calibration.

The ratio-metric force feedback gyroscope has fundamentally the same noise as traditional force feedback gyroscopes. The only modification is implemented in the drive mode. The sense mode, which has the critical signal path determining the noise, has no change. The noise on the scale factor estimate is important, but it does not carry any high bandwidth information. The noise on the frequency measurement was suppressed by the low pass filters whose cut-off frequency is much smaller than the rate bandwidth. Figure 2.7 shows an Allan deviation test with an angle random walk of 5.3 mdps/rt-Hz and a bias stability of 3 deg/hr.

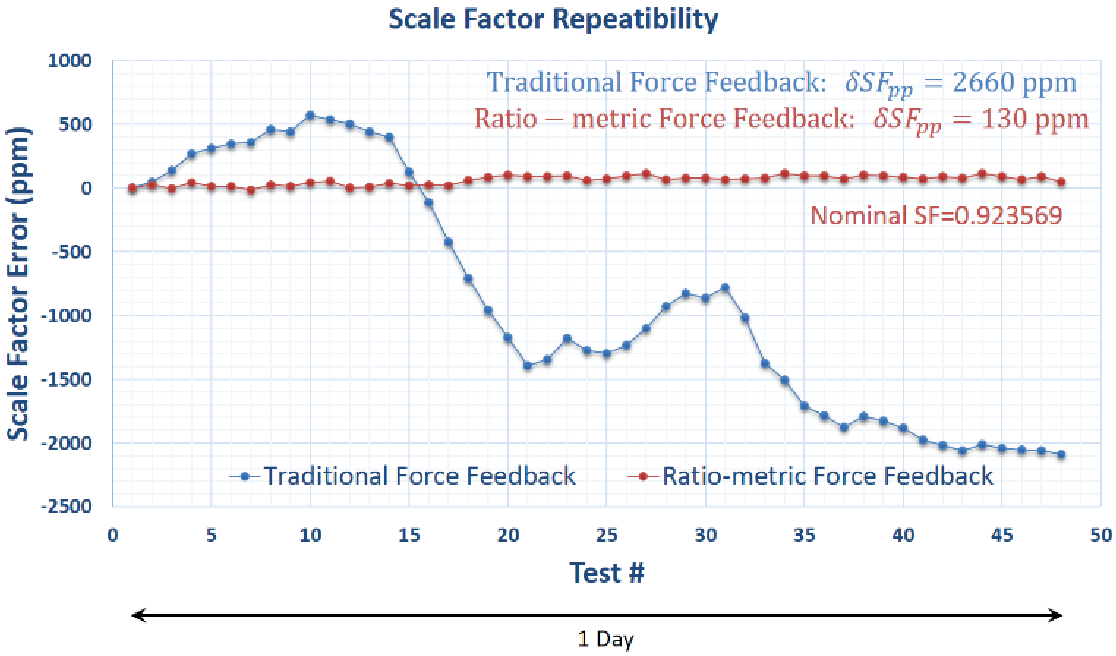

Figure 2.6. Scale factor repeatability test with traditional and ratio-metric force feedback operations.

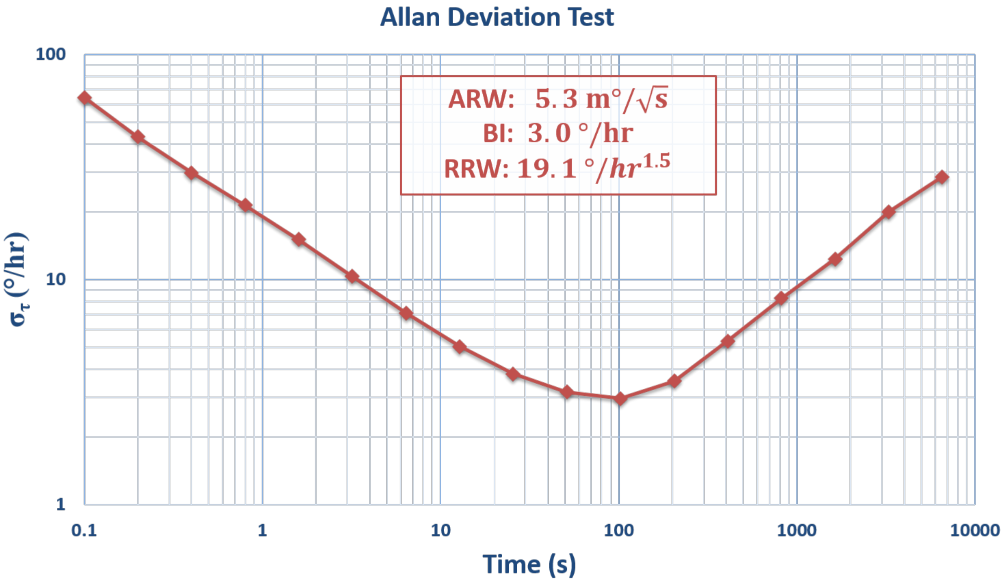

Figure 2.7. Allan deviation test with ratio-metric force feedback.

2.1.5.2 Magnetic Transducer

The linearity of the magnetic transducer is better than capacitive transducers. As a result, the transduction gains between drive and sense modes match better, and the scale-factor calibration method is more effective.

To verify this, a sensor module of a commercial gyroscope with magnetic transduction is used [34]. Figure 2.8 shows the device photo with transducer parameters.

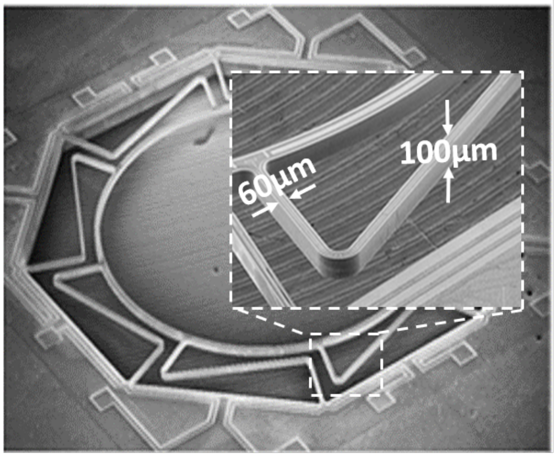

Ring Diameter	6mm
Resonance Frequency	14kHz
Mechanical Frequency Mismatch	80mHz
Q-factor	4700

Figure 2.8. Device photo with transducer parameters [4].

Figure 2.9 shows the long-term repeatability of the scale factor measured over 12 days. Background calibration reduces the peak-to-peak deviation by a factor of 24 from 547ppm to 23ppm whose 1σ deviation is only 7ppm.

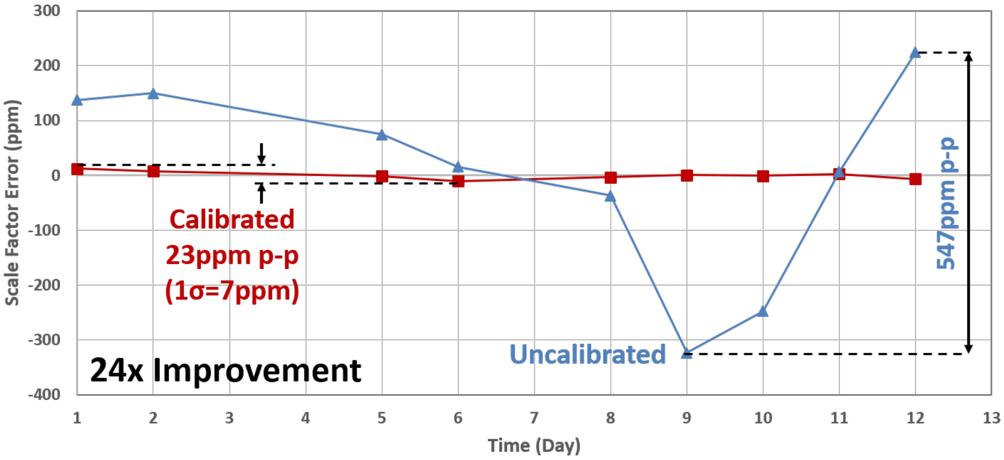

Figure 2.9. Repeatability of the scale factor measured over 12 days.

Figure 2.10 demonstrates the temperature sensitivity of the scale factors for both calibrated and uncalibrated outputs. It has been shown that the overall deviation of the scale factor over 30°C temperature range is reduced from 18700ppm to 61ppm which is more than 300 times improvement. The temperature coefficient of the scale factor at room temperature is also decreased from 560ppm/°C to 4ppm/°C. It has been observed that the temperature sensitivity becomes zero around 35°C.

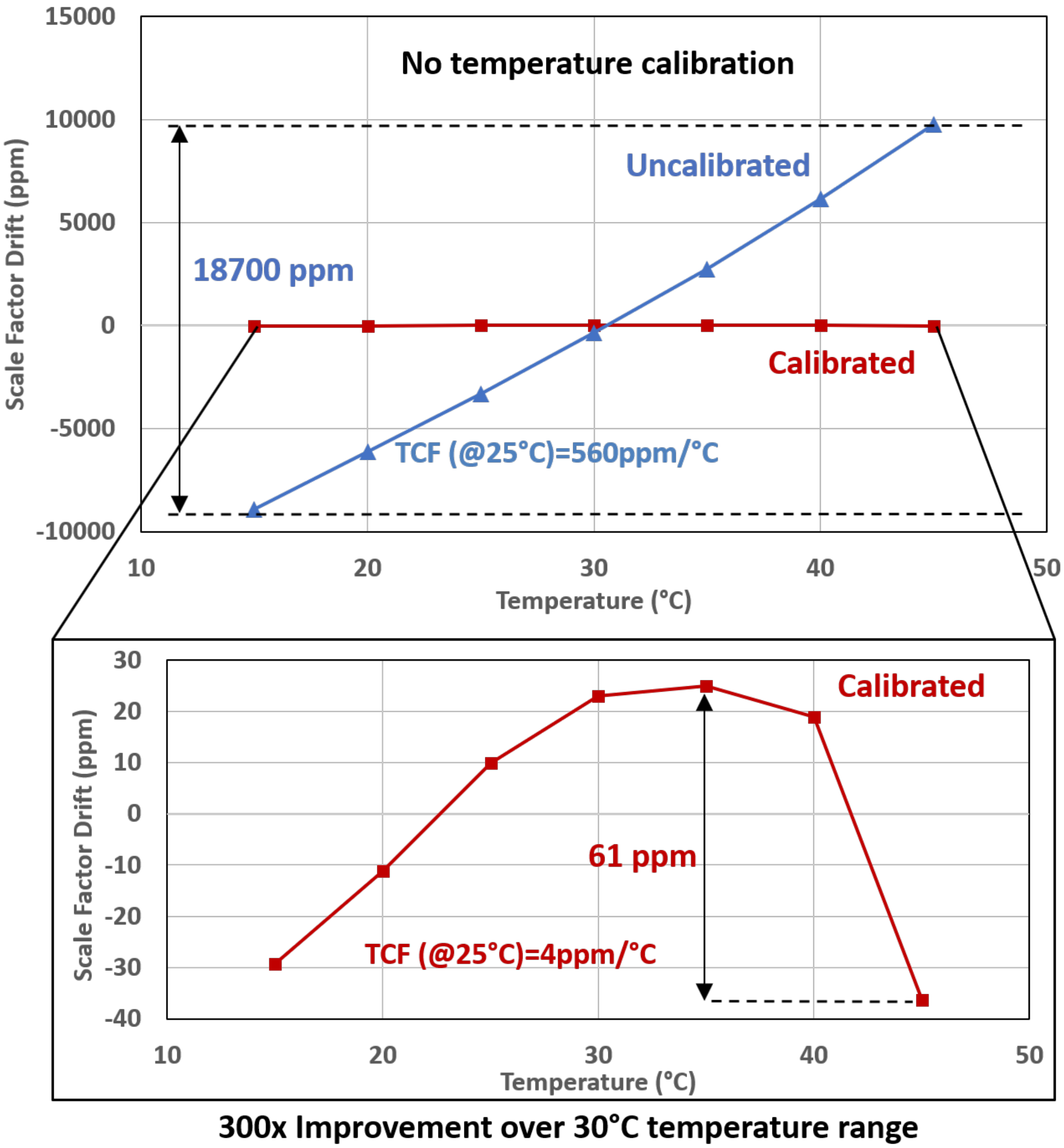

Figure 2.10. Scale factor measurements between 15°C and 45°C.

These results imply that the scale factor estimation is very accurate. As it is mentioned in (2.18), the only errors are coming from $\alpha_z\eta_x/\eta_y$. First, the angular gain (α_z) is known to be very stable, but it still presents temperature dependency. The temperature coefficient of the angular gain in hemi-spherical ring gyroscopes (HRGs) is reported as 0.5ppm/°C [8]. Second, η_x/η_y is a ratio of transduction gains. If the structure is symmetric, this ratio will be more balanced and reject most of the common disturbances in $\eta_{x,y}$. However, in practice $\eta_{x,y}$ depends on displacement, and η_x and η_y have different dynamics due to the inherent asymmetrical operation of conventional force feedback. While η_y does not have any displacement dependency because there is no motion in the y-channel, η_x suffers from this dependency if there is any transduction non-linearity. Magnetic transducers do not have this problem thanks to its linear transduction which is the main reason the accurate scale factor shown in Figure 2.10 could be obtained.

2.2 Background Calibration for Bias Stability

Bias instability is the limiting factor for long-term applications. As mentioned before, there are three main error sources for bias stability which can be grouped under 2 categories: (1) quadrature error and (2) in-phase errors due to anisodamping and force coupling. This section discusses two approaches to suppress these errors for force-feedback gyroscopes.

2.2.1 Quadrature Error Suppression

For quadrature coupling, direct cancellation of this error is the most common techniques for bias correction [5]. But, this method is not always possible due to the necessity of dedicated quadrature cancellation electrodes. Alternatively, phase error in the electronics can also be calibrated so that quadrature error is eliminated precisely with phase sensitive demodulation.

In force feedback gyroscopes, the critical signal path is the feedback network of the sense channel which includes the modulators as shown in Figure 2.11. The carriers of these modulators come from the drive channel. Because the quadrature leakage happens due to the phase errors in these carriers, the phase error of the drive channel needs to be measured and corrected. The front-end electronics phase error (θ_{err}) in the drive mode is the dominant error source.

Figure 2.11 shows the simplified block diagram of the force feedback gyroscopes with the injected calibration signal used for scale factor calibration. *Note: In this section S_{**}, which refers to electrical signal, is used instead of voltage or current to generalize the expressions for different types of transducers.*

Equation 2.20 shows that the actuating force F_{xv} of the drive channel sets the amplitude of the oscillator, and this force should balance the damping force to sustain the oscillation. However, (2.20) is not accurate if there is any phase error between the velocity and force. If this is the case, F_{xv} will have two components which are

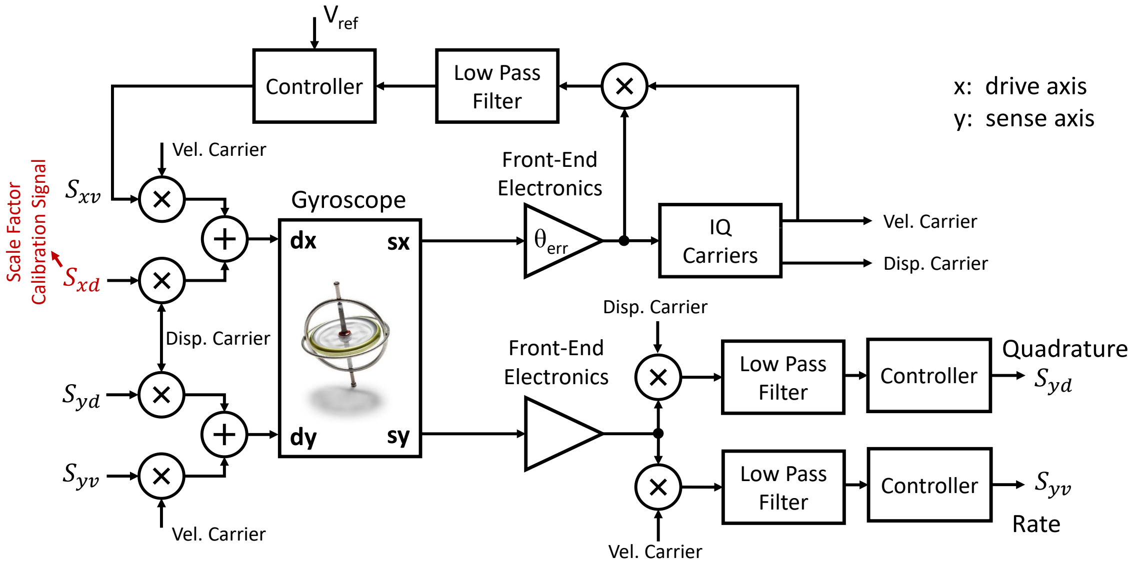

Figure 2.11. Simplified block diagram for force-feedback gyroscopes.

in-phase with displacement and velocity instead of a single force, which is in-phase with the velocity. A similar situation also holds for F_{xd}.

$$\begin{aligned} m\ddot{x} + b_x\dot{x} + k_x x = {} & (F_{xv}\cos(\theta_{err}) - F_{xd}\sin(\theta_{err}))\frac{\dot{x}}{\dot{x_a}} \\ & + (F_{xd}\cos(\theta_{err}) + F_{xv}\sin(\theta_{err}))\frac{x}{x_a} \end{aligned} \tag{2.20}$$

In order to have sustaining oscillation with an amplitude of x_a, the following conditions should be met.

$$\begin{aligned} b_x x_a \omega_{osc} &= F_{xv}\cos(\theta_{err}) - F_{xd}\sin(\theta_{err}) \\ \frac{b_x x_a}{\eta_x}\omega_{osc} &= S_{xv}\cos(\theta_{err}) - S_{xd}\cdot\sin(\theta_{err}) \end{aligned} \tag{2.21}$$

Equation 2.21 is a single equation with two unknowns: $b_x x_a/\eta_x$ and θ_{err}. On the other hand, S_{xd} and so F_{xd} are AC signals to modulate the oscillation frequency for scale factor calibration. Therefore, (2.21) can be divided into two new equations for DC and AC terms using superposition.

$$\begin{aligned} \frac{b_x x_a}{\eta_x}\omega_{osc,DC} &= S_{xv,DC}\cos(\theta_{err}) - S_{xd,DC}\sin(\theta_{err}) \\ \frac{b_x x_a}{\eta_x}\omega_{osc,AC} &= S_{xv,AC}\cos(\theta_{err}) - S_{xd,AC}\sin(\theta_{err}) \end{aligned} \tag{2.22}$$

$S_{xd,DC}$ is equal to 0, since the calibration force and electrical signal are pure AC to modulate the oscillation frequency. Therefore, the phase error θ_{err} can be found as follows.

$$\theta_{err} = \frac{S_{xv,AC} - S_{xv,DC}\dfrac{\omega_{osc,AC}}{\omega_{osc,DC}}}{S_{xd,AC}} \tag{2.23}$$

Equation 2.23 shows that the phase error can easily be obtained by using the oscillation frequency and drive signals in the drive channel. After this phase error is obtained, the force vector of $[F_{yv}\ F_{xv}]^T$ can be rotated to eliminate the quadrature leakage. The same thing can also be done for the electrical signals S_{yv} and S_{yd} which are used to generate the feedback forces as follows.

$$\begin{bmatrix}\tilde{S}_{yv}\\ \tilde{S}_{xv}\end{bmatrix} = \begin{bmatrix}\cos(\theta_{err}) & -\sin(\theta_{err})\\ \sin(\theta_{err}) & \cos(\theta_{err})\end{bmatrix}\begin{bmatrix}S_{yv}\\ S_{xv}\end{bmatrix} = \frac{1}{\eta_y}\cdot\begin{bmatrix}2m\alpha_z x_a \omega_{osc}\left(\Omega + \dfrac{b_{xy}}{2m\alpha_z}\right)\\ k_{xy}x_a\end{bmatrix} \tag{2.24}$$

Equation 2.24 shows that $\tilde{S}_{yv}$ is now free from the quadrature error, and the only errors left are due to the in-phase errors.

2.2.2 In-phase Error Correction

Errors like anisotropic damping shown in (2.24) and force coupling have the same phase as the Coriolis force [11]. The amount of force coupling is directly related to the amount of the electrical signal applied at the forcer electrodes in the drive channel (S_{xv}). Similarly, anisotropic damping (b_{xy}) is related to the isotropic damping (b_x), and the actuating electrical signal in the drive channel is a function of isotropic damping as shown in (2.22). Therefore, the in-phase error term (e_{in}) can be expressed in terms of S_{xv}.

$$e_{in} = S_{xv}\cdot\zeta_{cal} \tag{2.25}$$

where ζ_{cal} is a correlation coefficient between the actuating signal in the drive channel and in-phase errors. ζ_{cal} can be found easily, when there is no angular rate. In other words, this correlation coefficient can be extracted by one-point calibration. This method is valid as long as there is no error leakage from quadrature. This condition is automatically satisfied using the dynamic phase error correction mentioned above. As a result, ζ_{cal} can be extracted as follows:

$$\zeta_{cal} = \left.\frac{\tilde{S}_{yv}}{S_{xv}}\right|_{\Omega=0} \tag{2.26}$$

In brief, the overall background calibration can be summarized as follows:

$$\begin{bmatrix}\Omega\\ \Omega_q\end{bmatrix} = \frac{1}{\alpha_z}\frac{\eta_y}{\eta_x}\frac{\omega_{AC}}{S_{xd,AC}} \cdot \left(\begin{bmatrix}\cos(\theta_{err}) & -\sin(\theta_{err})\\ \sin(\theta_{err}) & \cos(\theta_{err})\end{bmatrix}\begin{bmatrix}S_{yv}\\ S_{xv}\end{bmatrix} - \begin{bmatrix}S_{yv}\\ 0\end{bmatrix}\left.\frac{\tilde{S}_{yv}}{S_{xv}}\right|_{\Omega=0}\right) \qquad (2.27)$$

where, Ω_q is the rate equivalent quadrature error. In (2.27), $\frac{1}{\alpha_z}\frac{\eta_y}{\eta_x}$ can be considered as inverse of the scale factor of the overall background calibrated system. All the other parameters in (2.27) are observable parameters, and the uncertainty in the rate estimate is minimized by the proposed background calibration methods.

2.2.3 Test Results

The above calibration techniques were also tested with the magnetic transducer used in the scale factor calibration method.

Figure 2.12 shows the measured Allan Variance. The Angular Random Walk of 0.035 deg/rt-hr is dominated by pickup noise and not affected by calibration. The dynamic phase error correction described above reduces the bias for 400s averaging time two-fold. At 3200s, relevant for short-term navigation, the error decreases from 5.7deg/hr to 3.3deg/hr. Combining all proposed calibration approaches achieves better than a six-fold improvement at 400s. At 3200s, drift is reduced from 5.7deg/hr to 2deg/hr, thus attaining tactical grade performance.

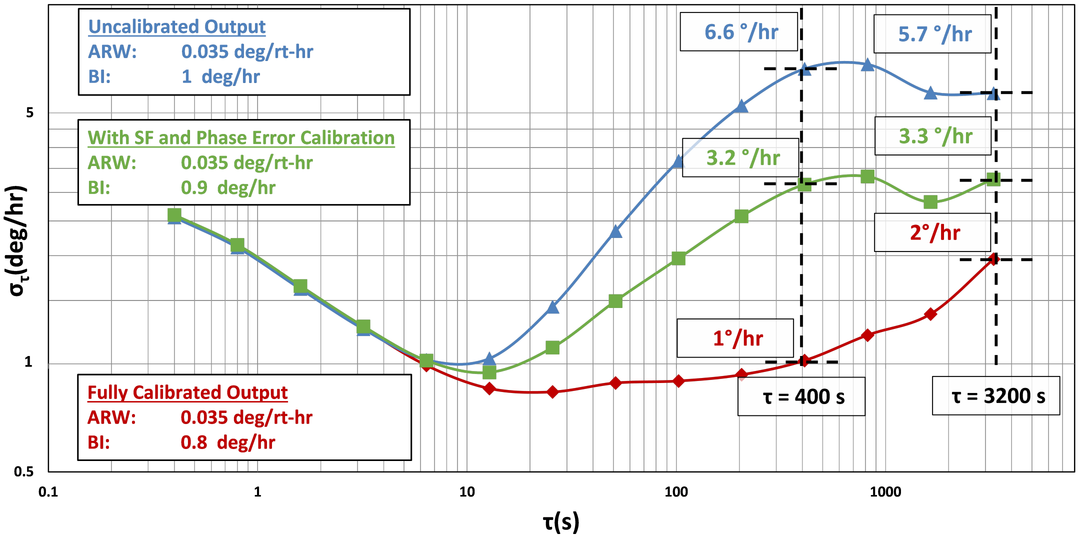

Figure 2.12. Allan deviation results for uncalibrated and calibrated outputs.

Figure 2.13 shows the bias measurement results over 30°C temperature range. The temperature-coefficient of the bias is decreased from 32mdps/°C to 8mdps/°C with the background calibration.

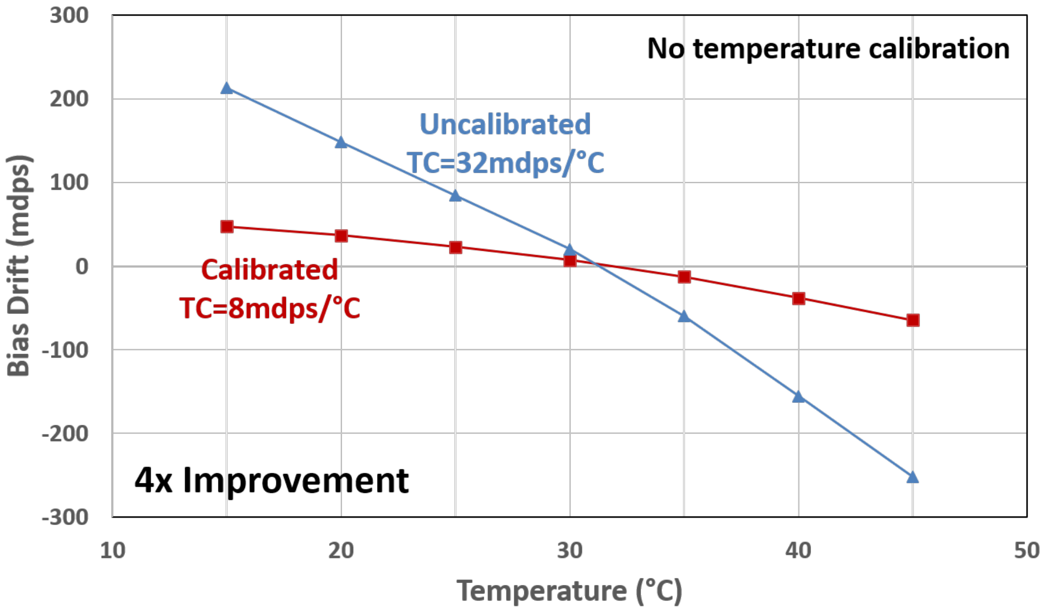

Figure 2.13. Temperature test results of bias for uncalibrated and calibrated outputs.

2.3 Conclusion

This chapter presents three calibration techniques, which calibrate scale factor and bias at the background. The detailed tests of the scale factor calibration demonstrate that the long-term repeatability improves from 547ppm to 23ppm, and the first order temperature-coefficient of the scale factor at room temperature drops from 560ppm/°C to 4ppm/°C, showing more than two orders of magnitude improvement. The bias calibration includes two different approaches. First, the phase error in the system is continuously monitored, and quadrature leakage to the output is corrected using this estimated phase error. Second, in-phase errors are corrected by using the actuating electrical signal in the drive channel. These bias calibration techniques reduce the bias instability by a factor of approximately 7 from 6.6deg/hr to 1deg/hr at 400s, and the temperature coefficient by a factor of 4 from 32mdeg/s/°C to 8mdeg/s/°C.

Chapter 3

FM Gyroscope Dynamics

In FM gyroscopes, the angular rate modulates the frequency instead of amplitude [30]. This modulated frequency is sensed by a frequency-to-digital (FDC) converter with a precision reference clock. Since angular rate itself is also frequency, this kind of ratio-metric readout inherently has much shorter signal path which minimizes the error terms appearing in the scale factor and bias [24].

In conventional gyroscopes, while the first channel is operating as an oscillator, the second channel is only used as a sense element. However, FM gyroscopes use both of the axes as an oscillator. In fact, as it will be shown later, using both channels as an oscillator is not only necessary for FM gyroscopes, but also provides unique features for AM gyroscopes.

This chapter covers the dynamics of coupled oscillators acting as a gyroscope and the effect of error sources.

3.1 Gyroscope as a Coupled Oscillator

The electro-mechanical matrices for a 2-DOF oscillator are described below.

$$
\begin{gathered}
M=\begin{bmatrix} m_{xx} & 0 \\ 0 & m_{yy} \end{bmatrix},\ B=\begin{bmatrix} b_{xx} & b_{xy} \\ b_{yx} & b_{yy} \end{bmatrix},\ K=\begin{bmatrix} k_{xx}+\xi_x k_{tune} & k_{xy} \\ k_{yx} & k_{yy}-\xi_x k_{tune} \end{bmatrix}, \\
O=\begin{bmatrix} 0 & 2m\Omega\alpha_z \\ -2m\Omega\alpha_z & 0 \end{bmatrix},\ T_\lambda=\begin{bmatrix} 1 & \lambda_{xy} \\ \lambda_{yx} & 1 \end{bmatrix},\ q=\begin{bmatrix} x \\ y \end{bmatrix},\ F=\begin{bmatrix} F_{xv}\dfrac{\dot{x}}{\dot{x}_a}+F_{xd}\dfrac{x}{x_a} \\ F_{yv}\dfrac{\dot{y}}{\dot{y}_a}+F_{yd}\dfrac{y}{y_a} \end{bmatrix}
\end{gathered}
\tag{3.1}
$$

where M, B, and K are mass, damping, and sensor matrices. k_{tune} is the controllable spring constant used for tuning purpose. $\xi_{x,y}$ is the weights for tuning. O is the rate matrix, T_λ is the force coupling matrix, q is the position vector, and F is the forcer vector. x_a, $\dot{x}_a$, y_a, and $\dot{y}_a$ are the oscillation amplitudes for the displacement and velocity signals.

The equations of motion in matrix form are written as

$$H = M\ddot{q} + (B + O)\dot{q} + Kq - T_\lambda F \tag{3.2}$$

where H is a equivalent force vector with the components below.

$$\begin{aligned} H_1 =& m_{xx}\ddot{x} + \left(b_{xx} - \frac{F_{xv}}{\dot{x}_a}\right)\dot{x} + \left(k_{xx} - \frac{F_{xd}}{x_a} + \xi_x k_{tune}\right)x \\ &+ \left(k_{xy} - \frac{\lambda_{xy}F_{yd}}{y_a}\right)y + \left(b_{xy} + 2m\Omega\alpha_z - \frac{\lambda_{xy}F_{yv}}{\dot{y}_a}\right)\dot{y} \end{aligned} \tag{3.3}$$

$$\begin{aligned} H_2 =& m_{yy}\ddot{y} + \left(b_{yy} - \frac{F_{yv}}{\dot{y}_a}\right)\dot{y} + \left(k_{yy} - \frac{F_{yd}}{y_a} - \xi_y k_{tune}\right)y \\ &+ \left(k_{yx} - \frac{\lambda_{yx}F_{xd}}{x_a}\right)x + \left(b_{yx} - 2m\Omega\alpha_z - \frac{\lambda_{yx}F_{xv}}{\dot{x}_a}\right)\dot{x} \end{aligned} \tag{3.4}$$

This expression indicates that the coupling forces can modulate the effective damping (b^*) and stiffness (k^*) terms depending on their phase with respect to the displacement. If the coupled force is in-phase with the displacement, it modulates the stiffness. If it is in-phase with the velocity, it modulates the damping.

For an arbitrary phase difference between the x and y channel displacement signals (ϕ_{xy}), the coupling forces can be decomposed into the displacement and velocity signals of the corresponding oscillator. Figure 3.1 shows the projection of the normalized coupled signals (y/y_a) and ($\dot{y}/\dot{y}_a$) to the normalized displacement (x/x_a) and velocity signals ($\dot{x}/\dot{x}_a$).

Using these relations, the coupled signals can be rewritten as below.

$$\begin{aligned} y &= x\frac{y_a}{x_a}\cos(\phi_{yx}) + \dot{x}\frac{y_a}{\dot{x}_a}\sin(\phi_{yx}) \\ \dot{y} &= \dot{x}\frac{\dot{y}_a}{\dot{x}_a}\cos(\phi_{yx}) - x\frac{\dot{y}_a}{x_a}\sin(\phi_{yx}) \\ x &= y\frac{x_a}{y_a}\cos(\phi_{xy}) + \dot{y}\frac{x_a}{\dot{y}_a}\sin(\phi_{xy}) \\ \dot{x} &= \dot{y}\frac{\dot{x}_a}{\dot{y}_a}\cos(\phi_{xy}) - y\frac{\dot{x}_a}{y_a}\sin(\phi_{xy}) \end{aligned} \tag{3.5}$$

Using (3.3), (3.4), and (3.5), the dynamics can be explained as

$$\begin{aligned} m_{xx}\ddot{x} + b_x^*\dot{x} + k_x^*x = 0 \\ m_{yy}\ddot{y} + b_y^*\dot{y} + k_y^*x = 0 \end{aligned} \tag{3.6}$$

where $b_{x,y}^*$ and $k_{x,y}^*$ are the effective damping and spring constant terms

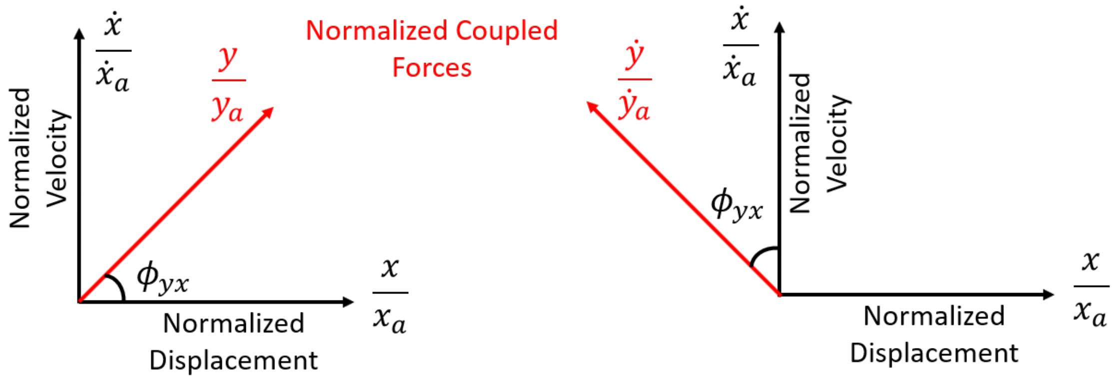

$$\phi_{yx} = \phi_y - \phi_x = -\phi_{xy}$$

$$\frac{y}{y_a} = \frac{x}{x_a}\cos(\phi_{yx}) + \frac{\dot{x}}{\dot{x}_a}\sin(\phi_{yx}) \qquad \frac{\dot{y}}{\dot{y}_a} = -\frac{x}{x_a}\sin(\phi_{yx}) + \frac{\dot{x}}{\dot{x}_a}\cos(\phi_{yx})$$

Figure 3.1. Projection of coupled forces for an arbitrary ϕ_{xy} difference.

$$\begin{aligned} k_x^* =& k_{xx} - \frac{F_{xd}}{x_a} + \xi_x k_{tune} + \frac{y_a}{x_a} k_{xy}\cos(\phi_{xy}) - \frac{F_{yd}}{x_a}\lambda_{xy}\cos(\phi_{xy}) \\ & - \frac{F_{yv}}{x_a}\lambda_{xy}\sin(\phi_{xy}) + \frac{\dot{y}_a}{x_a} b_{xy}\sin(\phi_{xy}) + 2m\Omega\alpha_z\frac{\dot{y}_a}{x_a}\sin(\phi_{xy}) \end{aligned} \tag{3.7a}$$

$$\begin{aligned} k_y^* =& k_{yy} - \frac{F_{yd}}{y_a} - \xi_y k_{tune} + \frac{x_a}{y_a} k_{yx}\cos(\phi_{yx}) - \frac{F_{xd}}{y_a}\lambda_{yx}\cos(\phi_{yx}) \\ & - \frac{F_{xv}}{y_a}\lambda_{yx}\sin(\phi_{yx}) + \frac{\dot{x}_a}{y_a} b_{yx}\sin(\phi_{yx}) + 2m\Omega\alpha_z\frac{\dot{x}_a}{y_a}\sin(\phi_{yx}) \end{aligned} \tag{3.7b}$$

$$\begin{aligned} b_x^* =& b_{xx} - \frac{F_{xv}}{\dot{x}_a} - \frac{F_{yv}}{\dot{x}_a}\lambda_{xy}\cos(\phi_{xy}) + \frac{\dot{y}_a}{\dot{x}_a} b_{xy}\cos(\phi_{xy}) \\ & - \frac{y_a}{\dot{x}_a} k_{xy}\sin(\phi_{xy}) + \frac{F_{yd}}{\dot{x}_a}\lambda_{xy}\sin(\phi_{xy}) + \frac{\dot{y}_a}{\dot{x}_a} 2m\Omega\alpha_z\cos(\phi_{xy}) \end{aligned} \tag{3.7c}$$

$$\begin{aligned} b_y^* =& b_{yy} - \frac{F_{yv}}{\dot{y}_a} - \frac{F_{xv}}{\dot{y}_a}\lambda_{yx}\cos(\phi_{yx}) + \frac{\dot{x}_a}{\dot{y}_a} b_{yx}\cos(\phi_{yx}) \\ & - \frac{x_a}{\dot{y}_a} k_{yx}\sin(\phi_{yx}) + \frac{F_{xd}}{\dot{y}_a}\lambda_{yx}\sin(\phi_{yx}) + \frac{\dot{x}_a}{\dot{y}_a} 2m\Omega\alpha_z\cos(\phi_{yx}) \end{aligned} \tag{3.7d}$$

Note that (3.6) and (3.7) have only one assumption: ϕ_{xy} is a slowly varying signal. In these equations we have 4 equations with 4 unknowns. These unknowns are the sustaining forces and oscillation frequencies.

3.2 Force Sensing

The sustaining force expressions can be found by using $b^*_{x,y}$ terms. In order to have sustaining oscillations, $b^*_{x,y}$ should be equal to zero. Neglecting the higher order error terms such as $\lambda_{xy}\lambda_{yx}$, F_{xv} and F_{yv} can be found as

$$\begin{aligned} F_{xv} =& b_{xx}\dot{x}_a + (F_{yd}\lambda_{xy} - y_a k_{xy})\sin(\phi_{xy}) \\ &+ (b_{xy}\dot{y}_a - b_{yy}\lambda_{xy}\dot{y}_a + 2m\Omega\alpha_z\dot{y}_a)\cos(\phi_{xy}) \end{aligned} \tag{3.8a}$$

$$\begin{aligned} F_{yv} =& b_{yy}\dot{y}_a - (F_{xd}\lambda_{yx} - x_a k_{yx})\sin(\phi_{xy}) \\ &+ (b_{yx}\dot{x}_a - b_{xx}\lambda_{yx}\dot{x}_a - 2m\Omega\alpha_z\dot{x}_a)\cos(\phi_{xy}) \end{aligned} \tag{3.8b}$$

Equation 3.8 shows the two channels have opposite rate sensitivity. If the velocities are matched $\dot{x}_a = \dot{y}_a = \dot{r}_a$, we can simply get the difference as follows.

$$\begin{aligned} \Delta F =& (b_{xx} - b_{yy})\dot{r}_a + (F_{xd}\lambda_{yx} - y_a k_{xy} - x_a k_{yx} + F_{yd}\lambda_{xy})\sin(\phi_{xy}) \\ &+ (b_{xy} - b_{yx} + b_{xx}\lambda_{yx} - b_{yy}\lambda_{xy} + 4m\Omega\alpha_z)\,\dot{r}_a\cos(\phi_{xy}) \end{aligned} \tag{3.9}$$

For a symmetrical device with equal cross-axis error terms such as $b_{xy} = b_{yx}$ and $F_{xd,yd} = 0$ simplifies to Equation 3.9 to

$$\Delta F = (b_{xx} - b_{yy})\dot{r}_a - (y_a k_{xy} + x_a k_{yx})\sin(\phi_{xy}) + (4m\Omega\alpha_z)\,\dot{r}_a\cos(\phi_{xy}) \tag{3.10}$$

Here, if $\phi_{xy} = \{0^\circ, 180^\circ\}$, the rate sensitivity is maximized. In this case, the bias error is set by the damping mismatch instead of anisotropic damping as in conventional gyroscopes. But, this is still a limitation for high performance operation. This limitation can be overcome by alternating the phase difference between 0° and 180°. This can be implemented using additional PLL or DLL loops, or simply letting the oscillators run at their natural frequencies with a mode split of Δf which will automatically modulate the rate signal. The mode-split should be minimized to reduce noise, but it should also be high enough to reject the drift due to $b_{xx} - b_{yy}$.

Note that this presents a new way of implementing AM gyroscopes with two new features: (1) Operating both of the channels of the gyroscope as oscillators enables continuous tracking and control of the mode-split. Therefore, the mode-split can be minimized to decrease the noise and power. (2) Alternating the phase between 0° and 180° eliminates error terms and improves the bias stability.

3.3 Frequency Sensing

The instantaneous oscillation frequency can simply be found as $\sqrt{k/m}$. It is known that the nominal oscillation frequency is set by the mechanical spring constants. Therefore, using the Taylor series expansion at the nominal resonance frequencies ($\omega_{ox,oy}$), the instantaneous oscillation frequencies can be found as

$$\omega_x = \sqrt{\frac{k_x^*}{m_{xx}}} = \omega_{ox} + \frac{k_x^*}{2m\omega_{ox}} \tag{3.11a}$$

$$\omega_y = \sqrt{\frac{k_y^*}{m_{yy}}} = \omega_{oy} + \frac{k_y^*}{2m\omega_{oy}} \tag{3.11b}$$

where $\omega_{ox,oy} = \sqrt{k_{xx,yy}/m_{xx,yy}}$. Using Equation 3.7

$$\begin{aligned}\omega_x = &\left(\alpha_z \frac{\dot{y}_a}{\dot{x}_a}\Omega - \frac{F_{yv}}{2m\dot{x}_a}\lambda_{xy} + \frac{\dot{y}_a}{2m\dot{x}_a}b_{xy}\right)\sin(\phi_{xy}) \\ &+ \left(-\frac{F_{yd}}{2m\dot{x}_a}\lambda_{xy} + \frac{\dot{y}_a}{2m\omega_{oy}\dot{x}_a}k_{xy}\right)\cos(\phi_{xy}) \\ &- \frac{F_{xd}}{2m\dot{x}_a} + \frac{\xi_x}{2m\omega_{ox}}k_{tune} + \omega_{ox}\end{aligned} \tag{3.12a}$$

$$\begin{aligned}\omega_y = &\left(\alpha_z \frac{\dot{x}_a}{\dot{y}_a}\Omega + \frac{F_{xv}}{2m\dot{y}_a}\lambda_{yx} - \frac{\dot{x}_a}{2m\dot{y}_a}b_{yx}\right)\sin(\phi_{xy}) \\ &+ \left(-\frac{F_{xd}}{2m\dot{y}_a}\lambda_{yx} + \frac{\dot{x}_a}{2m\omega_{ox}\dot{y}_a}k_{yx}\right)\cos(\phi_{xy}) \\ &- \frac{F_{yd}}{2m\dot{y}_a} - \frac{\xi_y}{2m\omega_{oy}}k_{tune} + \omega_{oy}\end{aligned} \tag{3.12b}$$

Here the rate sensitivity is the same for each channel. If there is no active tuning ($k_{tune} = 0$), then the oscillation frequencies in (3.12) should be summed if the velocities are equal. Equation 3.13 gives the summation for equal velocities and cross-axis terms, $F_{xv} = F_{yv}$, and $F_{xd,yd}$=0.

$$\Sigma\omega = 2\alpha_z\Omega\sin(\phi_{xy}) + \frac{k_{xy}}{m\omega_o}\cos(\phi_{xy}) + \omega_{ox} + \omega_{oy} \tag{3.13}$$

Equation 3.13 shows that error terms cancel each other for symmetric operation and design which confirms the intuition about less erroneous performance with symmetric operation. The DC components can be eliminated by alternating the phase between 90° and 270°. Similar to force sensing, this phase alternation can be carried out by just letting the oscillators run free with a mode-split. Until now, both force and frequency sensing for a gyroscope with dual-oscillating channels exhibit similar features in terms of bias stability and mode-split observation. However, as seen in (3.13) the scale-factor for frequency output depends only on the angular gain (α_z) which provides a significant advantage compared to force sensing.

To understand the scale factor sensitivity to oscillation amplitudes, we need to go back to (3.12). If we sum these two terms for free running oscillators (no active tuning, $k_{tune} = 0$), we get the following SF expression.

$$SF = \alpha_z \frac{1}{2} \frac{d\Sigma\omega}{d\Omega} = \frac{1}{2} \left(\frac{\dot{y}_a}{\dot{x}_a} + \frac{\dot{x}_a}{\dot{y}_a} \right) \tag{3.14}$$

Equation 3.14 shows that the FM scale factor is minimized with equal velocities, but the scale factor error due to the velocity mismatch is also minimized thanks to the reciprocal summation.

If active tuning is used to set the mode split ($k_{tune} \neq 0$), then the tuning strategy affects the common-mode frequency (ω_{cm}). This common-mode frequency is set by the tuning weights $\xi_{x,y}$.

$$\omega_{cm} = \frac{\omega_x \xi_y + \omega_y \xi_x}{\xi_x + \xi_y} \tag{3.15}$$

Then the scale factor is

$$SF = \frac{d\omega_{cm}}{d\Omega} = \alpha_z \frac{1}{\xi_x + \xi_y} \left(\frac{\dot{y}_a}{\dot{x}_a} \xi_y + \frac{\dot{x}_a}{\dot{y}_a} \xi_x \right) \tag{3.16}$$

This is an important observation that the tuning strategy is important if the errors are to be minimized as shown for scale factor. For example, if one of the channels is used as a master resonator and the second resonator is locked to this resonator such as ($\xi_x = 1$ and $\xi_y = 0$), then the scale scale factor will only be $\alpha_z \dot{x}_a / \dot{y}_a$ which does not have the reciprocal summation feature.

3.4 Phase Error in Electronics

The above analysis only covers the mechanical errors. In (3.12) and (3.13), it is clear that any phase error in the demodulation path causes both scale factor and bias errors. Since quadrature coupling is the largest error term, the phase error in the demodulation process causes significant bias error, similar to what happens in conventional AM gyroscopes.

However, the aforementioned AM and FM methods have a very significant advantage: the phase error is due to the difference of two phases, rather than the absolute error of a single phase as in conventional gyroscopes. This eliminates the use of high bandwidth electronics to minimize the phase error, hence reducing power consumption.

The error in the phase mismatch is not the only error source. Note that Equation 3.12 includes the force terms ($F_{xd,yd}$). Ideally, these force terms are zero if there is no calibration signal applied. But, if there is a phase error ($\phi_{errx,erry}$), $F_{xv,yv}$ leaks to $F_{xd,yd}$.

$$F_{xd,yd} = \tan(\phi_{errx,erry}) \cdot F_{xv,yv} \tag{3.17}$$

By replacing Equation 3.8 in the oscillation frequency expressions, and neglecting the higher order error terms which include the multiplication of different error sources, we can get the following expressions.

$$\begin{aligned}\omega_x = &\left(\alpha_z \frac{\dot{y}_a}{\dot{x}_a}\Omega - \frac{b_{yy}}{2m}\lambda_{xy} + \frac{y_a}{2m\dot{x}_a}k_{xy}\tan(\phi_{errx}) + \frac{\dot{y}_a}{2m\dot{x}_a}b_{xy}\right)\sin(\phi_{xy}) \\ &+ \left(-\frac{F_{yd}}{2m\dot{x}_a}\lambda_{xy} + \frac{\dot{y}_a}{2m\omega_{ox}\dot{x}_a}k_{xy}\right)\cos(\phi_{xy}) \\ &+ \frac{\xi_x}{2m\omega_{ox}}k_{tune} + \omega_{ox} - \frac{b_{xx}}{2m}\tan(\phi_{errx}) - \frac{k_{yx}}{4m\omega_{ox}}\lambda_{xy}\end{aligned} \tag{3.18a}$$

$$\begin{aligned}\omega_y = &\left(\alpha_z \frac{\dot{x}_a}{\dot{y}_a}\Omega + \frac{b_{xx}}{2m}\lambda_{yx} - \frac{x_a}{2m\dot{y}_a}k_{yx}\tan(\phi_{erry}) - \frac{\dot{x}_a}{2m\dot{y}_a}b_{yx}\right)\sin(\phi_{xy}) \\ &+ \left(-\frac{F_{xd}}{2m\dot{y}_a}\lambda_{yx} + \frac{\dot{x}_a}{2m\omega_{oy}\dot{y}_a}k_{yx}\right)\cos(\phi_{xy}) \\ &- \frac{\xi_y}{2m\omega_{oy}}k_{tune} + \omega_{oy} - \frac{b_{yy}}{2m}\tan(\phi_{erry}) - \frac{k_{xy}}{4m\omega_{oy}}\lambda_{yx}\end{aligned} \tag{3.18b}$$

The above expressions show that the quadrature signal can leak to the output due to both phase error and cross-axis stiffness mismatch. The latter mismatch leaks to the output with the common-mode phase error (ϕ_{err}). For equal velocities (symmetric FM), the overall error is written below.

$$\Omega_{err} = \frac{1}{\alpha_z}\left(\lambda_{xy}\frac{\Delta b}{2m} + \Delta\lambda_{xy}\frac{b}{2m} + \frac{\Delta b_{xy}}{2m} + \phi_{err}\frac{\Delta k_{xy}}{2m} + \Delta\phi_{err}\frac{k_{xy}}{2m}\right) \tag{3.19}$$

where, $\Delta\lambda_{xy}$, Δb_{xy}, and Δk_{xy} are the mismatch in the cross-axis terms. $\Delta\phi_{err}$ is the phase mismatch between the channels, and b, b_{xy}, and k_{xy} are common-mode terms for the damping, cross-axis damping, and cross-axis stiffness terms.

3.5 Conclusion

The gyroscope is a 2-DOF resonator. Conventionally, one of the channels is used as an oscillator, and the second channel is used as a sense mode. Here it is shown that both channels can be used as oscillators to sense angular rate. In this case, the rate is coupled to the sustaining forces and oscillation frequencies. If the system is well-balanced with equal oscillation velocities, cross-axis terms and errors cancel without the necessity of additional calibration. The scale factor when sensing frequency is also very insensitive to the velocity mismatch. For active tuning, it is important to control the oscillation frequencies in a balanced way to maintain this reciprocal summation feature and error cancellation.

In practice, unequal cross-axis terms can potentially cause large errors even with equal velocities. This problem can be minimized by using a symmetric transducer design and packaging.

Chapter 4

Indexing FM Gyroscope

FM gyroscopes have unique features allowing robust scale factor and bias stability. In addition, symmetry is very important to exploit all the features of FM gyroscope. However, perfectly symmetric transducers have very low mode-split which makes it difficult to operate FM gyroscope as free-running oscillators due to injection locking.

This chapter introduces indexed FM operation (IFM) which is ideal for highly symmetric devices. In this operating mode the x- and y-modes of a z-axis gyroscope are operated with a phase shift that alternates between +90° and -90°, corresponding to circular clock and anti clockwise orbits. Taking the difference between the rate measured in the two states rejects long-term variation of the transducer resonant frequencies. Additionally, the symmetry of the sensor and controller suppresses damping related errors.

4.1 IFM Operation

The mathematical description of the FM gyroscope has been discussed in Chapter 3. Before discussing IFM details, it is important to address why we need indexing.

In FM gyroscopes both modes are driven with equal amplitude at their respective frequencies and rate is inferred from a change in the free-running oscillation frequency. In quadrature FM (QFM) operation, a controller uses an appropriate tuning mechanism to adjust the phase difference between the x- and y-modes to a constant +90° or -90° [23]. In the presence of a rotation signal, the proof mass retains its angular momentum in the inertial frame resulting in a change of the oscillation frequency.

For an ideal Foucault pendulum, a rotation of 360°/s results in a 1Hz frequency shift in the oscillation frequency, corresponding to a unity SF. In practical transducers the scale factor is reduced by the angular gain α_z, which is set by geometry and exhibits very low sensitivity to environmental parameters, typically at the sub-ppm level, translating into excellent SF stability [14].

By contrast, the zero-rate output is set by the nominal resonant frequency which has a large temperature coefficient (approximately -30ppm/°C for Silicon). Alternating the orbit between clock and counter-clock wise oscillations as shown in Figure 4.1 up-converts the rate signal to the modulation frequency where it can be separated from long-term drift phenomena by electronic filtering.

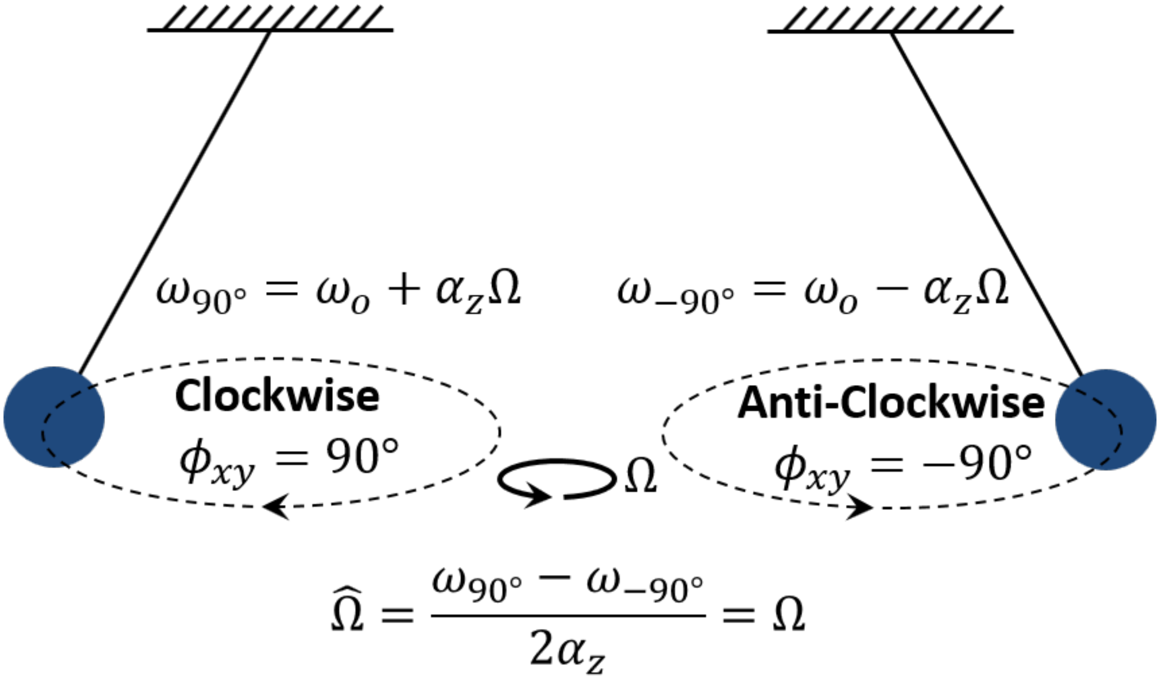

Figure 4.1. FM gyroscope with phase indexing.

4.1.1 Comparison of AM and FM Gyroscope Errors

Table 4.1 compares the outputs from conventional AM and FM gyroscopes. The quadrature error is omitted for brevity and cross-axis damping terms are assumed to be equal. Equations 4.1 and 4.3 for QFM and IFM operation differ primarily by the suppression of the resonant frequency ω in the latter.

The SF of the AM gyroscope is a complex function of several design parameters including proof mass velocity and transduction gain η. By contrast, the SF of FM gyroscopes equals the angular gain α_z modified by a term with the normalized velocity mismatch squared $(\Delta v/v)^2$ where $v = 1/2\,(\dot{x}_a + \dot{y}_a)$ and $\Delta v = (\dot{x}_a - \dot{y}_a)$.

For 1ppm SF stability the velocities (and hence amplitudes) must exhibit less than 0.14% variation, a relatively modest requirement. By contrast, to meet the same requirement with an AM gyroscope, each parameter contributing to its SF must be controlled to a fraction of 1ppm absolute accuracy, a requirement that is nearly impossible to meet with practical implementations.

Table 4.1. Gyroscope error analysis for (4.1) force-rebalance AM (voltage readout), (4.2) QFM, and (4.3) IFM operation.

$\hat{V}_y = \underbrace{\frac{2m\alpha_z\dot{x}}{\eta}}_{\text{scale factor}} \left\{ \Omega + \underbrace{\frac{b_{xy}}{2m\alpha_z}}_{\text{bias}} \right\}$	(4.1)
$\omega_{\pm 90^\circ} = \pm\alpha_z \left\{ 1 + \frac{1}{2}\left(\frac{\Delta v}{v}\right)^2 \right\} \left\{ \Omega + \frac{\Delta v}{v}\frac{b_{xy}}{2m\alpha_z} \right\} + \omega_o$	(4.2)
$\frac{\omega_{\pm 90^\circ}}{2} = \underbrace{\pm\alpha_z \left\{ 1 + \frac{1}{2}\left(\frac{\Delta v}{v}\right)^2 \right\}}_{\text{scale factor}} \left\{ \Omega + \underbrace{\frac{\Delta v}{v}\frac{b_{xy}}{2m\alpha_z}}_{\text{bias}} \right\}$	(4.3)

Similarly, the bias from aniso-damping is attenuated by the same factor Δv, translating into an at least two orders-of-magnitude advantage of FM over conventional AM operation. The quadrature error is removed with synchronous demodulation. The symmetrical design of the FM readout facilitates more accurate phase matching compared to AM gyroscopes [6], translating into reduced quadrature leakage.

Mode reversal has been proposed in AM gyroscopes as a means to reduce long-term drift [35]. In this operating mode, the roles of the drive and sense axes are periodically interchanged. Unfortunately, this solution is difficult to realize especially with the high-Q transducers generally required for high performance, limiting the reversal rate to a fraction of the transducer bandwidth.

IFM operation avoids this trade-off between resonator Q and modulation frequency. Since indexing only changes the relative phase of the x- and y-mode oscillations but does not alter the amplitude and hence energy in each mode, the modulation rate is set by the frequency tuning range Δf which is independent of the resonator bandwidth. The indexing transient in this case is the time required to change the relative phase between +90° and -90° and equals $1/(2\Delta f)$ plus the settling time of the phase control loop which in practice equals a few oscillation periods.

4.2 Experimental Characterization

The AM and FM performances were compared using the commercial gyroscope transducer [34] which is also used for the testing the background calibration methods in Chapter 2 (Figure 2.8). The device was tested in the facilities of United States Air

Force 746th Test Squadron.

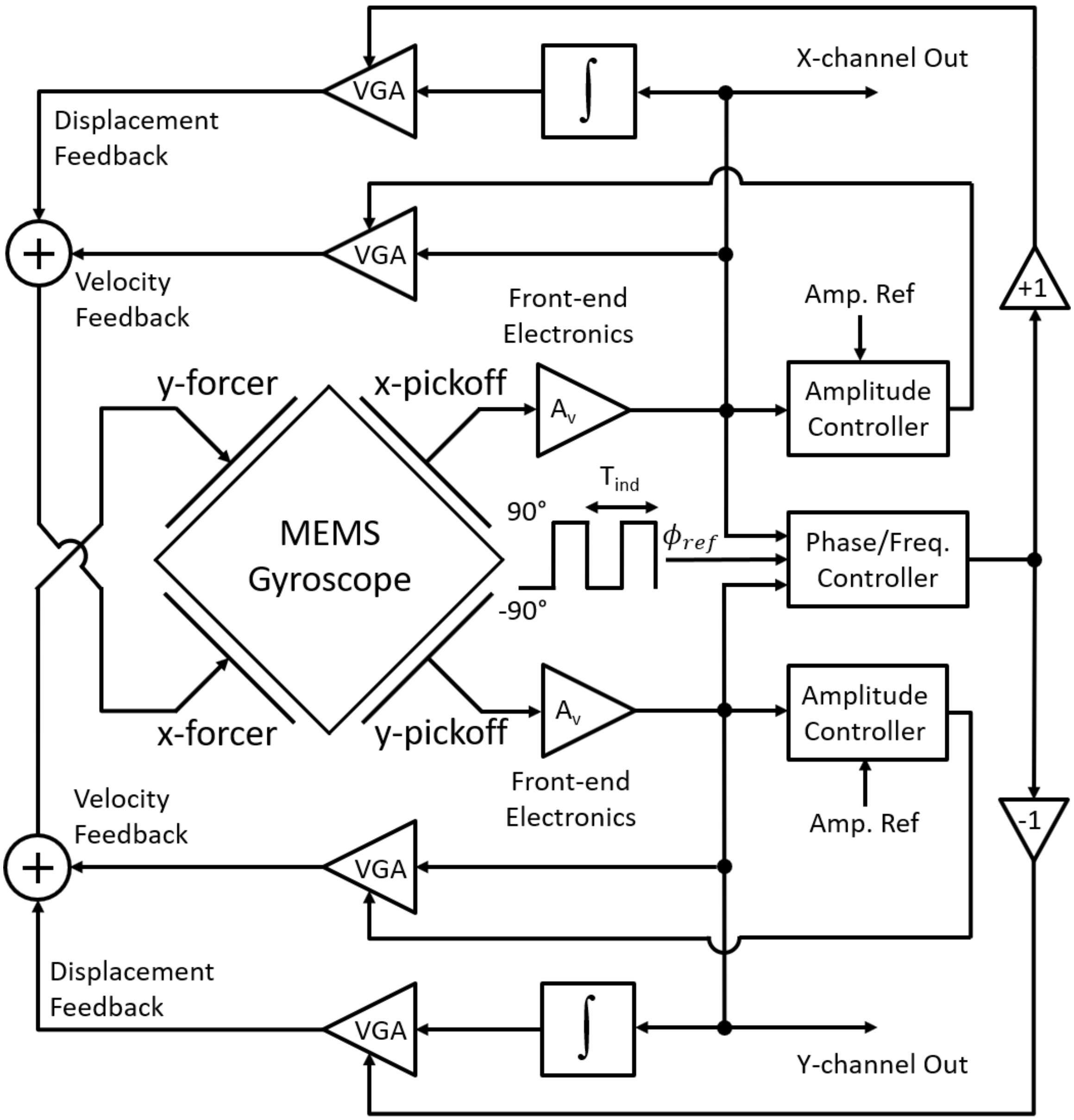

Figure 4.2. Block diagram of IFM gyroscope.

Figure 4.2 shows the block diagram. The tested device uses magnetic transduction and lacks a means to tune the mechanical resonant frequencies. Phase shifts instead are generated by the controller with forces that are in-phase with displacement. The ratio of these forces to the oscillation amplitude mimics a spring constant and can thus be used to tune the oscillators. Due to limitations of the maximum tuning force that can be realized by this method, the tuning range Δf is limited to

1 Hz. In order to attain the reciprocal summation feature, as discussed in Chapter 3, differential tuning is applied: equal magnitude with opposite polarities.

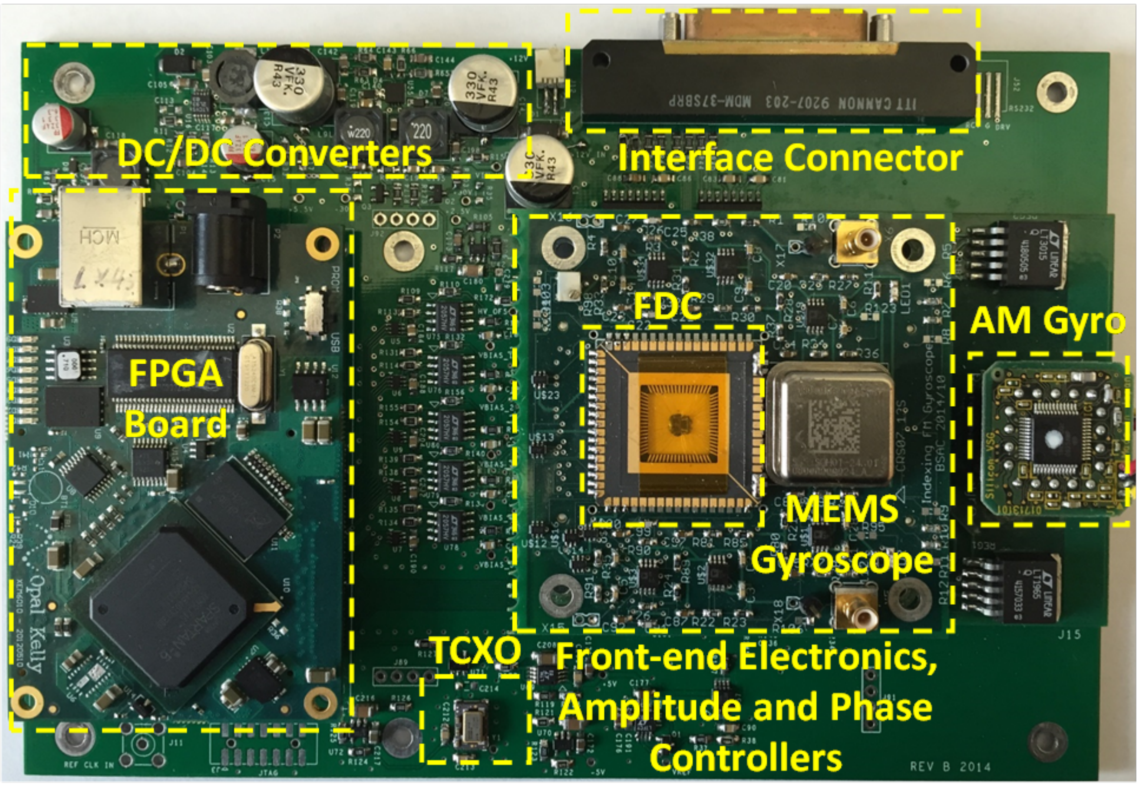

Figure 4.3. Board photo of the tested system.

Figure 4.3 shows the board photo of the tested system. The front-end electronics and controllers are implemented with discrete components, while a custom frequency-to-digital converter ASIC is used to measure the IFM frequency [36]. A 10MHz temperature compensated crystal oscillator (TCXO) with a frequency stability of 0.1ppm between 0°C to 70°C [37] supplies the reference to the frequency-to-digital converter (FDC), ensuring good scale factor accuracy.

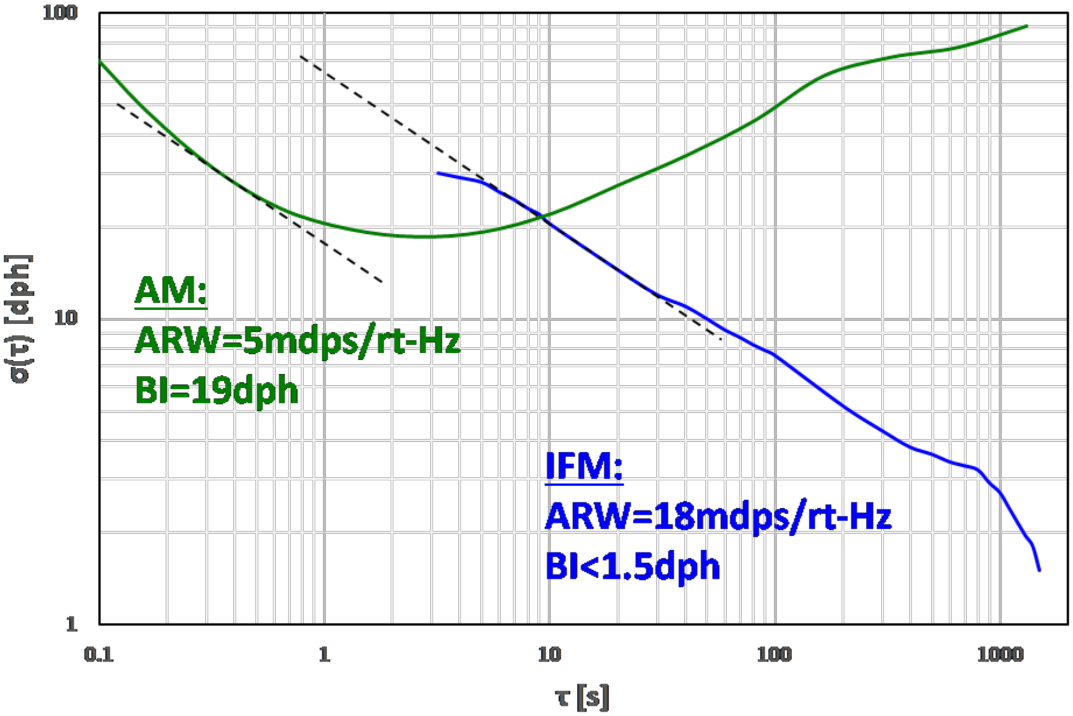

Figure 4.4. Allan variance plots for AM and IFM.

Figure 4.4 shows the in-run Allan-Variance for the AM and FM operation modes. Compared to AM operation, FM operation reduces the bias as expected, but indexing results in elevated ARW. This is caused by rate noise above the 0.8Hz indexing rate folding into the signal-band. A transducer with higher tuning range or a combination of two or more sensors can be used to eliminate this penalty.

Figure 4.5 and 4.6 show the measured bias and SF error over a 30-day period during which power was switched off between measurements. Both results demonstrate a more than two orders-of-magnitude improvement of FM over AM operation for the same transducer. For FM operation, the bias repeatability is 2.86mdps (10.3dph) and the SF repeatability is 4.3ppm. It is important to note that repeatability tests are typically more challenging than in-run stability tests. Especially for SF, ppm level repeatability is very difficult to get with the available MEMS and fiber-optic-gyroscopes (FOG) in the market without any sophisticated calibration.

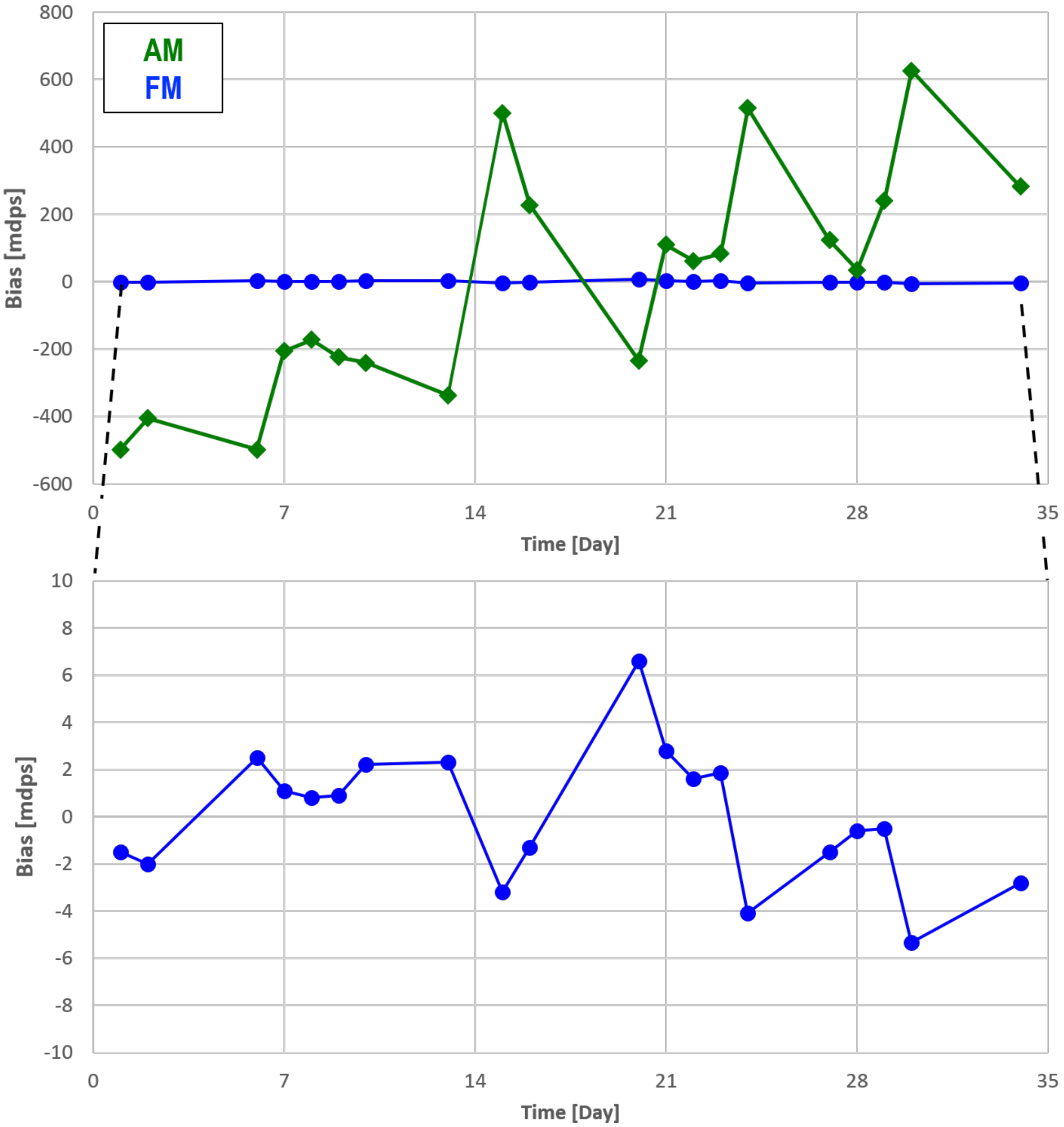

Figure 4.5. 1-month turn on bias repeatability results.

For SF measurements the FM gyroscope was tested up to ±600dps, which is the maximum rate of the rate table. FM gyroscopes inherently have a much higher full-scale range. In the system used for IFM operation, the full-scale range is limited by the current FDC, which can measure ±1000dps. This value can easily be increased thanks to the high range nature of frequency measurement.

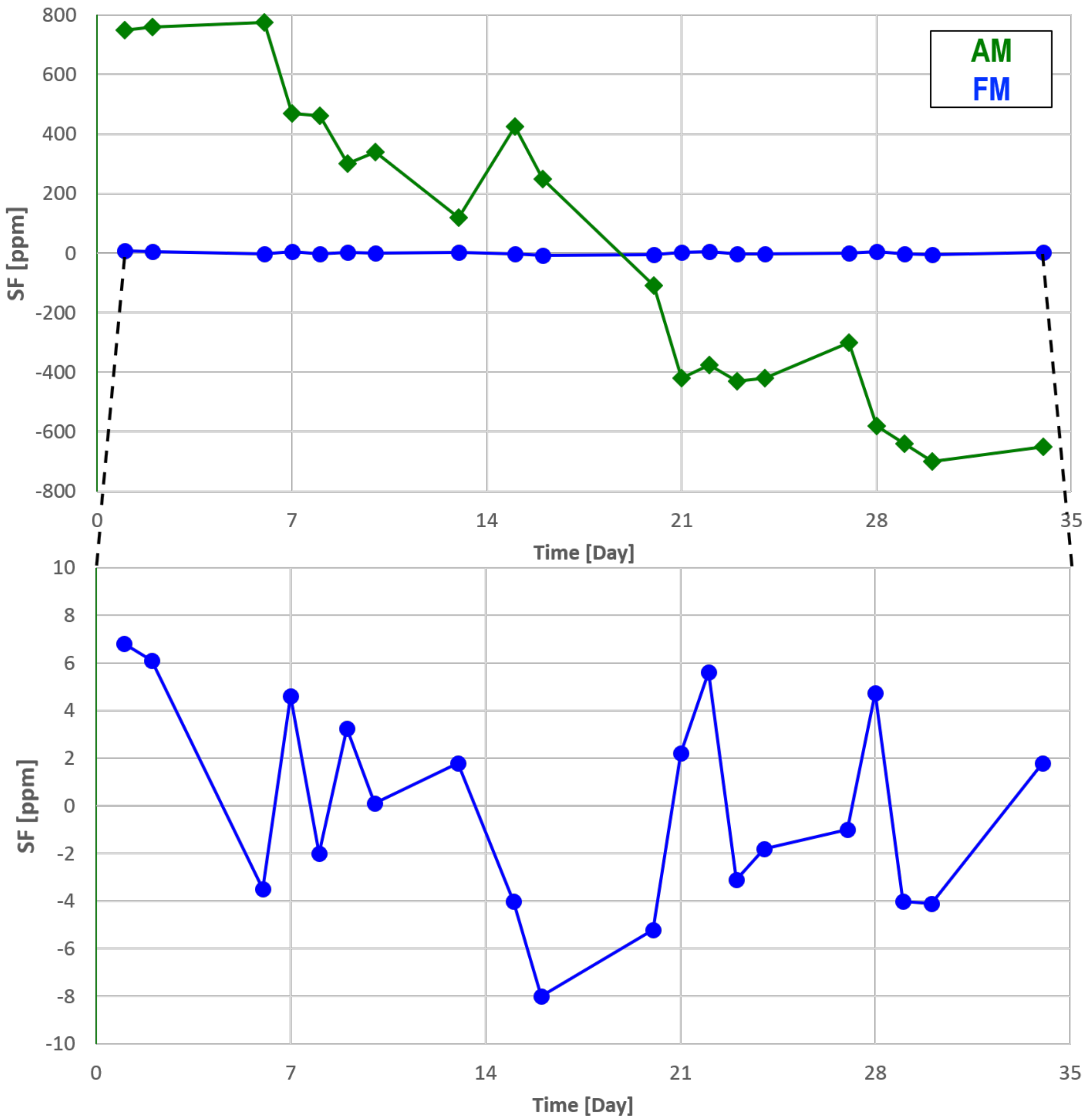

Figure 4.6. 1-month turn on SF repeatability results.

The temperature sensitivity is lowered by a similar factor, as demonstrated by the measurement results shown in Figure 4.7 and 4.8. The temperature coefficient (TC) of the SF in FM operating mode is as 1.25ppm/°C. This value is close to the TC of the angular gain of HRGs, which is reported in [14] as 0.5ppm/°C. These results show that FM gyroscopes achieve similar long-term SF stability without sophisticated calibration or trimming and are thus promising candidates for low-cost high performance gyroscopes.

Table 4.2 summarizes the results, indicating the performance advantage of FM versus AM operation.

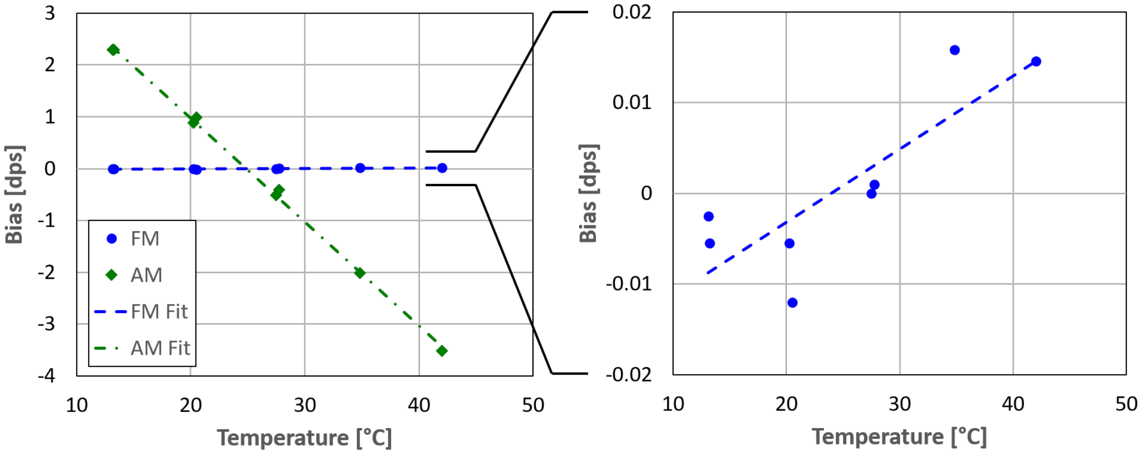

Figure 4.7. Temperature sensitivity of bias.

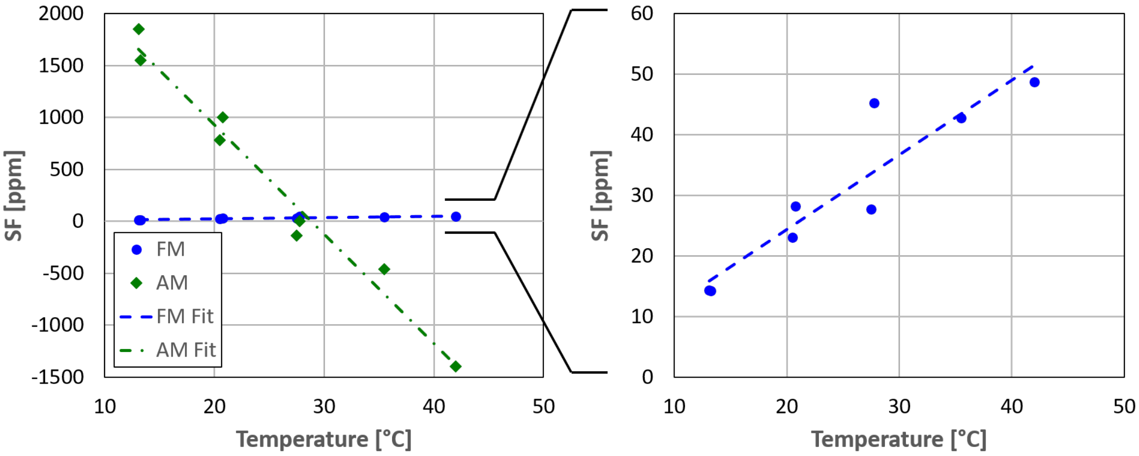

Figure 4.8. Temperature sensitivity of SF.

Table 4.2. Performance summary.

	AM	**FM**	**Improvement**
Bias (1σ)	335mdps	2.86mdps	117x
SF (1σ)	518ppm	4.31ppm	120x
TC Bias	711dph/°C	2.9dph/°C	245x
TC SF	105ppm/°C	1.25ppm/°C	84x
In-run Bias	19dph	<1.5dph	13x

4.3 Conclusion

Conventional AM gyroscopes measure rate indirectly via the amplitude of vibration of the sense channel. As a consequence, the scale factor depends on several fabrication parameters including the transduction gain and the absolute velocity of the drive axis (Chapter 2). Each of these parameters must be controlled to a fraction of the desired scale-factor accuracy, a significant barrier to achieving better than 100ppm stability. In contrast, FM gyroscopes detect rate in the form of a frequency change which can be measured with high accuracy using a crystal or other accurate clock as reference, readily enabling sub 10ppm accuracy without trimming or calibration.

Indexed FM gyroscopes benefit from a similar reduction of zero-rate output. The modulation of the rate by alternating the orbit between clockwise and anticlockwise directions eliminates the large offset in circular FM gyroscopes. As demonstrated, indexing FM gyroscopes have very impressive scale factor and bias repeatability with symmetric devices having very low mode split.

Chapter 5

Circuit Implementation

The FM gyroscope measures rate directly as frequency and converts it to a digital output by comparing it to a precision clock reference [24]. Hence, the circuit design will differ significantly from that used in conventional AM gyroscopes.

This chapter discusses the circuit implementation of FM gyroscopes. It also introduces two new techniques: (1) asymmetric FM to reduce short-term noise and (2) a bandwidth extension technique using FM and AM outputs from the same gyroscope simultaneously.

5.1 System Overview

IFM operation has been discussed in Chapter 4 for highly symmetric transducers without mode-split tuning capability. In this chapter, the transducer is a custom design based on quad-mass gyroscope topology which has a larger frequency tuning range [24]. The two channels of these transducers can operate as coupled oscillators without any injection locking problem after tuning the mode-split (Δf) to a desired value.

Figure 5.1 illustrates the principle of this operation. The transducer proof mass consists of two orthogonal resonators excited at their resonant frequencies f_o by two sustaining circuits. For a 90° phase shift in the displacements of the x- and y-channels, the motion of the proof mass follows a circular pattern. An observer in the rotating frame perceives a rate input as a shift of the observed oscillation frequency of the proof mass. The scale factor equals α_z, where α_z is the unit-less transducer gain. It can be measured accurately with a frequency-to-digital converter with an explicit reference input f_{ref}.

The transducer resonance f_o appears as a huge offset in the output. Environmental variations preclude straightforward subtraction from the rate output. Instead, the direction of the circular path is altered periodically to modulate the sign of the rate sensitivity, shifting the rate to the modulation frequency. It is accomplished by

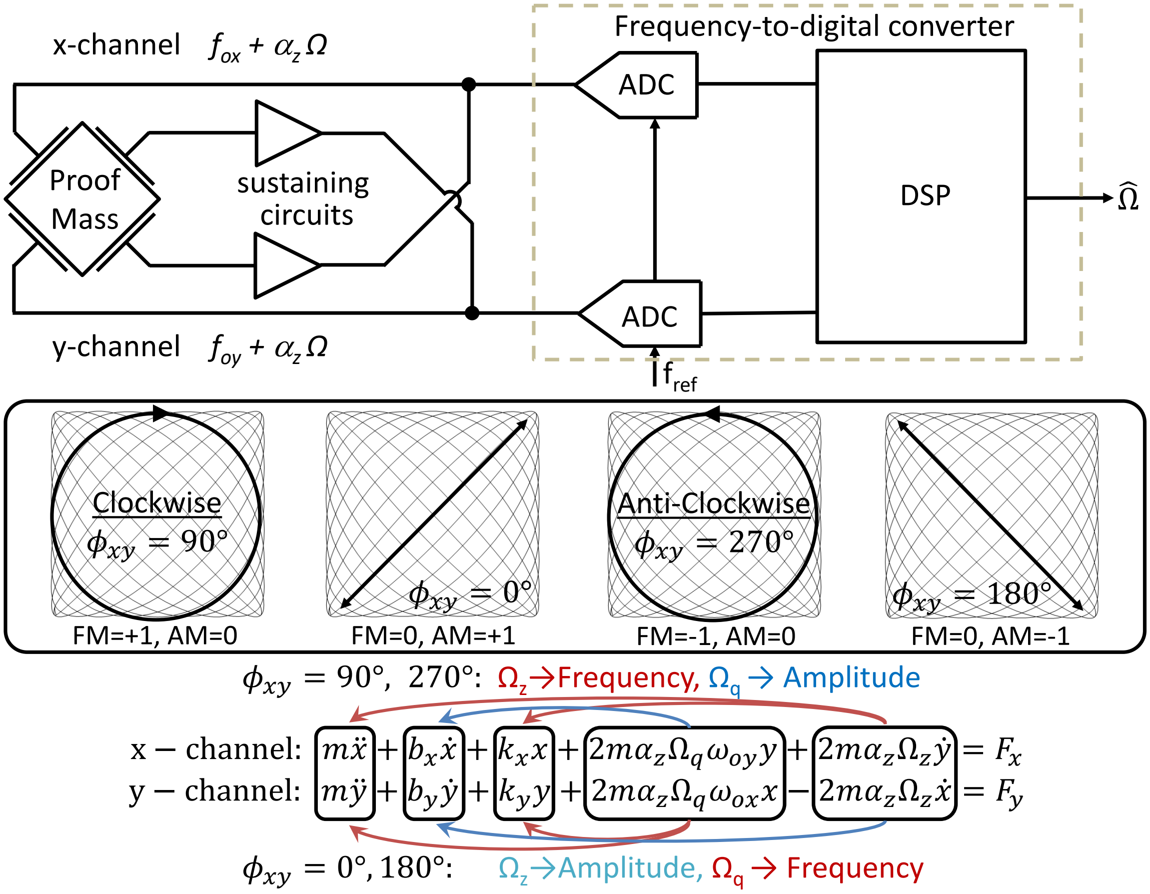

Figure 5.1. Simplified block diagram and rate chopping for FM and AM channels.

deliberately mismatching the resonances f_{ox} and f_{oy} of the two axes by a small amount Δf (typically $<$100Hz). Now the relative phase ϕ_{xy} of the x- and y-channels changes continuously, passing through 90° and 270°, corresponding to FM gains +1 and -1. This is equivalent to chopper stabilization and rejects drift at frequencies below the modulation rate. At 0° and 180° the rate modulates the amplitude rather than frequency of the x- and y-displacements. The force-equations illustrate the periodic modulation of the rate signal Ω_z and quadrature error Ω_q to frequency and amplitude, respectively. Consequently, rate appears in the output both as a frequency shift (FM channel) and modulation of the oscillation amplitude (AM channel). FM and AM signals are modulated at Δf with $\sin(\Delta\phi_{xy})$ and $\cos(\Delta\phi_{xy})$, respectively. Due to the trajectory of the proof mass, this operating mode is called *Lissajous FM* (LFM).

5.2 Implementation

As in conventional AM gyroscopes, reducing the split Δf between the modes improves the ARW of the sensor [17, 15]. Since both modes are continuously driven, Δf is observable and electrostatically tuned to 10Hz in the prototype. The ability to accurately set the split frequency is an important advantage of FM over AM implementations and a consequence of both axes being driven. Figure 5.2 shows the readout circuits consisting of a differential oscillator with amplitude control. It consists of a trans-capacitance amplifier followed by a phase shifter, amplitude detector, and VGA. The input-referred current noise of the trans-capacitance amplifier is 17fA/rt-Hz. This is the dominant noise source coming from the electronics and it corresponds to an ARW of 0.9mdps/rt-Hz at 10Hz mode split for 100nA motional current. A telescopic cascode OTA has been used at the front-end with a bias current of 20μA. The same OTA is also used in the differentiator with a bias current of 5μA. In the front-end, an active biasing circuit with long-channel transistors simulating large resistor is used to minimize noise. An SC peak detector is clocked at the zero crossings of the differentiator output to sample the oscillation amplitude. Unlike other options, this solution does not require a low-pass filter which would limit the measurement bandwidth. The VGA ensures a stable oscillation amplitude and rejects the amplitude variations from the AM channel. The active biasing, amplitude controller loop, and VGA blocks are discussed in the sections below.

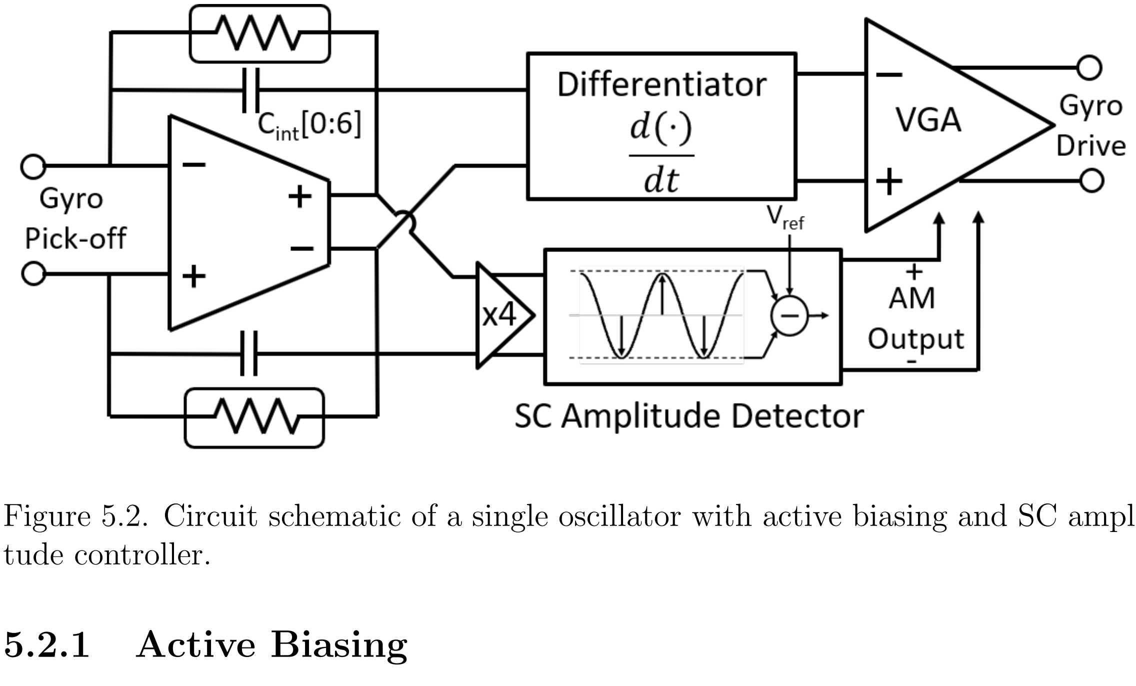

Figure 5.2. Circuit schematic of a single oscillator with active biasing and SC amplitude controller.

5.2.1 Active Biasing

In the oscillator design, the TIA is the main block determining the noise performance. In order to have accurate gain and avoid the resistor noise, a capacitive TIA is used. In order to provide the DC feedback to keep the TIA OTA in the linear region, a resistor is used in the feedback parallel to the capacitance. This resistor should be large enough to ensure (1) the signal flows through the capacitor with a minimum phase error and (2) the current noise of the resistor does not degrade the noise performance. In order to keep the resistor noise negligible compared to the main noise sources such as Brownian and front-end OTA noises, the resistor needs to be larger than 1GΩ. It is not feasible to directly implement such a large resistor in CMOS due to its exorbitant area requirement and parasitic capacitance.

It is possible to implement such a large resistor using a pseudo resistor [38]. However, such an implementation is very sensitive to threshold variations. An uncontrolled large resistance in the feedback path can cause significant offset at the output due to potential leakage coming from the transducer. Additionally, these large resistors cause excess voltage noise at the pick-off electrodes, which may degrade the noise overall noise performance, especially when considering the electrode non-linearity (due to electrostatic spring softening from the electrode bias).

Duty-cycled resistors can be used to implement large resistor values in a controllable way [39], but the discontinuous operation can potentially increase the oscillator phase noise.

DC feedback through an active circuit can be used to replicate the function of the biasing resistor. The easiest solution is to use a buffer with a small transconductance for low noise. The following section discusses the small-signal behavior of active biasing circuit.

5.2.1.1 Small-signal Behavior

Figure 5.3a shows the conceptual circuit diagram with an ideal amplifier in the feed-forward path. The frequency dependent feedback-factor (F) in this amplifier is

$$F = \frac{g_m^* + sC_{int}}{s\left(C_{in} + C_{int}\right) + g_m^*} \tag{5.1}$$

The phase error and normalized magnitude error at the oscillation frequency ω in the loop is approximated as

$$\theta_{err} = \left|\frac{A_{err}}{A}\right| \approx \frac{g_m^*}{\omega C_{int}} \tag{5.2}$$

In order to decrease the current noise of active biasing circuit, g_m^* should be minimized. This forces the transistors to operate in the sub-threshold region. However, the output of the front-end has high swing which causes non-linearity and noise folding in the feedback path. In order to alleviate this problem, a low-pass filter with a cut-off frequency ω_{lpf} is used as shown in Figure 5.3b. In this case, the feedback factor is

$$F = \frac{g_m^*(1 + s/\omega_{lp})^{-1} + sC_{int}}{s\left(C_{in} + C_{int}\right) + g_m^*} \tag{5.3}$$

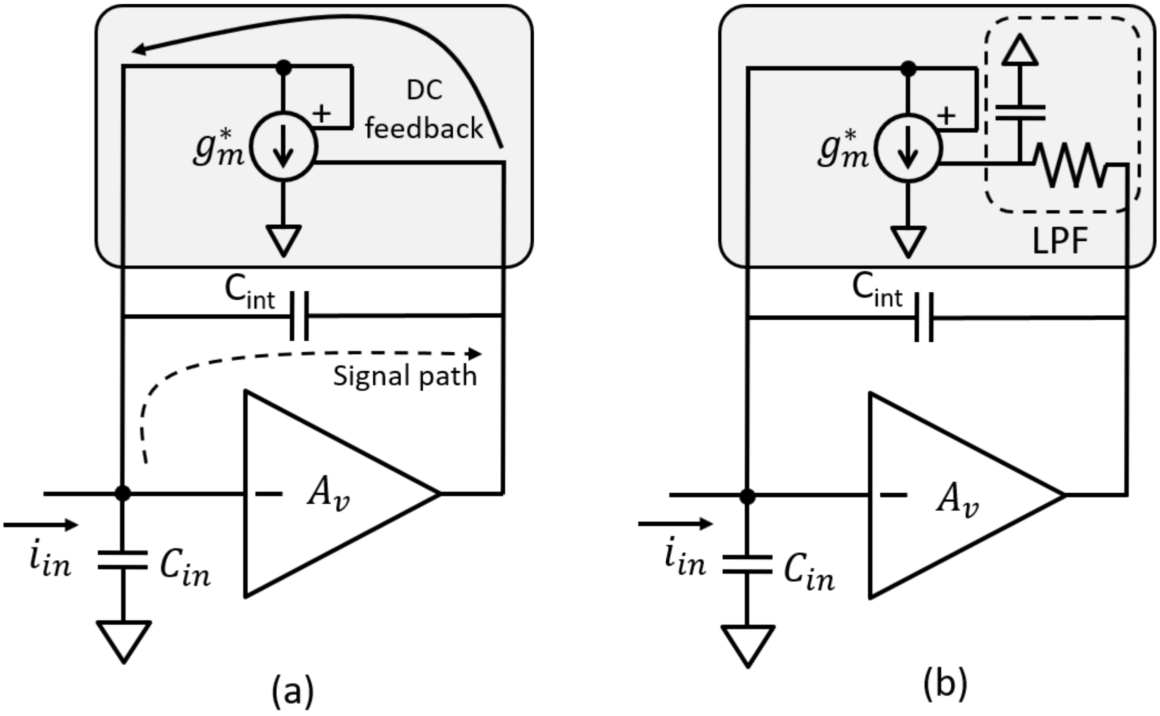

Figure 5.3. Conceptual diagram of active biasing.

Having additional low-pass filter also delays the signal in the feedback path by roughly 90°. This decreases the phase error by $(\omega/\omega_p)^2$. The magnitude error is same as without the low-pass filter.

$$\theta_{err} \approx \frac{g_m^*}{C_{int}} \frac{\omega_{lp}^2}{\omega^3} \tag{5.4}$$

This extra suppression of the phase-error is very useful for applications where the phase error in the TIA is important. This is especially important for conventional AM gyroscopes where quadrature leakage heavily depends on the phase delay in the front-end of the drive mode.

Here, the frequency response of the biasing OTA is ignored. If the conventional single-ended OTA is used, it has one pole and one zero at ω_p and $2\omega_p$, respectively. The pole ω_p is at g_{mp}/C_x, where C_x is dominated by the gate capacitance at the mirror node. The transistors have long-channel lengths to prevent the transistors from entering deep sub-threshold due to their low bias currents. As a result, g_{mp} is low and C_x is high which set the ω_p to low frequencies. In this case, it is important to include the effect of ω_p.

$$F = \frac{G_m^*(1+s/\omega_{lp})^{-1} + sC_{int}}{s\left(C_{in}+C_{int}\right)+G_m^*} \tag{5.5}$$

where $G_m^* = g_m^* \cdot \dfrac{1+s/(2\omega_p)}{1+s/\omega_p}$. For the frequency of interest, the current flowing through the mirror node has a negligible effect assuming, $\omega_p \ll \omega$. The new phase and gain error expressions are

$$\theta_{err} \approx \frac{g_m^*}{2C_{int}} \frac{(\omega_{lp} - \omega_p)\,\omega_{lp}}{\omega^3} \tag{5.6}$$

This is almost the same expression for $\omega_p \ll \omega$. The phase error can further be minimized by matching ω_p to ω_{lp}. In this case, the gain error is half of the previous gain errors, since at higher frequencies the effective trans-conductance is half-of the DC trans-conductance (g_m^*).

5.2.1.2 Noise of Active Biasing Circuit

The input-referred current noise contribution to the TIA due to the active biasing is simply the short-circuit current noise of the biasing OTA: $i_n = 4kTg_m^*\gamma NF$.

Due to the sub-threshold operation, noise-folding of the tail-current noise degrades the noise. Adding the filter before the biasing OTA avoids such a limitation. Figure 5.4 shows the input referred current noise obtained with PNOISE simulation for 400mV$_{pp}$ voltage swing at the TIA output with and without the low-pass filter with a cutoff frequency of 3kHz. The dashed line shows the noise level for the equivalent 2GΩ resistor.

The tail-current is 50pA and 64 long-channel transistors are cascaded with a size of 220nm/20μm to keep the transistors away from the deep sub-threshold region. The V* of the input transistors is roughly 100mV. In this case, the noise power of the active biasing is less than 5% of the front-end noise power. Figure 5.5 shows the transistor-level implementation of the active-biasing circuit.

5.2.2 Amplitude Controller

Amplitude controller not only regulates the amplitude to maintain a reliable FM operation, but also determines the performance of AM channel. The base-band model of the differential equations for the oscillation amplitude can be found as follows assuming amplitude and oscillation frequencies are slowly varying terms compared to ω_o.

$$\dot{x}_a = b(t) \cdot x_a \tag{5.7}$$

The solution of this time-varying differential equation is

$$x_a(t) = x_a(t_0) \cdot e^{-\displaystyle\int_{t_0}^{t} \frac{\beta(t)}{2} dt} \tag{5.8}$$

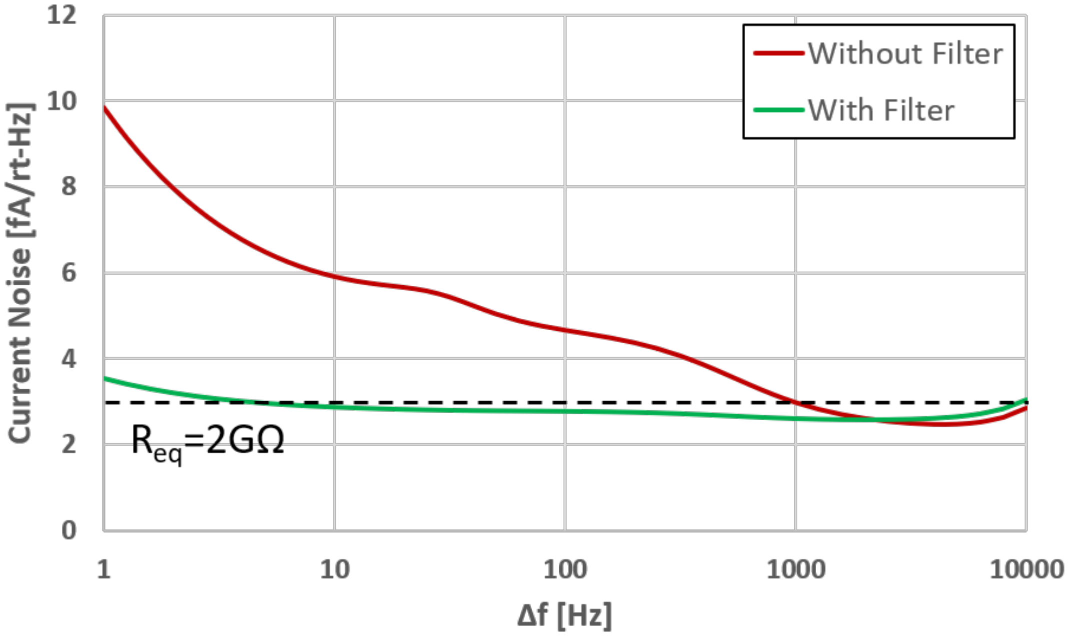

Figure 5.4. Input-referred current noise due to active biasing.

where t_0 is the initial time and $\beta(t)$ is the time-varying bandwidth of the electromechanical resonator. Note that, in a typical resonator this bandwidth is constant. However, in an oscillator loop with an amplitude control loop, this term is being controlled continuously, thus Equation 5.8 should be used to analyze the dynamics of the amplitude control loop.

After the initial transient, a reasonable controller reaches its steady state by ensuring that the argument of the exponent in (5.8) is close to 0. Under this condition, (5.8) can be further simplified using Taylor's Series expansion [40].

$$x_a(t) = x_{ao} \cdot \left(1 - \int \frac{\beta(t)}{2} dt\right) \tag{5.9}$$

where x_{ao} is the desired oscillation amplitude.

Equation 5.9 demonstrates an integral behavior. The integrator behavior can be confirmed from a functional perspective. The controller needs to set the control voltage of the electrical resistance to a certain value in order to eliminate the mechanical loss. This control voltage does not depend on the desired oscillation amplitude. In other words, changing the desired oscillation amplitude (x_{ao}) does not change the error voltage, hence it does not cause a gain error as a proportional controller does. The only static error in this scheme comes from the error voltage which sets the effective loss to 0 to sustain the oscillation.

Equation 5.9 is rewritten as

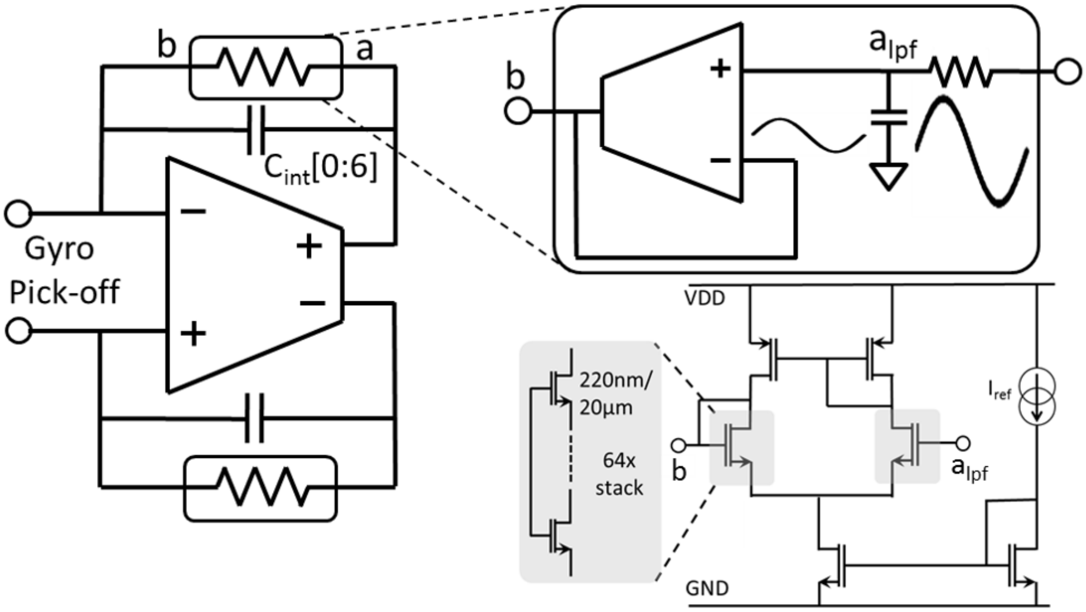

Figure 5.5. Transistor-level implementation of active biasing.

$$x_a(t) = x_{ao} \cdot \left(1 - \frac{1}{2}\int (\beta_{\text{mech}} - \beta_{\text{el}}(t))\,dt\right) \tag{5.10}$$

where β_{mech} is the mechanical bandwidth and $\beta_{\text{el}}(t)$ is the time-varying electrical bandwidth which is controlled by a control voltage (V_c) with a sensitivity of K_{el} as shown below.

$$x_a(t) = x_{ao} \cdot \left(1 - \int \left(\frac{\beta_{\text{mech}}}{2} - K_{\text{el}}V_c(t)\right) dt\right) \tag{5.11}$$

As discussed above, Equation 5.11 shows an integrator behavior which eliminates the gain error. There is only a systematic offset (V_{co}) due to the mechanical loss in the resonator.

$$V_{co} = \frac{\beta_{\text{mech}}}{2K_{el}} \tag{5.12}$$

Equation 5.11 can be further modified for voltage domain by multiplying the oscillation amplitude with the transduction gain (η) and integration capacitor (C_{int}) in TIA. The desired oscillation amplitude V_{ao} is replaced by the reference voltage V_{ref}.

$$V_a(t) = V_{ref} \cdot \left(1 - \int \left(\frac{\beta_{\text{mech}}}{2} - K_{\text{el}}V_c(t)\right) dt\right) \tag{5.13}$$

The complete amplitude behavior of the system can be analyzed using (5.11). Figure 5.6 shows the behavioral model including the transfer function of the sampler used in the amplitude detector and the first-order low pass filter used for smoothing the output waveform.

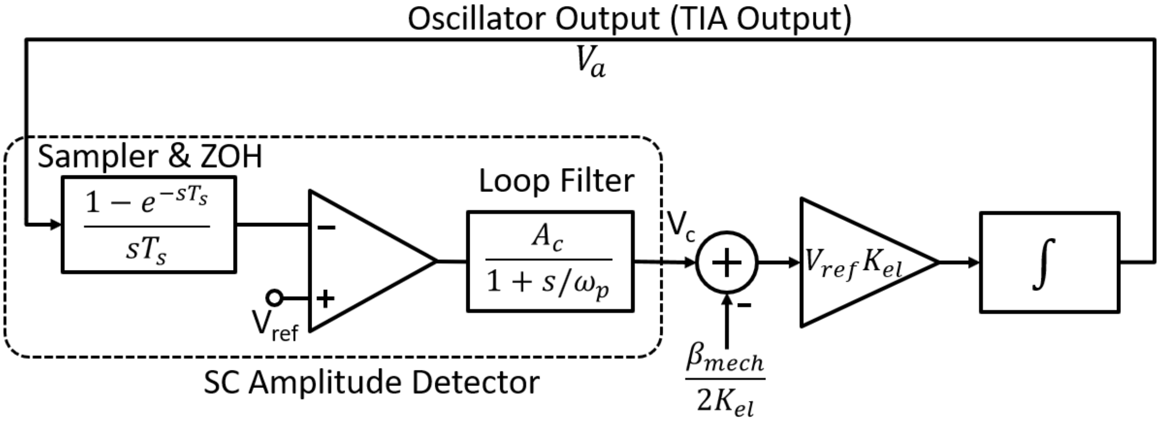

Figure 5.6. Behavioral model for amplitude-control loop.

The open-loop transfer function can now be written as follows:

$$H_{a,ol}(s) = \frac{1 - e^{-sT_s}}{s} \frac{A}{1 + s/\omega_p} \frac{1}{s} \tag{5.14}$$

where s is the base-band argument for the Laplace transform and $A = A_c V_{ref} K_{el} / T_s$. Before analyzing further, it can be noticed that the dynamics of this loop are very similar to type-I PLL dynamics [41]. In PLLs implemented with phase-frequency detectors (PFD), the phase is sampled at zero-crossings and the VCO behaves like an ideal integrator. Here, amplitudes are sampled at the peaks and the self-sustaining loop itself behaves as an integrator. Here, there is no additional loop filter as in type-II PLLs [41] to eliminate the effect of offset thanks to low mechanical loss (high-Q).

It is desirable to maximize the bandwidth to be able to reject amplitude ripple as much as possible. In addition, having larger bandwidth also increases the signal bandwidth for AM channel which potentially increases the overall bandwidth in the combined output with FM.

Since the sampling frequency is fixed in terms of the oscillation frequency, the bandwidth can be maximized by setting the electrical gains properly. Here, the low-pass cut-off ω_p needs to be low enough to avoid disturbance in the oscillators by smoothing the SC transients.

Figure 5.7 shows the closed-loop peaking and phase margin vs. 3dB closed-loop bandwidth for $\omega_p = 0.2\pi f_s$. As expected, the bandwidth can go up to 10% of the sampling frequency while maintaining a reasonable phase margin and closed-loop peaking.

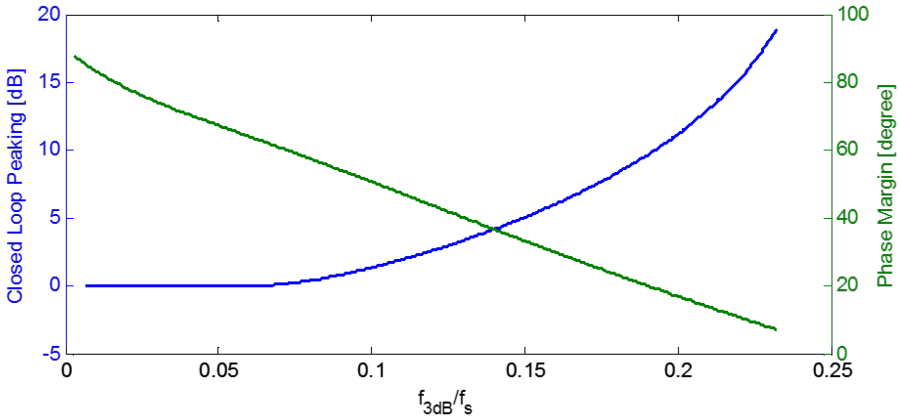

Figure 5.7. Frequency response of the amplitude-control loop.

Figure 5.8 shows the root-locus plot of the amplitude-control loop for varying gain A, shown in (5.14) for $\omega_p = 0.2\pi f_s$. The delay in the sampler (ZOH) is approximated with the Pade approximation with an order of 4. The system becomes unstable for $f_{3dB} = f_s/6$.

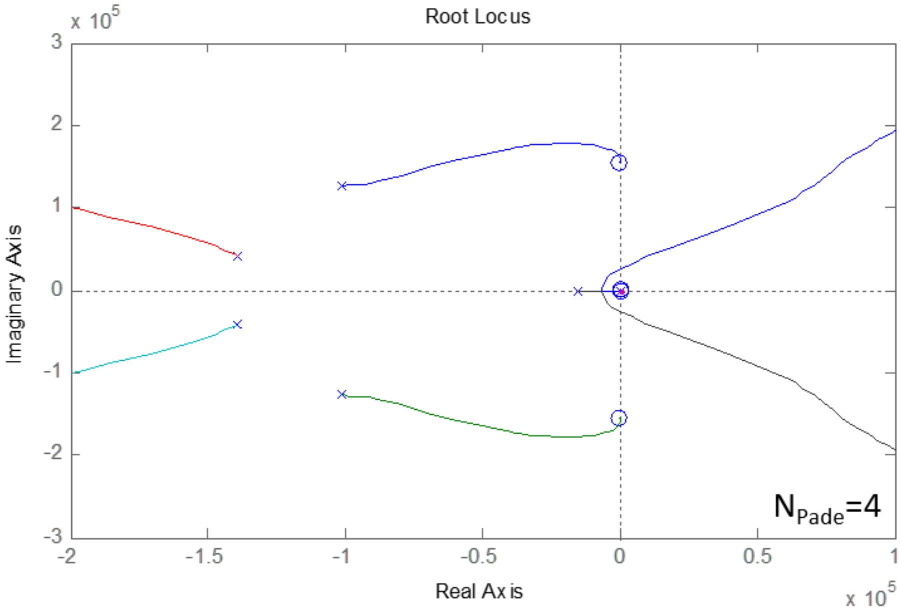

Figure 5.8. Root-locus of the amplitude-control loop.

5.2.2.1 Switched Capacitor Amplitude Detector

The most critical block in the amplitude controller block is the amplitude detector. Conventional amplitude detectors rely on rectification and filtering of 2f components [42]. This extra filter introduces additional poles in the system, limiting the bandwidth. In this work, peaks are sampled synchronously [43] with the differentiator outputs. For the synchronous sampling, a fully-differential switched capacitor amplifier is used. This block not only samples the positive and negative peaks, but also works as an error amplifier by subtracting the peak-to-peak value from the reference voltage (V_{ref}).

Figure 5.9 shows the SC amplifier with the timing of the clocks. A wrap-around topology is preferred due to its flicker and offset cancellation features [44]. The front-end TIA is isolated from transient effects of this SC amplifier by an additional amplifier. Including the buffer amplifier, the overall amplitude detector consumes 45μA per channel.

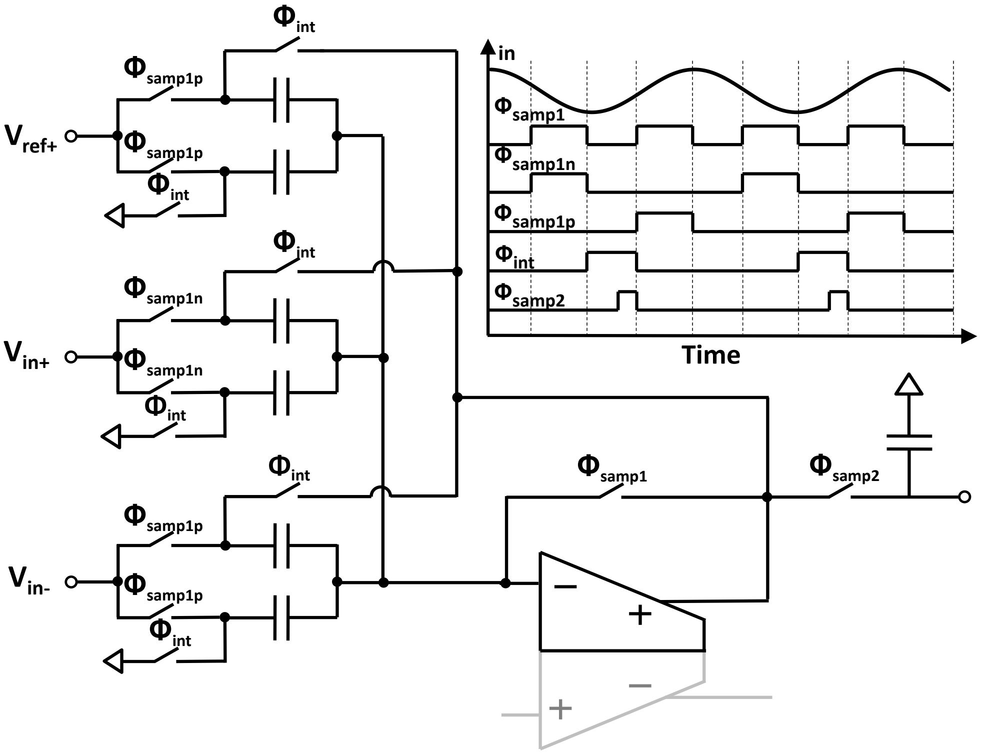

Figure 5.9. SC amplitude detector.

5.2.3 Variable Gain Amplifier

In a typical resonator, the VGA compensates the loss in the resonator. For that reason, typical VGAs used in the self-sustaining loop operate in a limited range.

These VGAs are relatively simple amplifiers such as a bias controlled common-source amplifiers used in Pierce oscillators [45].

However, in FM gyroscope VGA also needs to compensate the coupling forces such as Coriolis and quadrature forces. These forces can be much higher than the sustaining force. In this case, the VGA should be able to change its polarity to compensate these forces. To be able to change the polarity, a differential VGA is used as shown in Figure 5.10.

Voltage-controlled resistors implemented with triode-devices change the bias current and gain. A replica of the VGA controls the biasing of the bottom cascode (V_{bn1} and V_{bn2}) so that output CM does not change with the control voltages ($V_{contp,contn}$). The common-mode output is regulated by the triode transistors. Figure 5.11 shows that VGA can compensate the coupling forces even if they are larger than the sustaining forces.

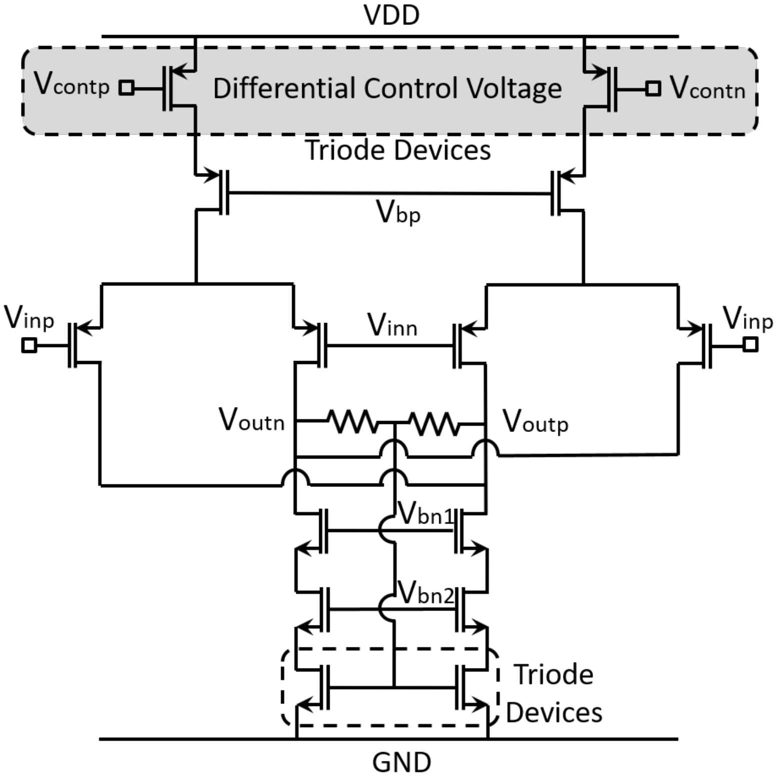

Figure 5.10. Differential VGA.

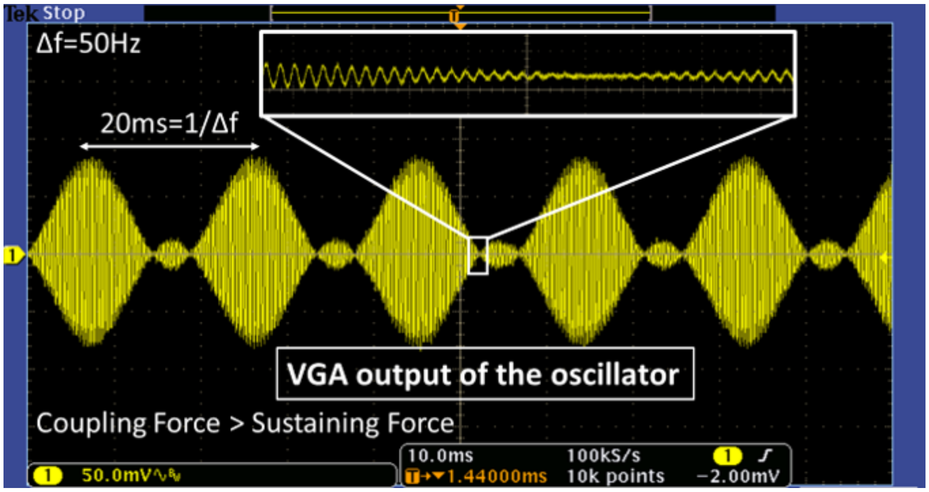

Figure 5.11. VGA output during operation.

5.3 Noise

There are three main noise sources determining the overall noise performance of FM gyroscopes: oscillator noise, ADC noise, and transducer bias noise.

5.3.1 Oscillator Noise

In the linear oscillators, base-band models can be used to estimate phase noise. A linear oscillator can be simplified to Figure 5.12 with the base-band model of the MEMS resonator, TIA with a gain of Z_{tia} and an amplifier with a gain of A_v including the gains of differentiator and VGA. The noise sources are also included for amplifiers and MEMS resonator.

Base-band impedance of the MEMS resonator is

$$Z_x = R_x + 2sL_x \tag{5.15}$$

where R_x is the motional resistance, L_x is the motional inductance, and s is the base-band Laplace argument ($j\Delta\omega$). In order to achieve the sustaining oscillations, electrical resistance seen by the resonator needs to cancel the motional resistance: $R_x = Z_{tia}A_v$. Using this condition, the noise on the motional current (i_{xo}) flowing through the oscillator is found as

$$i_{xn}^2 = \frac{v_{n1}^2 \cdot A_v^2 + v_{n2}^2 + v_{nRx}^2}{(2\Delta\omega L_x)^2} \tag{5.16}$$

and the voltage noise at the oscillator output is

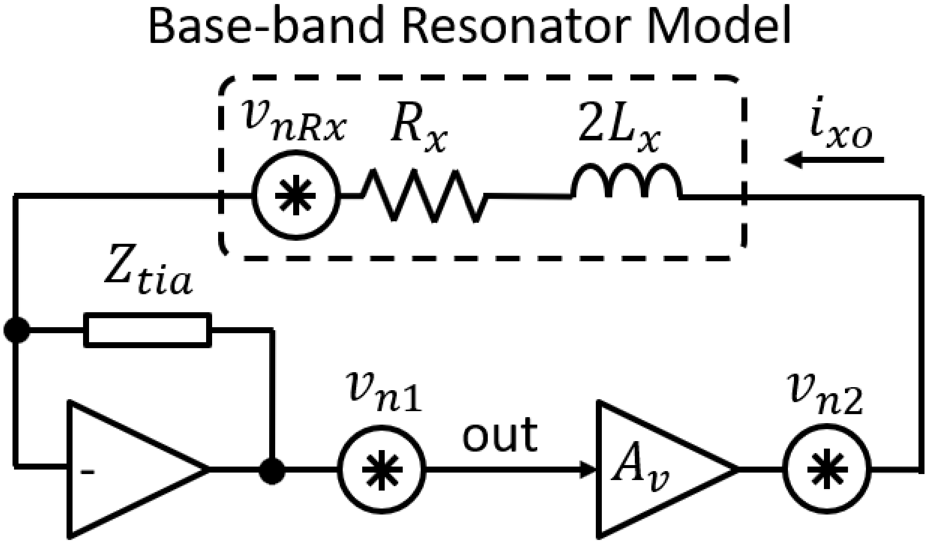

Figure 5.12. Noise model for the self-oscillation loop.

$$v_{osc,n}^2 = \frac{v_{n1}^2 \cdot A_v^2 + v_{n2}^2 + v_{nRx}^2}{(2\Delta\omega L_x)^2}|Z_{tia}^2| + v_{n1}^2 \tag{5.17}$$

Phase noise of the oscillator equals to SNR which is $\frac{v_{osc,n}}{i_{xo}|Z_{tia}|}$. Here remember that each noise source will contribute to amplitude and phase noise. Therefore, noise power should be divided by 2 for phase noise analysis. However, phase noise at a frequency offset of Δf is caused by the spot noise at frequencies of $f_o \pm \Delta f$. This is an extra 3dB noise penalty which compensates the previous 3dB drop assuming noise is white around f_o. Therefore, phase noise can simply be calculated from spot noise values of the noise sources. Using (5.17), phase noise (ϕ_n) is expressed below.

$$\phi_n^2 = \underbrace{\frac{1}{i_{xo}^2}\frac{v_{n1}^2 \cdot A_v^2 + v_{n2}^2 + v_{nRx}^2}{(2\Delta\omega L_x)^2}}_{\text{shaped by } \Delta\omega} + \underbrace{\frac{1}{i_{xo}^2}\frac{v_{n1}^2}{|Z_{tia}|^2}}_{\text{white phase noise}} \tag{5.18}$$

Here, the first term is the shaped phase noise with the offset frequency and the latter one is white. The frequency noise can simply be found by multiplying phase noise with the offset frequency which is corresponding to the mode split[1].

$$\omega_n^2 = \phi_n^2 \Delta\omega^2 \tag{5.19}$$

---

[1] Frequency is the derivative of phase and both of them are base-band terms.

$$\omega_n^2 = \underbrace{\frac{1}{i_{xo}^2}\frac{v_{n1}^2 \cdot A_v^2 + v_{n2}^2 + v_{nRx}^2}{(2L_x)^2}}_{\text{white frequency noise}} + \underbrace{\frac{1}{i_{xo}^2}\frac{v_{n1}^2}{|Z_{tia}|^2}\Delta\omega^2}_{\text{shaped frequency noise}} \tag{5.20}$$

Equation 5.20 shows that for low $\Delta\omega$ noise is white and dominated by both mechanical and electrical noise sources. However, increasing the mode split directly increases noise power after the noise corner where shaped and white noise sources are equal to each other.

Using the criteria for sustaining oscillation, A_v can be replaced by R_x/Z_{tia}. In addition, $R_x/(2L_x)$ equals to the half-mechanical bandwidth ($\beta_{mech}/2$) and $v_{n1}/|Z_{tia}|$ equals to the input referred current noise (i_{n1}). Then, (5.20) can be rewritten as follows.

$$\omega_n^2 = \frac{1}{i_{xo}^2}\frac{v_{n2}^2 + v_{nRx}^2}{(2L_x)^2} + \frac{i_{n1}^2}{i_{xo}^2}\left(\Delta\omega^2 + \left(\frac{\beta_{mech}}{2}\right)^2\right) \tag{5.21}$$

v_{n2} is the output referred noise coming from the differentiator and VGA. If transduction gain of the sensor is high, automatic gain controller will set the gain of VGA to low value. In this case, VGA output noise will dominate the white frequency noise. Note that VGA cancels the signal coming from two different path (Figure 5.10). However, noise of the input transistors does not cancel since they are uncorrelated. As expected, SNR of the driving signal degrades and white frequency noise increases. To avoid this problem, a passive attenuator can be used so that nominal VGA gain can be higher. With an attenuator gain A_{attn} frequency noise is modified to

$$\omega_n^2 = \frac{1}{i_{xo}^2}\frac{v_{n2}^2 \cdot A_{attn}^2 + v_{nRx}^2}{(2L_x)^2} + \frac{i_{n1}^2}{i_{xo}^2}\left(\Delta\omega^2 + \left(\frac{\beta_{mech}}{2}\right)^2\right) \tag{5.22}$$

But, this approach suggests the maximization of the attenuation amount. Nevertheless, increasing the attenuation amount decreases the full-scale range because of the fixed supply limit. Amplitude controller loop will not be able to re-balance the force higher than its supply limit.

The nominal motional current (i_{xo}) and the regarding actuation voltage ($i_{xo}R_x$) is corresponding to half-of the mechanical bandwidth ($\beta_{mech}/2 = R_x/(2L_x)$). Then, maximum angular rate (Ω_{max}) which can be compensated by the maximum output voltage (V_{max}) is found below.

$$\Omega_{max} = \frac{V_{max}A_{attn}}{i_{xo}R_x} \cdot \frac{R_x}{2L_x} = \frac{V_{max}A_{attn}}{i_{xo}2L_x} \tag{5.23}$$

Combining Equations 5.23 and 5.22, frequency noise can be expressed as follows.

$$\begin{aligned}\omega_n^2 &= \frac{1}{i_{xo}^2}\frac{v_{nRx}^2}{(2L_x)^2} + \frac{v_{n2}^2}{V_{max}^2}\Omega_{max}^2 + \frac{i_{n1}^2}{i_{xo}^2}\left(\Delta\omega^2 + \left(\frac{\beta_{mech}}{2}\right)^2\right) \\ &= \omega_{n,brw}^2 + \frac{v_{n2}^2}{V_{max}^2}\Omega_{max}^2 + \frac{i_{n1}^2}{i_{xo}^2}\left(\Delta\omega^2 + \left(\frac{\beta_{mech}}{2}\right)^2\right)\end{aligned} \tag{5.24}$$

where $\omega_{n,brw}$ is the Brownian noise.

Equation 5.24 tells that TIA noise increases linearly with mode-split. This behavior is same as the conventional AM gyroscopes. Furthermore, Brownian noise effect and feedback noise expressions are also similar to AM gyroscopes. In order to reach the Brownian noise performance for a targeted full-scale range, mode-split should be minimized and motional current should be maximized. Otherwise, more power should be consumed to reduce the noise. Remember that rate sensitivity of the gyroscopes is also a function of α_z and velocity ratios. Rate-referred noise can easily be found by dividing the frequency noise with the SF which is α_z for symmetric FM. The noise in dps/rt-Hz can be expressed as

$$\Omega_n[\mathrm{dps}/\sqrt{\mathrm{Hz}}] = \frac{\omega_n}{2\pi SF} \cdot 360\frac{\mathrm{dps}}{\mathrm{Hz}} \tag{5.25}$$

Also use of two outputs in the symmetric operating mode decreases the total noise by 3dB. However, sinusoidal chopping decreases the signal (rate) power which causes 3dB . Moreover, ARW is usually a common metric for noise in inertial sensors. This parameter is also $1/\sqrt{2}$ of the rate-noise density.

Figure 5.13 shows the power breakdown of the ASIC. Note that power breakdown does not include the off-chip ADCs. The dominant noise source in the ASIC is the TIA. This noise is corresponding to ARW of 0.9mdps/rt-Hz for $i_{xo} = 100\text{nA}$ at $\Delta f = 10\text{Hz}$.

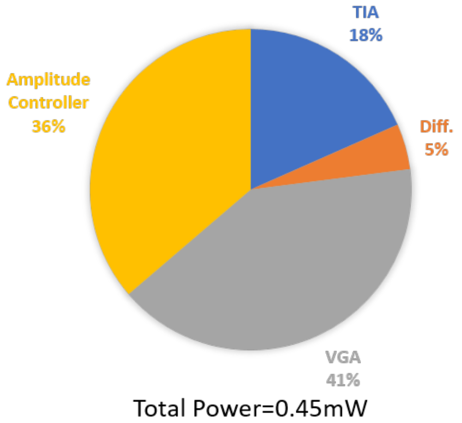

Figure 5.13. Power breakdown for the ASIC.

5.3.2 ADC Noise

Frequency measurement is done by digitizing the oscillator with ADCs. Noise of the ADC is an additive signal which will cause white phase noise ($\phi_{n,adc}$). Using the full-scale range of the ADC (V_{FS}) and the spot noise at f_o, $\phi_{n,adc}$ can be found as follows.

$$\phi_{n,adc}^2 = \frac{v_{n,ADC}(f_o)^2}{0.5\,(V_{FS}/2)^2} \tag{5.26}$$

If the ADC is wide-band with a sampling frequency of f_s, noise density in terms of SNR (in dB scale) is

$$v_{n,ADC}^2 = \frac{V_{FS}^2}{4 \cdot 10^{\frac{\text{SNR}}{10}} \cdot f_s} \tag{5.27}$$

Then, the phase noise becomes

$$\phi_{n,adc}^2 = \frac{10^{-\frac{\text{SNR}}{10}}}{0.5 f_s} \tag{5.28}$$

and the frequency noise becomes

$$\omega_{n,adc}^2 = \frac{10^{-\frac{\text{SNR}}{10}}}{0.5 f_s}\,(\Delta\omega)^2 \tag{5.29}$$

Because the spot noise at the resonance frequency determines the noise, it is better to use narrow-band ADCs. Wide-band ADCs in the market can also provide low noise with reasonable power consumption. AD7982 which has 99dB SNR consumes 0.7mW power at 100kHz sampling rate [46]. With these specifications, ARW contribution of this ADC is roughly 0.25mdps/rt-Hz at $\Delta f = 10Hz$.

5.3.3 Transducer Bias Noise

The above noise sources are linear. For FM gyroscopes, noise on proff mass bias is an additional noise source which is especially critical for nonlinear transducers. Electro-static spring softening is a well-known effect in capacitive MEMS transducers [47]. The bias voltage across parallel plates modulates the frequency. Consequently, noise on this bias voltage also causes frequency noise. This problem can be avoided using low-pass filters for the proof mass bias ensuring the noise density at Δf is low enough so that it does not hurt overall noise. However, the bias noise of the pick-off electrodes cannot be filtered. This noise mainly comes from the DC feedback (biasing) network for fully-differential amplifiers. Common-mode noise of the DC biasing causes significant low-frequency noise across the pick-off electrodes. Linear sensing such as comb-drives for the pick-off electrodes decreases the electro-static softening effect and decreases the noise due to that. For tuning purpose, non-linear electrodes can still be used with low-pass filters.

5.4 Test Results with Asymmetric FM and Bandwidth Extension Techniques

For testing, the circuit was connected to the symmetric quad-mass gyroscope (QMG) shown in Figure 5.17 with nominal f_o=24kHz and Q=100k. The frequency-to-digital conversion (FDC) is performed off-chip by digitizing two oscillator outputs and extracting the frequency with a software PLL. The output from the AM channel is obtained from the amplitude detector and also digitized off-chip.

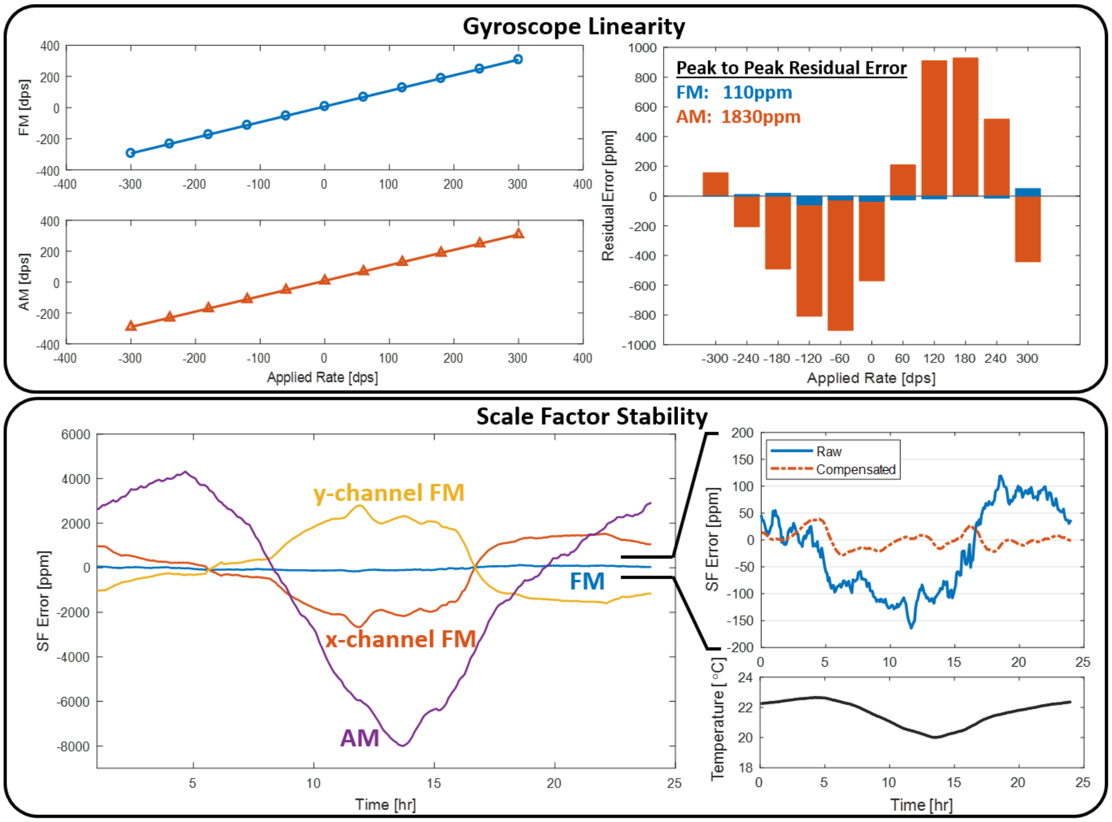

Figure 5.14. Scale factor tests of FM and AM channels.

Figure 5.14 shows the measured linearity and scale factor stability. The sensitivity of conventional AM gyroscopes is determined by transducer bias, electrode gaps, oscillation amplitude, and VGA gain which are difficult to control accurately. In contrast, FM sensitivity is set by an external reference clock and proportional to the slip-factor α_z set by transducer geometry and the sum of the reciprocal velocity ratios $\left(\frac{v_x}{v_y}+\frac{v_y}{v_x}\right)$. For best stability, the velocities are chosen to be equal, contributing only a 1ppm error to the scale-factor for as much as 1400ppm velocity mismatch. For this prototype, the AM and FM linearity over ±300dps are 1830ppm and 110ppm, respectively. Measured over a 24-hour period in an uncontrolled environment, the individual FM channels exhibit considerable fluctuations dominated by temperature variations. Summing the two outputs reduces this variation to ±150ppm, a more than order-of-magnitude improvement over the AM performance. Also shown is a first-order compensated result which reduces the magnitude of the error to less than 40ppm. The temperature of the sensor is obtained without extra circuitry from the FDC based on the transducer's TCF of -30ppm/°C.

Figure 5.15 shows the measured Allan variance for sensors operated at equal oscillation amplitudes and hence nearly identical velocities in both channels and with a deliberate amplitude mismatch. The mismatch increases the scale factor of the sensor, thereby reducing the noise contribution of the FDC. Note that the only change between the two measurements is a different setting in the amplitude controller. The possibility to dynamically adjust long versus short-term stability without increased power dissipation is a unique feature of the FM gyroscope.

These results were achieved with a transducer with parallel plate transduction, which due to its inherent nonlinearity results in noise folding, impairing the ARW. The 1mdps/rt-Hz obtained with a transducer with comb-drive actuation confirms this hypothesis. In addition, the larger oscillation amplitude in the comb-drive actuation decreases the Brownian noise to less than 0.1mdps/rt-Hz. Unfortunately, this design has not been optimized and in the current version exhibits poor long-term stability.

The noise is a function of Δf and decreases from 10mdps/rt-Hz at 100Hz to 1mdps/rt-Hz at 10Hz in the asymmetric mode, where total noise is dominated by the electronics. Below 5Hz close-to-carrier phase noise dominates. Consequently, the mode-split of the gyroscope is tuned to 10Hz with a servo loop with 20ms settling time. The tuning accuracy is not critical since the FDC extracts the instantaneous phase between the x- and y-axis motion for demodulation.

While reducing the mode-split is advantageous for noise, this also lowers the useful bandwidth since the input is chopped at this rate. Since the outputs from the FM and AM channels are in quadrature, the bandwidth of the sum of these outputs is limited only by the bandwidth of the amplitude controller, 1.9kHz in this design. Figure 5.16 illustrates the summing process and the spectrum for a 25Hz rate input. To show the effectiveness of the technique, these measurements have been performed with Δf tuned to 5Hz. The tone at 20Hz is due to transducer nonlinearity and can be reduced with an improved mechanical design. The image is the result of imperfect gain matching of the AM and FM channels. As expected, it disappears after trimming

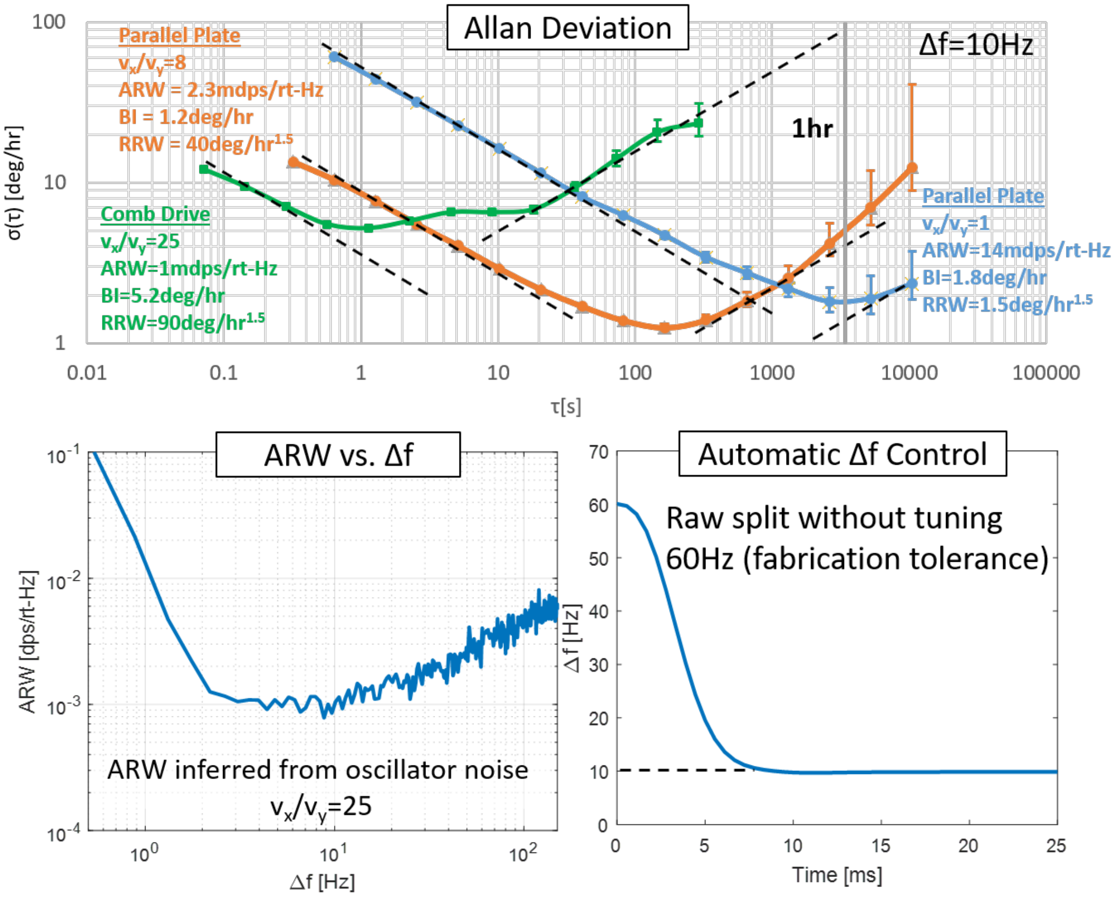

Figure 5.15. Allan deviation of the FM channel, ARW versus mode split, and automatic mode split tuning.

the AM scale factor.

5.5 Conclusion

Table 5.1 compares this result to solutions reported earlier. The FM gyro achieves competitive or better performance in all categories. Note that these results have been achieved without calibration. Not usually reported but a significant error source for applications such as navigation is scale factor accuracy. By relying on an explicit reference supplied in the prototype by an external (precision) clock the FM gyro scale factor stability is more than two orders-of-magnitude better than typical AM gyro accuracy. Further significant advantages include the continuously tuned mode-split and the asymmetric mode of operation used to trade off long- and short-term stability without circuit changes.

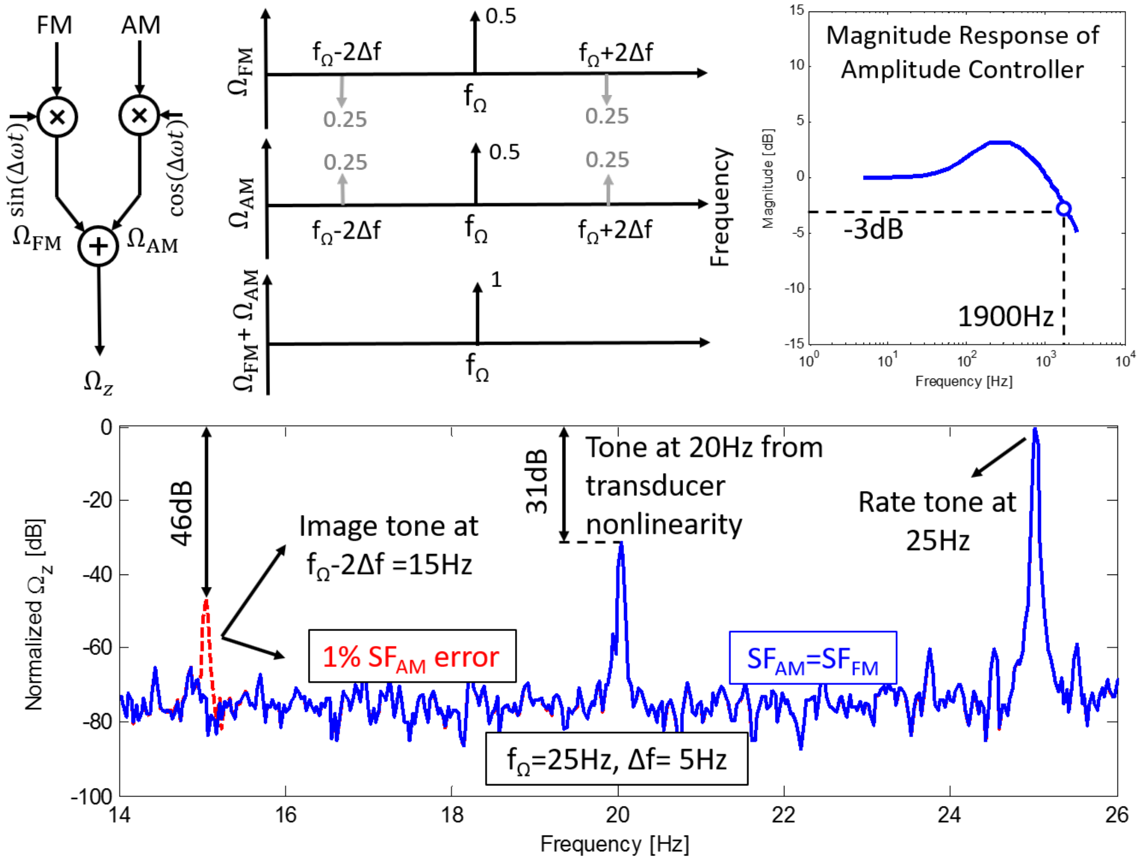

Figure 5.16. Image rejection in combined FM and AM readout.

Table 5.1. Performance summary and comparison table.

	This Work	**ISSCC'17 [1] Marx**	**ISSCC'15 [2] Ezekwe**	**ISSCC'08 [4] Ezekwe**
ARW [dps/rt-Hz]	**0.001[1]**	0.0014	0.0049[7]	0.0028[7]
Bias Stability [deg/hr]	**1.2[1]**	0.9	n.a	n.a.
RRW [deg/hr$^{1.5}$]	**1.5[2]**	3.8	n.a.	n.a.
FS [dps]	**1000[2,3]**	800	2000	n.a.
Bandwidth [Hz]	**1900[4]**	50	520	50
Number of Axes	**1**	1	3	1
Supply [V]	**1.8**	3.3	1.71-3.6	3.3
Power [mW]	**0.45[5]**	1.71	0.37/axis	1[8]
FoM[6] for ARW [dps^2/Hz x W]	**0.45n[1]**	3.4n	8.9n	7.8n
Read-out Features	**-Simultaneous FM and AM**	-ΔΣ with tuned cont. time BPF	-Open loop - With HV	-Closed loop
Bias Stability Methods	**-FM readout -Symmetric transducer and readout**	Manual quadrature tuning	Background phase error correction over temperature	n.a.
Mode Split Sensing	**Direct readout of resonance frequencies**	n.a. (initial tuning)	n.a.	Tone injection

[1] Asymmetric FM

[2] Symmetric FM

[3] Circuit full-scale. Tested up to ±300dps (rate table limitation).

[4] Tested up to 25Hz.

[5] Power does not include off-chip ADCs and DSP.

[6] FOM = Power x ARW^2 (per axis)

[7] Rate noise density reported. ARW = Rate Noise Density/$\sqrt{2}$

[8] Drive electronics power not included.

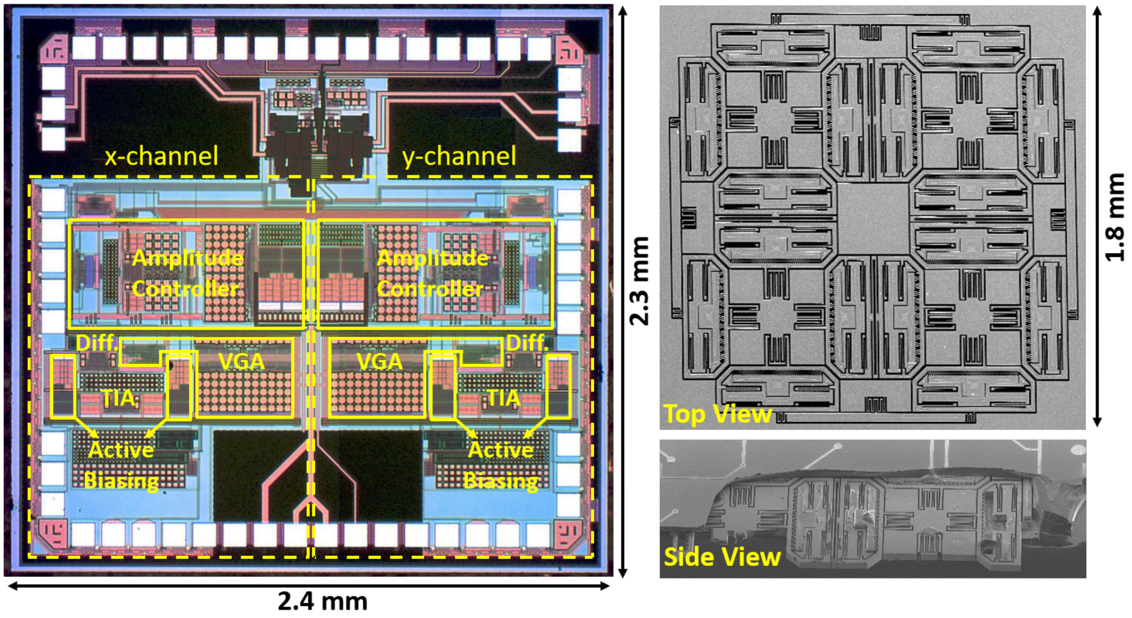

Figure 5.17. Chip micrograph and SEM image of the MEMS gyroscope.

Chapter 6

Conclusion

Size, cost, and power have been limitations for high performance MEMS gyroscopes. This thesis introduces new techniques to break these limitations for conventional AM (force-feedback) and FM gyroscopes.

Conventional AM gyroscopes have a fundamental drawback due to their lack of a a true frequency reference for rate sensing. This thesis introduced a new technique to extract this reference by injecting a calibration signal into the drive mode. The sensitivity of the oscillation frequency to this calibration signal is almost same as the sensitivity (scale-factor) of the force-feedback gyroscope. It has been demonstrated that the the background calibrated scale factor has a temperature coefficient of only 5ppm/°C without any additional calibration and trimming. The quadrature leakage due to the phase error is also suppressed by measuring the sensitivity of the sustaining force to the same calibration signal applied for the scale factor calibration. Moreover, the in-phase errors are also corrected using the sustaining force signal in the drive mode.

Mode-matched FM gyroscopes have been implemented with very high performance. The oscillation frequency term is eliminated by alternating the circular orbit direction between clockwise and anti-clockwise. This chopping behavior is achieved by indexing the phase difference between $+90°$ and $-90°$ using the feedback forces. FM operation with a symmetric transducer and implementation provides a very stable scale factor and bias. The turn-on repeatability of the scale factor is 4ppm and bias is 3mdps over a 1-month test. The TC of SF and bias are 1.25ppm/°C and 3dph/°C, respectively.

New FM techniques are introduced to lower the angle random walk and extend the bandwidth beyond the split between the two oscillator frequencies. In the asymmetric mode an intentionally introduced velocity mismatch suppresses the back-end noise as well as non-linear noise sources in the oscillator. Inherent observation of the oscillation frequencies of both channels in FM operation also enables to operate the gyroscope with a lower frequency split. By using this technique an ARW of 1mdps/rt-

Hz is achieved by consuming less than 0.5mW. Instantaneous AM and FM readouts enable quadrature demodulation and suppress the image problem due to chopping.

FM gyroscopes have a phenomenal scale factor accuracy combined with low bias instability in symmetric operation. They provide high performance without requiring any additional complicated calibration and trimming. Symmetric transducer design minimizes the errors due to mismatch between cross-axis error terms. Linear transducers can potentially enable low close-to-carrier noise and thus lower mode-split to relieve the noise-power trade-off even further. The limitation due to injection locking can be solved using active tuning as has been demonstrated for indexed FM gyroscopes. The tuning strategy needs to be symmetric in order to gain the benefits of FM gyroscopes. The low noise and stable nature of FM gyroscopes promises navigation grade performance with consumer grade cost, size, and power.

Bibliography

[1] Datasheet for ICM-20600: High Performance 6-Axis MEMS MotionTracking Device [Online]. Available: http://www.invensense.com/wp-content/uploads/2015/12/DS-000184-ICM-20600-v1.0.pdf.

[2] Datasheet for HG1900: Inertial Measurement Unit [Online]. Available: https://aerospace.honeywell.com/en//̃media/aerospace/files/brochures/n61-1468-000-001-hg1900-inertialmeasurementunit-bro.pdf.

[3] M. H. Kline, Y. C. Yeh, B. Eminoglu, I. I. Izyumin, M. Daneman, D. A. Horsley, and B. E. Boser, "MEMS gyroscope bias drift cancellation using continuous-time mode reversal," in *2013 Transducers Eurosensors XXVII: The 17th International Conference on Solid-State Sensors, Actuators and Microsystems (TRANSDUCERS EUROSENSORS XXVII)*, June 2013, pp. 1855–1858.

[4] S. Clarke, (2013, December 11). Inertial technology for north finding [Online]. Available: https://www.siliconsensing.com/media/1430/sssl-inertial-technology-for-north-finding-11-dec-2013.pdf.

[5] E. Tatar, S. E. Alper, and T. Akin, "Quadrature-error compensation and corresponding effects on the performance of fully decoupled MEMS gyroscopes," *Journal of Microelectromechanical Systems*, vol. 21, no. 3, pp. 656–667, 2012.

[6] C. D. Ezekwe, W. Geiger, and T. Ohms, "A 3-axis open-loop gyroscope with demodulation phase error correction," in *2015 IEEE International Solid-State Circuits Conference-(ISSCC)*, 2015, pp. 1–3.

[7] D. Lynch, "Vibratory gyro analysis by the method of averaging," in *Proc. 2nd St. Petersburg Conf. on Gyroscopic Technology and Navigation, St. Petersburg*, 1995, pp. 26–34.

[8] S. F. Wyse and R. E. Stewart, "Vibratory gyro bias error cancellation using mode reversal," Oct. 22 2013, US Patent 8,561,466.

[9] I. P. Prikhodko, C. Merritt, J. A. Gregory, J. A. Geen, J. Chang, J. Bergeron, W. Clark, and M. W. Judy, "Continuous self-calibration canceling drive-induced

errors in MEMS vibratory gyroscopes," in *2015 Transducers-2015 18th International Conference on Solid-State Sensors, Actuators and Microsystems (TRANSDUCERS)*, 2015, pp. 35–38.

[10] A. Walther, C. Le Blanc, N. Delorme, Y. Deimerly, R. Anciant, and J. Willemin, "Bias contributions in a MEMS tuning fork gyroscope," *Journal of Microelectromechanical Systems*, vol. 22, no. 2, pp. 303–308, 2013.

[11] I. P. Prikhodko, J. A. Gregory, C. Merritt, J. A. Geen, J. Chang, J. Bergeron, W. Clark, and M. W. Judy, "In-run bias self-calibration for low-cost MEMS vibratory gyroscopes," in *2014 IEEE/ION Position, Location and Navigation Symposium-PLANS 2014*, 2014, pp. 515–518.

[12] J. Y. Cho, J.-K. Woo, J. Yan, R. L. Peterson, and K. Najafi, "Fused-silica micro birdbath resonator gyroscope (μ-BRG)," *Journal of Microelectromechanical Systems*, vol. 23, no. 1, pp. 66–77, 2014.

[13] D. Senkal, M. J. Ahamed, M. H. A. Ardakani, S. Askari, and A. M. Shkel, "Demonstration of 1 million Q-factor on microglassblown wineglass resonators with out-of-plane electrostatic transduction," *Journal of Microelectromechanical Systems*, vol. 24, no. 1, pp. 29–37, 2015.

[14] D. M. Rozelle, "The hemispherical resonator gyro: From wineglass to the planets," in *Spacefl. Mech. 2009.* Citeseer, 2009.

[15] C. D. Ezekwe and B. E. Boser, "A mode-matching closed-loop vibratory-gyroscope readout interface with a $0.004°/\mathrm{s}/\sqrt{Hz}$ noise floor over a 50Hz band," in *2008 IEEE International Solid-State Circuits Conference - Digest of Technical Papers*, Feb 2008, pp. 580–637.

[16] I. P. Prikhodko, S. Nadig, J. A. Gregory, W. A. Clark, and M. W. Judy, "Half-a-month stable 0.2 degree-per-hour mode-matched MEMS gyroscope," in *2017 IEEE International Symposium on Inertial Sensors and Systems (INERTIAL)*, 2017, pp. 1–4.

[17] M. Marx, D. D. Dorigo, S. Nessler, S. Rombach, M. Maurer, and Y. Manoli, "A 27μW 0.06 mm^2 background resonance frequency tuning circuit based on noise observation for a 1.71 mW CT-$\Delta\Sigma$ MEMS gyroscope readout system with 0.9°/h bias instability," in *2017 IEEE International Solid-State Circuits Conference (ISSCC)*, Feb 2017, pp. 164–165.

[18] F. Yesil, S. Alper, and T. Akin, "An automatic mode matching system for a high Q-factor MEMS gyroscope using a decoupled perturbation signal," in *2015 18th International Conference on Solid-State Sensors, Actuators and Microsystems (TRANSDUCERS), 2015 Transducers*, 2015, pp. 1148–1151.

[19] L. Prandi, C. Caminada, L. Coronato, G. Cazzaniga, F. Biganzoli, R. Antonello, and R. Oboe, "A low-power 3-axis digital-output MEMS gyroscope with single drive and multiplexed angular rate readout," in *2011 IEEE International Solid-State Circuits Conference Digest of Technical Papers (ISSCC)*, 2011, pp. 104–106.

[20] A. D. Challoner, H. G. Howard, and J. Y. Liu, "Boeing disc resonator gyroscope," in *2014 IEEE/ION Position, Location and Navigation Symposium-PLANS 2014*, 2014, pp. 504–514.

[21] K. Azgin, "High performance MEMS gyroscopes," *M. Sc. Thesis*, 2007.

[22] I. P. Prikhodko, S. A. Zotov, A. A. Trusov, and A. M. Shkel, "Sub-degree-per-hour silicon MEMS rate sensor with 1 million Q-factor," in *2011 16th International Solid-State Sensors, Actuators and Microsystems Conference (TRANSDUCERS)*, 2011, pp. 2809–2812.

[23] M. H. Kline, Y.-C. Yeh, B. Eminoglu, H. Najar, M. Daneman, D. A. Horsley, and B. E. Boser, "Quadrature FM gyroscope," in *2013 IEEE 26th International Conference on Micro Electro Mechanical Systems (MEMS)*, 2013, pp. 604–608.

[24] I. I. Izyumin, M. H. Kline, Y. C. Yeh, B. Eminoglu, C. H. Ahn, V. A. Hong, Y. Yang, E. J. Ng, T. W. Kenny, and B. E. Boser, "A 7ppm, 6°/hr frequency-output MEMS gyroscope," in *2015 28th IEEE International Conference on Micro Electro Mechanical Systems (MEMS)*, Jan 2015, pp. 33–36.

[25] J.-K. Woo, J. Y. Cho, C. Boyd, and K. Najafi, "Whole-angle-mode micromachined fused-silica birdbath resonator gyroscope (WA-BRG)," in *2014 IEEE 27th International Conference on Micro Electro Mechanical Systems (MEMS)*, 2014, pp. 20–23.

[26] A. Trusov, G. Atikyan, D. Rozelle, A. Meyer, S. Zotov, B. Simon, and A. Shkel, "Force rebalance, whole angle, and self-calibration mechanization of silicon MEMS quad mass gyro," in *2014 International Symposium on Inertial Sensors and Systems (ISISS)*, 2014, pp. 1–2.

[27] R. E. Stewart, "Self-calibration of scale factor for dual resonator class II Coriolis vibratory gyros," Mar. 20 2012, US Patent 8,136,382.

[28] A. Trusov, I. Prikhodko, D. Rozelle, A. Meyer, and A. Shkel, "1 ppm precision self-calibration of scale factor in MEMS coriolis vibratory gyroscopes," in *2013 Transducers & Eurosensors XXVII: The 17th International Conference on Solid-State Sensors, Actuators and Microsystems (TRANSDUCERS & EUROSENSORS XXVII)*, 2013, pp. 2531–2534.

[29] D. M. Rozelle, "Closed loop scale factor estimation," Dec. 8 2009, US Patent 7,628,069.

[30] M. Kline, "Frequency modulated gyroscopes," Ph.D. dissertation, University of California, Berkeley, 2013.

[31] S. Henzler, "Theory of TDC operation," *Time-to-digital Converters*, pp. 19–42, 2010.

[32] Datasheet for SiT5357: Precision super-TCXO [Online]. Available: https://www.sitime.com/sites/default/files/gated/SiT5357-datasheet.pdf.

[33] J. Seeger, M. Lim, and S. Nasiri, "Development of high-performance, high-volume consumer MEMS gyroscopes," in *Solid-State Sensors, Actuators, and Microsystems Workshop*, 2010, pp. 61–64.

[34] Datasheet for CRS07: Angular rate sensor [Online]. Available: http://www.siliconsensing.com/media/30685/DocNo-CRS07-00-0100-132-Rev-1PDF.pdf.

[35] S. F. Wyse and D. D. Lynch, "Vibrating mass gyroscope and method for minimizing bias errors therein," Mar. 13 2007, US Patent 7,188,523.

[36] I. Izyumin, M. Kline, Y. C. Yeh, B. Eminoglu, and B. Boser, "A 50 μW, 2.1 mdeg/s/$\sqrt{Hz}$ frequency-to-digital converter for frequency-output MEMS gyroscopes," in *ESSCIRC 2014 - 40th European Solid State Circuits Conference (ESSCIRC)*, Sept 2014, pp. 399–402.

[37] Datasheet for M100: High precision TCXO [Online]. Available: http://www.conwin.com/datasheets/tx/tx382.pdf.

[38] M. Yin and M. Ghovanloo, "A low-noise preamplifier with adjustable gain and bandwidth for biopotential recording applications," in *2007 IEEE International Symposium on Circuits and Systems*, May 2007, pp. 321–324.

[39] H. Chandrakumar and D. Markovi, "A 2μW 40mV_{pp} linear-input-range chopper-stabilized bio-signal amplifier with boosted input impedance of 300MΩ and electrode-offset filtering," in *2016 IEEE International Solid-State Circuits Conference (ISSCC)*, Jan 2016, pp. 96–97.

[40] F. Bahmani and E. Sánchez-Sinencio, "A stable loss control feedback loop for VCO amplitude tuning," *IEEE Transactions on Circuits and Systems I: Regular Papers*, vol. 53, no. 12, pp. 2498–2506, 2006.

[41] R. Behzad, *RF microelectronics (2^{nd} Edition).* Prentice Hall New Jersey, 2011.

[42] B. Eminoglu, S. E. Alper, and T. Akin, "An optimized analog drive-mode controller for vibratory MEMS gyroscopes," *Procedia Engineering*, vol. 25, pp. 1309–1312, 2011.

[43] S. Rombach, M. Marx, S. Nessler, D. De Dorigo, M. Maurer, and Y. Manoli, "An interface ASIC for MEMS vibratory gyroscopes with a power of 1.6 mW, 92 dB DR and $0.007°/s/\sqrt{Hz}$ noise floor over a 40 Hz band," *IEEE Journal of Solid-State Circuits*, vol. 51, no. 8, pp. 1915–1927, 2016.

[44] B. Razavi, *Design of Analog CMOS Integrated Circuits.* McGraw-Hill, Inc., 2000.

[45] E. Vittoz, *Implementations of the Pierce Oscillator.* Springer, 2010.

[46] Datasheet for AD7982: 18-Bit, 1 MSPS PulSAR 7 mW ADC in MSOP/LFCSP [Online]. Available: http://www.analog.com/media/en/technical-documentation/data-sheets/AD7982.pdf.

[47] S. D. Senturia, *Microsystem design.* Springer Science & Business Media, 2007.